UNIVERSITY OF CALIFORNIA SAN DIEGO

Variability of boundary currents in low latitude regions: the northern Indian Ocean and southern Pacific Ocean

A dissertation submitted in partial satisfaction of the
requirements for the degree
Doctor of Philosophy

in

Oceanography

by

Arachaporn Anutaliya

Committee in charge:

Uwe Send, Chair
Julie L. McClean, Co-chair
Janet Sprintall, Co-chair
Graham Elliott
Sarah Giddings
Shang-Ping Xie

2019

The dissertation of Arachaporn Anutaliya is approved, and it is acceptable in quality and form for publication on microfilm and electronically:

_____

_____

_____

_____
Co-Chair

_____
Co-Chair

_____
Chair

University of California San Diego

2019

TABLE OF CONTENTS

LIST OF FIGURES

LIST OF TABLES

ACKNOWLEDGEMENTS

Firstly, I would like to thank my advisors, Dr. Uwe Send, Dr. Janet Sprintall, and Dr. Julie McClean for many meeting hours, many manuscript drafts, and all the effort in shaping me to become a better oceanographer. I learned a lot in the past years, and it is not possible without your suggestions and guidance. I really appreciate your time and patience. Also, thank you all for the understanding and support you provide no matter what life event or health problem I was going through. I am very grateful to have all of you as my advisors. Thank to Sarah Giddings, Shang-Ping Xie, and Graham Elliott for kindly joining my committee and giving me advices along the way. Thanks to SIO professors for educating me. I started the program knowing very little about oceanography and with your help all the basics are covered in less than two years. I would like to thank everyone in Uwe's lab, especially Dr. Matthias Lankhorst who always help me no matter how simple my questions are.

Thank to my SIO friends: Celia Ou, Shantong Sun, Tingting Sun, Weijie Wang, Angelica Rodriguez, and Jannes Koelling. Thanks to my friends in math department: Stephan Weispenning, Angelika Kurtz, Simon Weispenning, Michelle Bodnar, Ching Wei Ho, Peter Spaarse, Emma Sawin, and Nathaniel Gallup for many hours of hanging out, even though we only get together around playgrounds lately. Shout out to Stephan, Angelika, Simon, and Michelle who help take care of Charlotte (and myself). You made my years spent here as a graduate student a lot more fun! Also, thanks to all the foods that keep us together.

I would like to thank my mom, dad, sister, and brother for all your supports, encouragements, and for pampering me whenever I find some time to visit home. Special thanks to my dad who inspires me to pursue Ph.D. and always believe in me. Although I am not fortunate enough to have you around when I am at the finish line, I hope you are still proud of me. I miss you. Also, thank to my in-law family for the help and support you provided.

Thank Charlotte for joining the family in the last 3 years. You bring so much joy to my parents, Kuang, and myself. You make my most difficult days easier (and sometimes you

make my easy days more difficult). On days that everything gives up on me, you did not and that motivates me to become better. Kuang, I cannot thank you enough for all your supports, for being by my side, and for always wanting me to be happy. In the past ten years, my life thousands of miles away from my family is much easier and much more enjoyable with you. I really cannot imagine going through graduate school without your help and support. Thank you two so much, and I love you both.

Chapter 2 is a draft of manuscript in preparation for submission as "PIES observations of flows off the Sri Lankan eastern and southern coast", by A. Anutaliya, U. Send, J. L. McClean, and J. Sprintall. The dissertation author was the primary investigator and author of this work.

Chapter 3, in full, is a reprint of the material as it appears in Ocean Science, "An undercurrent off the east coast of Sri Lanka", by A. Anutaliya, U. Send, J. L. McClean, J. Sprintall, L. Rainville, C. M. Lee, S. U. P. Priyantha, A. J. Wallcraft, and E. J. Metzger (2017). The dissertation author was the primary investigator and author of this paper.

Chapter 4, in full, is a reprint of the material as it appears in Journal of Geophysical Research, "Mooring and seafloor pressure end-point measurements at the southern entrance of the Solomon Sea: subseasonal to interannual flow variability", by A. Anutaliya, U. Send, J. Sprintall, J. L. McClean, M. Lankhorst, and J. Koelling (2019). The dissertation author was the primary investigator and author of this paper.

Chapter 5 is a draft of manuscript in preparation for submission as "Observations of the Solomon Sea inflow and outflow", by A. Anutaliya, U. Send, J. Sprintall, and J. L. McClean. The dissertation author was the primary investigator and author of this work.

VITA

2013	B. S. in Environmental Sciences, University of Virginia
2015	M. S. in Oceanography, University of California San Diego
2019	Ph. D. in Oceanography, University of California San Diego

PUBLICATIONS

A. Anutaliya, U. Send, J. Sprintall, J. L. McClean,M. Lankhorst, and J. Koelling, 2019: "Mooring and seafloor pressure end point measurements at the southern entrance of the Solomon Sea: subseasonal to interannual flow variability". *J. Geophys. Res. Oceans*, **124**, 5085-5104

A. Anutaliya, U. Send, J. L. McClean, J. Sprintall, L. Rainville, C. M. Lee, S.U.P. Jinadasa, A. J. Wallcraft, and E. J. Metzger, 2017: "An undercurrent off the east coast of Sri Lanka". *Ocean Sci.*, **13**, 1035-1044

ABSTRACT OF THE DISSERTATION

Variability of boundary currents in low latitude regions: the northern Indian Ocean and southern Pacific Ocean

by

Arachaporn Anutaliya

Doctor of Philosophy in Oceanography

University of California San Diego, 2019

Uwe Send, Chair

Julie L. McClean, Co-chair

Janet Sprintall, Co-chair

This thesis examines the low-latitude western boundary current in the northern Indian Ocean, to understand its role in inter-basin salinity exchange, and that in the southern Pacific Ocean to understand its forcing mechanisms. Continuous volume transports along Sri Lankan eastern and southern coasts are inferred from in-situ bottom pressure and acoustic travel-time measurements. Together with remotely-sensed surface salinity, eddy salt flux is estimated; the

flux produced by the boundary currents along Sri Lankan eastern (southern) coasts accounts for 11% (6%) of the salt input required to maintain salinity in the Bay of Bengal. In addition, glider measurements, historical hydrographic data, and Ocean General Circulation Models (OGCMs) are analyzed to better understand the variability of flow below 200 m depth and the associated eddy salt flux. Both observations and the OGCMs reveal the presence of an opposing undercurrent along the Sri Lankan eastern coast during the spring monsoon transition and southwest monsoon. However, the subsurface salinity range near the coast is small, resulting in low eddy salt flux produced by the undercurrent.

In the southern Pacific Ocean, flow derived from end-point dynamic heights and bottom pressures at the Solomon Sea southern entrance fluctuates greatly on subseasonal, seasonal, and interannual timescales. The subseasonal variability of flow in the 0-500 m depth layer (up to 25 Sv in one week) is partly forced by local and remote winds. The seasonal and interannual fluctuations ($\pm$10 Sv) are mainly influenced by westward-propagating Rossby waves from the interior of the Pacific Ocean. Anomalously high (low) equatorward volume transport during El Niño (La Niña) conditions is accompanied by a suppressed (enhanced) seasonal cycle. At the Solomon Sea exits, continuous mooring measurements of the flow are also available; thus, the relationship between the Solomon Sea inflow and outflow is investigated over the overlapping period of July 2012 - February 2014. Variability of the inflow and outflow compares well, with mean volume transport above the 26.7 isopycnal at the exit of 17.3$\pm$2.1 Sv and that at the entrance of 13.8$\pm$3.3 Sv. The difference is likely contributed from flow through the unmeasured Jomard Channel at the southwest of the basin.

Chapter 1

Introduction

Wind stress curl in the interior of Pacific Ocean produces meridional flow know as Sverdrup transport; generally, the interior Sverdrup transport is equatorward between the equator and 30 ° N where trade winds prevail and poleward between 30 ° N to 60 ° N where the easterly winds prevail. To balance the meridional interior flow, strong boundary current (BC) is needed. As meridional BC flows across latitude, the planetary vorticity is modified resulting in change in the relative vorticity that has to be removed. The coastal friction along the western boundary of the ocean provides the right sign of vorticity to remove the relative vorticity. This mechanism produces strong flow in boundary currents along the western boundary of the ocean, known as western boundary currents (WBCs). In addition to WBCs, there are also other BCs that arise from different mechanisms. For example, the summer monsoon current and the winter monsoon current, boundary currents along the southern coast of Sri Lanka, which arise from westward-propagating Rossby waves excited by reflection of equatorial Kelvin waves at the eastern boundary of the Indian Ocean. The BCs play an important role in connecting circulations between latitudes or water basins. In some regions such as BCs along the eastern and southern coasts of Sri Lanka, BCs supply water with contrasting physical properties, such as salinity and temperature, to their destinations and maintain the equilibrium of these properties. These BCs can be influenced by

local and remote forcings, such as winds and planetary waves transferring atmospheric signals across latitudes or water basins.

This dissertation is focused on the Low-Latitude Western Boundary Currents (LLWBCs) of the southern Bay of Bengal (BoB) in the northern Indian Ocean and the Solomon Sea in the western low-latitude south Pacific; both regions are highly influenced by seasonally reversing winds. The presence of a landmass to the north of the Indian Ocean causes seasonal asymmetric heating over the landmass and the ocean producing the seasonal wind reversal (e.g. Webster et al., 1998). During the southwest monsoon (June - August), winds blow northeastward bringing moisture from the ocean to the continent. During the northeast monsoon (November - January), winds blow southwestward transferring dry air from land to the ocean. The monsoon system not only affects circulation in the Indian Ocean, but also in the equatorial Pacific (e.g. Mooley and Parthasarathy, 1984; Yasunari, 1990; Butt and Lindstrom, 2000) including the Solomon Sea (Kuroda, 2000; Cravatte et al., 2011). Furthermore, westward propagating Rossby waves driven by seasonal remote winds are important in both oceans, particularly at seasonal timescales (Vinayachandran et al., 2005a; Sreenivas et al., 2012; Wang et al., 2000; Chen & Qiu 2004; Melet et al., 2010b).

On interannual timescales, the circulations in the BoB and the Solomon Sea are affected by an interannual large-scale climate mode, the El Niño Southern Oscillation (ENSO). El Niño events are associated with the weakening of the easterly equatorial trade winds and the relaxation of the isopycnal gradient across the equatorial Pacific (e.g. Ramage and Hori, 1981). The ENSO modifies the equatorial winds in the Indian ocean altering the seasonal Kelvin waves and thus circulation in the BoB (Sreenivas et al., 2012). The BoB is also affected by the Indian Ocean Dipole (IOD) which is a climate mode associated with strong wind anomalies along the equatorial Indian Ocean (Saji et al. 1999). A positive IOD (pIOD) event produces a southeasterly wind anomaly, resulting in the accumulation of warm and moist air over the eastern part of Africa but dry and cold air over the Indonesian archipelago. A negative wind stress curl anomaly is also

associated with pIOD events, which can result in a reduction or suppression of cyclonic eddies in the BoB (Sreenivas et al., 2012). Although the ENSO and IOD are different climate modes, a model study showed that they interact with and enhance each other through the atmosphere when they are concurrent (Luo et al., 2010).

Chapters 2 and 3 of this dissertation examine the BCs along Sri Lankan eastern and southern coasts using in-situ observations, remotely sensed measurements, and numerical simulations to understand variability of the BCs and their role in salinity exchange between the Arabian Sea and the BoB. Chapters 4 and 5 focus on the New Guinea Coastal Current and New Guinea Coastal Undercurrent system which is the LLWBC in the Solomon Sea. Volume transport into the Solomon Sea at the southern entrance and its variability at subseasonal, seasonal, and interannual timescales are discussed in Chapter 3, while a comparison between the volume inflow and outflow of the Solomon Sea is presented in Chapter 4.

Chapter 2

PIES observations of flows off the Sri Lankan eastern and southern coasts

Abstract

Two pairs of Pressure sensing Inverted Echo Sounders (PIES) have been deployed to infer the strengths of the boundary currents along the eastern and southern coasts of Sri Lanka. A technique has been developed to estimate volume transport in the 0-200 m and 200-600 m depth layers based on PIES acoustic travel time, bottom pressure, and satellite altimetry in combination with local historical hydrography. The estimated volume transport, in good agreement with an independent transport from Seaglider measurements, exhibits high variability on seasonal timescales associated with the monsoon wind reversal and on interannual timescales associated with Indian Ocean Dipole conditions. While the estimated transport along the eastern coast reverses its direction twice a year, transport along the southern coast shows a once-a-year reversal pattern in agreement with previous literature. With the use of satellite sea surface salinity, continuous time series of eddy salt transport along the Sri Lankan coasts in the 0-200 m depth layer are estimated. Time-mean eddy salt flux over the April 2015 – December 2018 (December

2015 – November 2017) period along the eastern (southern) coast accounts for 11% (6%) of the salt budget required to balance the 0.13 Sv of annual freshwater input into the Bay of Bengal. Currents along the eastern and southern coasts are often not continuous resulting in a divergence or convergence at the southeastern coast of Sri Lanka with some exceptions during the northeast monsoon and fall monsoon transition of some years. The East Indian Coastal Current often extends to the eastern coast of Sri Lanka and turns westward along the southern coast for a period of 1-2 months during the northeast monsoon exporting low-salinity water out of the Bay of Bengal. During the early fall monsoon transition, the eastward-flowing Summer Monsoon Current turns northward along the Sri Lankan eastern coast injecting high-salinity water from the equatorial Arabian Sea into the Bay of Bengal.

2.1 Introduction

The Bay of Bengal (BoB), a semi-enclosed ocean basin in the northeastern Indian Ocean, gains $\sim$0.13 Sv of freshwater annually from precipitation less evaporation and river runoff as estimated from observations, reanalysis products, and numerical simulations (Rao and Sivakumar, 2003; Sengupta et al., 2006; Wilson and Riser, 2016). One export pathway of freshwater out of the BoB is via the East India Coastal Current (EICC) during the northeast monsoon when it flows southward. During this period, the EICC extends southward from the east coast of India to the east coast of Sri Lanka (Shetye et al., 1996) and then turns westward to flow along the south coast of Sri Lanka (Schott et al., 1994; Hacker et al., 1998; Reppin et al., 1999) transporting low salinity water out of the basin (Han and McCreary, 2001; Wijesekera et al., 2015). During the southwest monsoon, the eastward summer monsoon current (SMC) transports high salinity water originating in the Arabian Sea (AS) into the BoB (Vinayachandran et al., 1999; Han and McCreary, 2001; Vinayachandran et al., 2013; Sanchez-Franks et al., 2019). Numerical simulations also show the intrusion of water of AS origin into the BoB at the end of the southwest monsoon (Jensen,

2001b), a result of northward Ekman transport arising from the monsoon wind reversal (Jensen, 2003). Analyses using multiple numerical simulations and reanalysis products show that the depth-integrated salt transport across 6°N into the BoB reaches its maximum in July at ∼84°E, while the maximum salt transport out of the BoB across the same transect reaches its maximum in January at ∼ 82°E (D'Addezio et al., 2015). Yet continuous long-term observations of the boundary currents associated with salt exchange between the BoB and the rest of the IO remain limited, particularly off the eastern and southern coasts of Sri Lanka.

The EICC, the SMC, and the winter monsoon current (WMC) are mainly driven by monsoon winds and wind-generated equatorial waves, and their seasonal variations have been studied using both observations (Schott et al., 1994; Shetye et al., 1996; Wijesekera et al., 2015) and numerical simulations (McCreary et al., 1993; McCreary et al., 1996; Shankar et al., 1996; Schott and McCreary, 2001). Off the eastern coast of Sri Lanka, the southward-flowing EICC is present during the northeast monsoon (Shetye et al., 1996; Wijesekera et al., 2015), while the Sri Lanka Dome (SLD), a seasonal cyclonic eddy, dominates the regional circulation during the southwest monsoon (Vinayachandran and Yamagata, 1997; Vinayachandran et al., 1999; Shankar et al., 2002; de Vos et al., 2014). During the monsoon transitions, the surface geostrophic flow derived from satellite altimetry is northward (Eigenheer and Quadfasel, 2000; Durand et al., 2009; Lee et al., 2016). Flow in the upper 100-200 m along the eastern coast of Sri Lanka reverses its direction twice a year flowing northward during the monsoon transitions and southward during monsoon seasons. In addition, an opposing undercurrent below the surface layer is present in boreal spring and summer (Anutaliya et al., 2017). Yet, to date, there have been few continuous or simultaneous measurements of flows off the Sri Lankan eastern and southern coasts to demonstrate the regional circulation and its contribution to BoB freshwater export.

In this study, we utilized continuous measurements from seafloor Pressure with Inverted Echo Sounders (PIES) deployed nearly simultaneously over approximately a 4-year period off the eastern coast of Sri Lanka and a 2-year period off the southern coast of Sri Lanka and surface

velocity from satellite altimetry to estimate the volume transport of these boundary currents and understand the regional circulation. Together with remotely-sensed sea surface salinity (SSS), we use the PIES measurements to estimate salt fluxes along the Sri Lankan eastern and southern coasts. In addition to the seasonal monsoon, we also examined the impact of interannual climate modes, such as the Indian Ocean Dipole (IOD) and the El Niño-Southern Oscillation (ENSO), on the circulation off the eastern and southern coasts of Sri Lanka. The data sets and methodology are described in section 2 and 3, respectively. Section 4 presents the observed velocity, volume transport, and salt flux across the transects. Sections 5 and 6 contain the discussion and summary, respectively.

2.2 Data sets

2.2.1 In-situ measurements

A pair of PIES (Kennelly et al., 2007) were deployed from November 2014 to March 2019 off the eastern coast (8.0°N, 81.75°E: site EI and 8.0°N, 83.40°E: site EO) and from December 2015 to the present (June 2019) off the southern coast (5.85°N, 80.50°E: site SI and 4.25°N and 80.50°E: site SO) of Sri Lanka. Both inshore PIES were at ∼600 m depth and both offshore PIES were at ∼4000 m depth. The separation of approximately 100 nautical miles was chosen based on boundary current scales derived from altimeter data (Lee et al., 2016; Section 2.2.2) and Seaglider measurements. The PIES measured bottom pressure and acoustic travel time at locations bracketing the expected position of the boundary current along each Sri Lankan coast, although the location and width of the flow along the southern coast varies seasonally (Schott et al., 1994). Acoustic travel time data off the southern coast at the inshore location are missing due to instrument malfunction. PIES bottom pressure was processed to eliminate the exponential linear drift and tidal signals (Kennelly et al., 2007), thus, the derived pressure fluctuation resolves variability shorter than the deployment period (∼4 years). The bottom pressure fluctuation

captures the barotropic flow fluctuation while the acoustic travel time captures baroclinic flow mainly contributed by temperature variations in the water column (in addition to sea surface height changes).

Seagliders were deployed by University of Washington along the same transects to repeatedly sample temperature and salinity from the surface to $\sim$1000 m during February 2014 - January 2016 off the eastern Sri Lanka coast and May 2016 - May 2019 off the southern coast (Lee et al., 2016; Figure 2.1). The gliders take one to two weeks to cross either transect and there are 14 (26) crossings with 7 (16) glider crossings overlapping with the PIES observation period at the eastern (southern) sections. Absolute geostrophic flow in the upper 1000 m was calculated using the measured depth-averaged velocity (Lee et al., 2016). The absolute geostrophic velocity determined from the glider was used to directly compute volume transport instead of using the glider temperature and salinity profiles to compute geostrophic velocity as done by Anutaliya et al. (2017). This is because in this study the glider measurements are primarily used to calibrate and validate the time series of volume transport and salt flux as estimated by the PIES. The vertical structure of the glider velocity profiles was utilized to construct details of the velocity profiles based on PIES measurements and satellite altimetry as described below (Section 2.3.1). The glider volume transports were also used to adjust for the time-mean volume transport that cannot be determined from the PIES measurements; the adjustment was taken as the mean difference between the glider volume transport and the mean PIES volume transport over the period that overlaps with that glider crossing. Salinity measurements from the Seagliders were used together with the velocity profiles to evaluate the errors associated with the salt flux estimations by the PIES, satellite altimetry, and SSS at the transects.

Conductivity-Temperature-Depth (CTD) profiles from historical shipboard hydrography and Argo floats similar to those described by Anutaliya et al. (2017) were used to establish a relationship between integrals of the baroclinic flow relative to a bottom reference and a linear combination of PIES acoustic travel time and satellite altimetry. There are 281 profiles (30

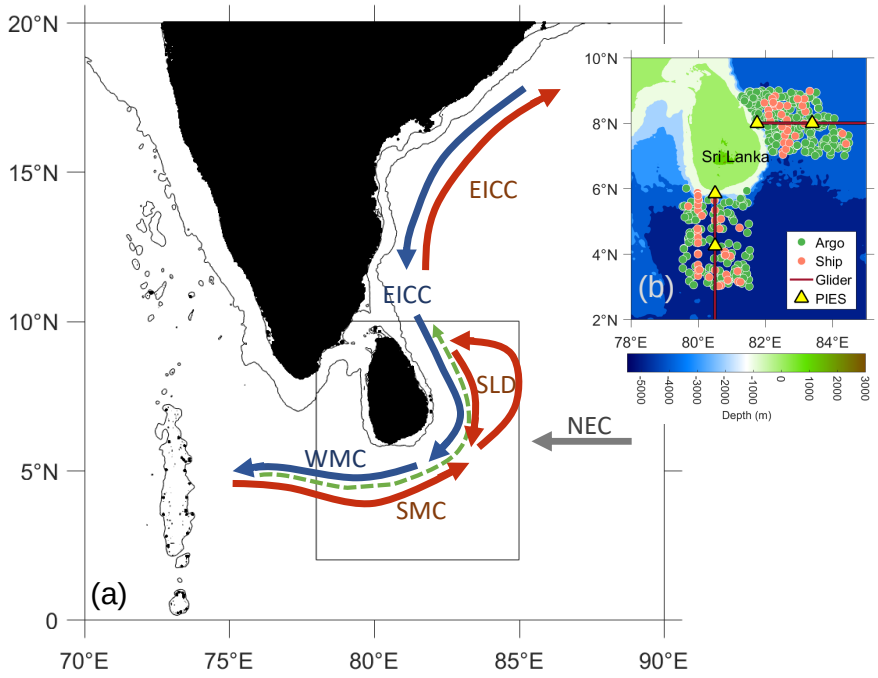

Figure 2.1: Map of the observing area and the dominant currents during the southwest monsoon (red), northeast monsoon (blue), spring monsoon transition (gray), and fall monsoon transition during some years (e.g. 2015 and 2018; green dashed). Black contour lines in (a) are plotted at 0 and 1000 m depths. EICC is the East Indian Coastal Current, WMC is the Winter Monsoon Current, SMC is the Summer Monsoon Current, SLD is the Sri Lanka Dome, and NEC is the North Equatorial Current. The inset shows bathymetry (m) of the Indian Ocean around Sri Lanka with the location of historical shipboard (orange) and Argo (green) hydrographic profiles, PIES instruments (yellow triangles) and nominal glider tracks (maroon lines).

profiles from shipboard hydrography and 251 profiles from Argo floats) sampled within the eastern box (7°N - 9°N) and less than 190 km off the eastern coast, and 185 profiles (39 profiles from shipboard hydrography and 146 profiles from Argo floats) sampled within the southern box (3°N - 7°N) and 79.5°E - 81.5°E (Figure 2.1). The CTD profiles were sampled to depths between 600 and 2000 m. All temperature-salinity profiles were used to simulate acoustic travel time signal for the inshore (shallow, ∼600 m) PIES, but only those that sampled to 2000 m (214 profiles off the eastern coast and 136 profiles off the southern coast) were used to simulate acoustic travel time signal for the offshore (deep, ∼4000 m) PIES with a constant temperature and salinity assumed between 2000 and 4000 m depth.

2.2.2 Remotely sensed data

The gridded satellite Sea Level Anomaly (SLA) is a delayed-time merged product derived from all available altimeter mission and is available over the 1993 - 2018 period on a ¼°grid at daily resolution (Ducet et al., 2000). The satellite SLA reflects expansion of the water column due to both steric height (temperature and salinity variations) and mass changes. The SLA was linearly interpolated onto the 8.0°N eastern and 80.5°E southern transects to combine with the PIES acoustic travel time and estimate baroclinic flow across the transects.

Remotely sensed sea surface salinity (SSS) is derived from Soil Moisture Active Passive (SMAP; Meissner et al., 2018). The product is an 8-day running average with 40 km spatial resolution interpolated onto a ¼°grid and is available from April 2015 - December 2018. The SSS is linearly interpolated onto the 8.0°N eastern and 80.5°E southern transects and used to estimate the salt flux carried by the boundary currents.

2.3 Methodology

2.3.1 Volume transport calculation

Dynamic height calculated from historical hydrography shows that the boundary current is concentrated in the upper 200 m of the water column. Therefore, we analyzed measurements from PIES and satellite SLA along each transect to estimate the across-transect volume transport in the surface layer (0-200 m depth layer) separately from that in the subsurface (200-600 m depth) layer. The surface-layer volume transport fluctuation (Q'_{sfc}) is computed as the horizontal difference between the vertical integral of geopotential anomaly (or the geopotential integral: G_{sfc}) from the surface to 200 m depth referenced to the depth of PIES at the inshore (In, ∼600 m depth) and offshore (Off , ∼4000 m depth) sites. The geopotential integral is combined with the geopotential (Φ) fluctuation at the reference depth level provided by the PIES pressure fluctuation (divided by the mean density at the PIES depths estimated from the nearby hydrography),

$$Q'_{sfc}(t) = \frac{1}{f}\left((G^{Off}_{sfc}(t) + \Phi^{Off}(t)\Delta z) - (G^{In}_{sfc}(t) + \Phi^{In}(t)\Delta z)\right), \tag{2.1}$$

where f is the Coriolis parameter at the mid-transect location (8.0°N for the eastern transect and 5.05°N for the southern transect), and Δz is the depth layer of 200 m. The historical hydrography sampled near to each PIES location was used to parametrize G_{sfc} based on hydrography-simulated acoustic travel time and satellite SLA. In addition to the hydrography, satellite SLA is also used to adjust for the height of the water column at the instances when the hydrographic profiles are sampled. The relationship is determined separately for each PIES site (Figure 2.2). Only satellite SLA is used to estimate G_{sfc} at the SI site as the travel time is missing. The subsurface-layer (200-600 m) volume transport is computed similarly except that the geopotential integral is estimated over the 200-600 m depth layer (G_{sub}) and so Δz is 400 m. Note that the method presented here is similar to the GEM-ETTA technique (Byrne, 2000)

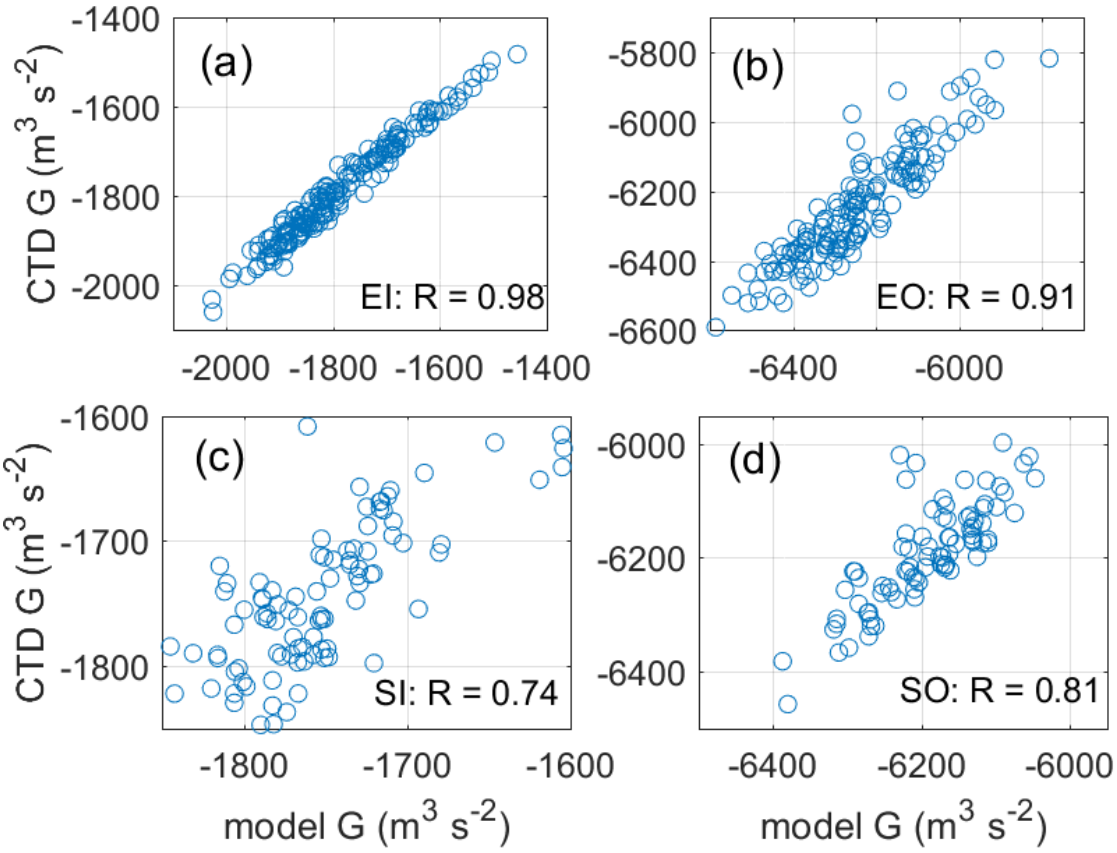

Figure 2.2: Scatter plot between the vertical integral of the geopotential (G_{sfc}) over the 0-200 m layer referenced to the PIES depth calculated from historical CTD profiles (y-axis) and that obtained through a linear regression against simulated acoustic travel time and satellite SLA (x-axis) at the eastern inshore (EI; a), eastern offshore (EO; b), and southern offshore (SO; d) sites. Only satellite SLA used for the model G_{sfc} at the southern inshore (SI) site (c). The corresponding correlation coefficient is shown in the lower right corner of each subplot.

that uses both acoustic travel time and surface steric height to parameterize the temperature and salinity profiles. However, the number of historical hydrographic profiles in this region of the BoB is limited and the water column structure is more variable. Therefore, instead of parametrizing profiles of salinity, we directly relate just the integral of interest (geopotential integral over the target layer) to the measured quantities (PIES acoustic travel time and satellite altimetry). This gives a more robust relationship since G is a double integral of specific volume anomaly.

The time-mean volume transport is calculated from averaging the difference between the

Seaglider absolute geostrophic transport during each crossing and the PIES estimated transport fluctuation overlapping with that glider crossing. Only a few glider crossings are available which overlap with the PIES time series, particularly at the eastern transect, causing high uncertainty in the estimation of the time-mean volume transport. However, the glider volume transports suggest that time-mean volume transports at both transects are likely small and the main focus of this study is on the fluctuating component of the flow. The uncertainties associated with the surface-layer volume transport estimates are 4.3 and 5.7 Sv for the flow along the eastern and southern coasts of Sri Lanka, respectively. At the eastern (southern) section, 2.2 (2.8) Sv of this uncertainty is contributed by the instrument accuracy and 3.7 (4.9) Sv is contributed by the calculation technique; the total uncertainty is calculated as the sum of variances produced by both components. Root-mean-square (rms) difference between the calculated surface-layer volume transport time series and the available Seaglider volume transport is 6.1 Sv for the flow along the Sri Lankan eastern coast and 3.1 Sv for the flow along the southern coast. For the subsurface layer, the uncertainty is 6.1 (7.4) Sv for the flow along the eastern (southern) coast, of which 4.3 (4.8) Sv is from the calculation technique and 4.3 (5.6) Sv is from the instrument accuracy. In addition to the layer volume transports, velocity profiles were estimated using vertical Empirical Orthogonal Function (EOF) modes from the Seaglider measurements. The velocity profile was constructed as a linear combination of the first two leading EOFs constrained by the surface and subsurface volume transports calculated from the PIES measurements and satellite SLA (Figure 2.3; Anutaliya et al., 2019).

2.3.2 Eddy salt flux estimation

The salt flux component calculated here is determined from the product of temporal fluctuations of salinity and temporal fluctuations of velocity at each transect; the time-mean of the product is the eddy salt flux ($\overline{F}_s(t)$) and the time series will be hereafter referred to as eddy salt transport ($F_s(t)$). The eddy salt transport is estimated using the time-mean of density (ρ) sampled

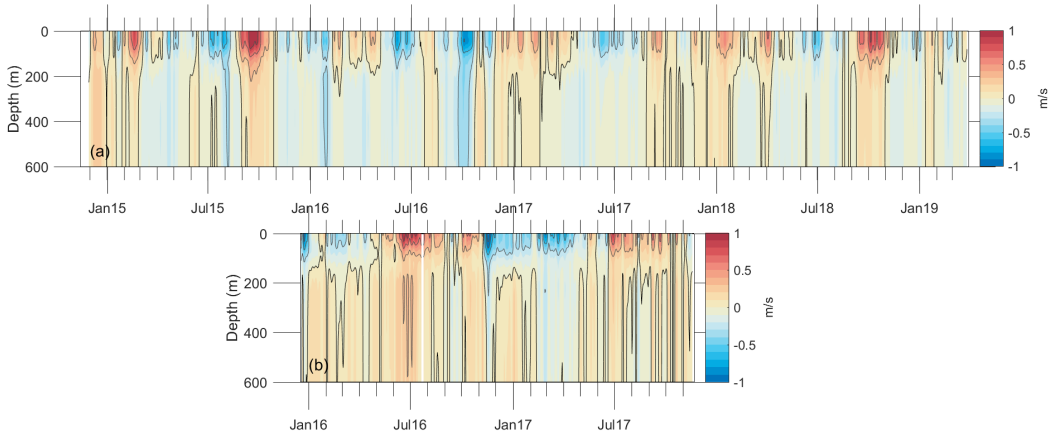

Figure 2.3: Mean geostrophic velocity (m/s) across the transect estimated from the surface and subsurface volume transport at the eastern (a) and southern sections (b). Color contour is plotted every 0.05 m/s, the gray contour is plotted every 0.3 m/s, and the black contour is zero velocity.

by historical hydrography at each location, the local profiles of salinity ($S(s,z,t)$) and velocity ($v(s,z,t)$), and the along-transect distance (s), as follows,

$$F_s(t) = \int_{z=0}^{200} \int_{s^{In}}^{s^{Off}} \rho \times (S(s,z,t) - \overline{S}(z)) \times (v(s,z,t) - \overline{v}(z)) ds dz, \tag{2.2}$$

where s^{In} and s^{Off} represent the location of PIES at the inshore and offshore sites, respectively, $\overline{S}(z)$ is the time-mean salinity profile from the local hydrography and $\overline{v}(z)$ is time-mean velocity profile from the velocity construction (see Section 2.3.1) over the observing period. Only the $F_s(t)$ in the upper 200 m of the water column is considered as we are less confident of the estimated salinity and velocity profiles over the deeper layer. Also, eddy salt flux over the layer below 200 m is likely small (Anutaliya et al., 2017).

The $F_s(t)$ can be decomposed into two components, the first component results from the across-transect mean salinity ($< S(z,t) >$) and velocity ($< v(z,t) >$), and the second component from the spatially-fluctuating parts. The first component of the $F_s(t)$ can be computed from the across-transect mean velocity (Figure 2.3) and the across-transect mean salinity profile derived from across-transect mean satellite SSS (and using historical hydrography for subsurface structure). For each transect, two salinity lookup tables are created separately from the nearby

Table 2.1: Uncertainties associated with time series-mean (annual-mean) salt flux estimation ($\times 10^6$ kg/s) using across-transect mean and gridded velocity (v) and salinity (S) across the eastern and southern transect. The estimated time-series mean salt flux values ($\times 10^6$ kg/s) at the eastern (southern) transect is based on the gridded (across-transect mean) v and S.

	Uncertainty ($\times 10^6$ kg/s)		Estimated mean eddy salt flux ($\times 10^6$ kg/s)
	$< v(z,t) >$ and $< S(z,t) >$	Gridded v and S	
East	0.15 (0.30)	0.10 (0.19)	0.50
South	0.14 (0.20)	0.23 (0.32)	0.26

historical hydrography; the first table has the salinity profiles arranged as a function of surface velocity, while the second table has profiles arranged as a function of surface salinity. Vertical structure of a salinity profile is determined by the lookup tables (using SSS from SMAP or velocity from altimetry), and this is then scaled such that it passes through the salinity value at the surface derived from SMAP SSS and through 35.0 at 600 m depth (which is the historical mean salinity at 600 m depth at both sections). The two lookup tables were tested for robustness of the resulting salinity profile and to provide options for the $F_s(t)$ calculation. In most cases, the salinity profiles derived from the two lookup tables are similar, but the second lookup table sorted as a function of surface salinity generally provides a better result at the eastern transect while the first lookup table sorted as a function of surface velocity generally provides a better result at the southern transect. Therefore, the following discussion is based on these "best" salinity profiles determined accordingly for each transect.

Simulation with glider velocity and salinity measurements shows that the first component of $F_s(t)$ alone (calculated based on $< S(z,t) >$ and $< v(z,t) >$) accounts for 62% (83%) of the total variability at the eastern (southern) transect. The uncertainties in eddy salt flux are 0.15×10^6 and 0.14×10^6 kg/s at the eastern and southern transect, respectively (Table 2.1). Thus, the eddy salt flux component derived from the across-transect mean S and v alone likely represents the eddy salt flux for the transect quite well, particularly at the southern section.

To estimate the full $F_s(t)$ which includes the spatially along-transect varying S and v,

measurements of velocity and salinity along the transect are required. The transect-depth salinity section is estimated using the lookup tables similar to the estimation of the across-transect mean salinity profile, except the SSS is not averaged over the transect. There are six SSS measurements along each transect but no observations within ∼40 km of the coastline. SSS is extrapolated toward the coast where the measurement is not available as a constant from the nearest available SSS measurement. Along each PIES transect, beginning at the coast, the SSS is interpolated to four equally spaced (∼45 km) grid points. Velocity profiles in each grid along the transect are interpolated using the altimetry-derived surface velocity and the two leading EOFs computed from the glider velocity profiles. The velocity profile in each grid along the transect is constructed as a linear combination of the two EOFs constrained by the surface velocity where the transect-depth sum of velocity in the surface (0-200 m depth) and subsurface (200-600 m depth) layers is equal to the volume observed by the PIES and the minimized rms of velocity in the subsurface layer.

The uncertainties associated with $F_s(t)$ estimation are evaluated by comparing $F_s(t)$ estimated by the glider salinity and velocity measurements to that derived from the method described above simulated with the glider surface velocity, surface salinity, and volume transport in the surface and subsurface layers. At the eastern transect, using along-transect variable (gridded) salinity/velocity estimation improves the estimation of $F_s(t)$ compared to the case using the across-transect mean velocity and across-transect mean salinity alone. The gridded $F_s(t)$ estimation explains 88% of the eddy transport variability. The time-mean rms error also decreases to 0.10×10^6 kg/s (Table 2.1). At the southern transect, the gridded salinity/velocity $F_s(t)$ estimation only explains 53% of the eddy transport variability and the time-mean rms error increases to 0.23×10^6 kg/s (Table 2.1). The higher uncertainty along the southern transect reflects the inability of the gridded salinity/velocity estimation to replicate the vertical structure of the salinity and velocity sections. Indeed, the glider measurements along the southern transect show that the salinity and velocity in the upper 200 m of the water column are quite complex; a subsurface salinity maximum is sometimes present between 40-120 m depth, while the velocity section often

shows subsurface reversing flow. Therefore, $F_s(t)$ at the eastern transect is determined from the gridded velocity and salinity profiles, while that at the southern transect is determined from the across-transect mean velocity and salinity profiles.

2.4 Results

2.4.1 Flow across the eastern section

Overall description

The surface-layer volume transport along the eastern coast of Sri Lanka ranges from -23.2 to 27.1 Sv (positive northward) with a mean of -0.8 Sv over the period of November 2014 - March 2019 (Figure 2.4a). In the subsurface layer, the mean volume transport is -4.0 Sv ranging from -28.6 Sv to 20.2 Sv. The subsurface current occasionally flows in the opposite direction to the surface current (Figure 2.3a); the correlation between the surface and subsurface flow is 0.74 and is significant at the 95% confidence level. The continuous observations and the reconstructed velocity profiles off the eastern coast of Sri Lanka confirm the *surface* circulation variability found by previous observational studies (e.g. Hacker et al., 1998; Shankar et al., 2002; de Vos et al., 2014; Wijesekera et al., 2015; Lee et al., 2016); the surface current reverses its direction twice a year flowing southward during the monsoon seasons and northward during transition periods (Figure 2.3a, 2.4a). Our PIES observations and PIES/altimetry velocity reconstruction yield the first continuous velocity observations in the upper 600 m of the water column off the eastern coast of Sri Lanka. In the following subsections, we will describe its variability.

Seasonal variability

During the southwest monsoon, the surface flow along the Sri Lankan eastern coast is southward as it is dominated by the SLD (Shankar et al., 2002; de Vos et al., 2014) arising from

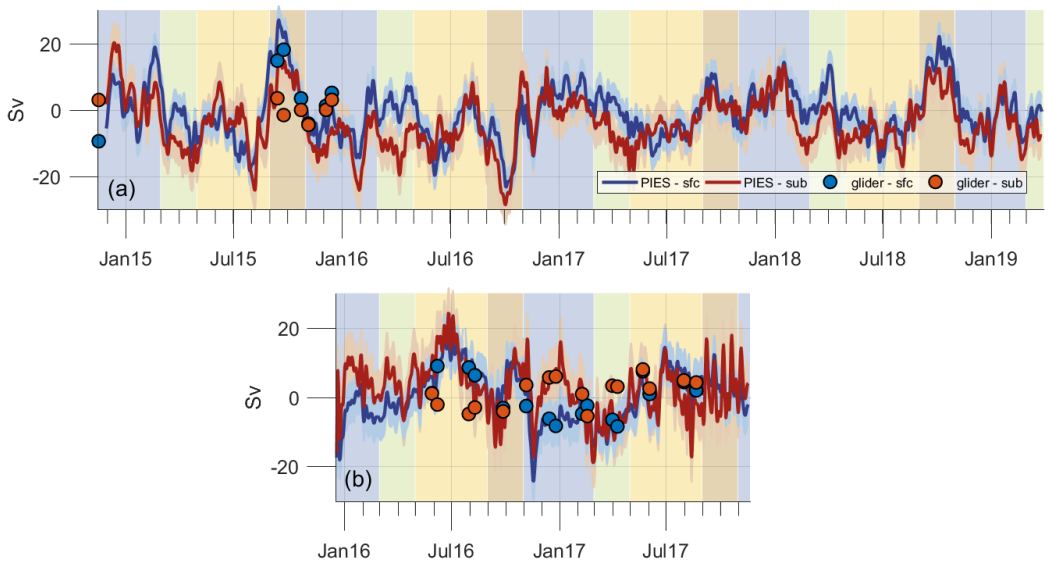

Figure 2.4: Volume transport (Sv) across the transect off the eastern (a) and southern coast (b) over the 0-200 m (blue) and 200-600 m (red) depth layers estimated from PIES measurements and satellite SLA with the associated uncertainty (blue and red shading) and that estimated from the Seaglider measurements (blue and red dots). Background shading designates northeast monsoon season (blue), spring monsoon transition (green), southwest monsoon (yellow), and fall monsoon transition (brown).

westward-propagating Rossby waves and Ekman pumping over the BoB (Vinayachandran et al., 1999). Our PIES measurements show that the southward-flowing flank of the SLD is quite strong; it transports 14-20 Sv in the upper 200 m of the water column (Figure 2.4a), although most of the volume is circulated back northward into the BoB (Figure 2.1). The southward flow usually extends to the deepest observed depth at 600 m and the opposing subsurface flow, as found in a previous observational and numerical study (Anutaliya et al., 2017), is only briefly apparent at the transect in June 2015 (Figure 2.3a). The PIES data may miss some occasions of the subsurface counterflow since the eastern PIES transect (81.75°-83.4°E) is quite wide and can include southward flow in the region east of 83°E obscuring the northward undercurrent that is usually confined to the west of 83°E. During the fall monsoon transition, surface northward flow along Sri Lankan east coast is present every year except in 2016 (Figure 2.3a, 2.4a). The northward-flowing surface current, influenced by the arrival of Rossby waves propagating from the eastern boundary of the BoB (Sreenivas et al., 2012), is present in agreement with that found in surface satellite altimetry observations (Eigenheer and Quadfasel, 2000; Durand et al., 2009; Lee et al., 2016). The reconstructed velocity profile shows that the northward flow is not only present at the surface but also extends over the observed 0-600 m depth layer (Figure 2.3a).

The southward EICC off the Sri Lankan east coast that has been previously observed (Shetye et al., 1996; Wijesekera et al., 2015) is apparent for $\sim$1-2 months between October and January (roughly the northeast monsoon season) in every year of the PIES record (Figure 2.3a). The EICC is strongest near the surface and extends to the deepest observed depth of 600 m which is comparable to that derived from a single hydrographic survey at 11°N (Shetye et al., 1996). The surface velocity derived from satellite altimetry shows that the EICC does not always extend over the whole PIES transect (not shown) and thus the two PIES at the transect end-points may not always fully capture the EICC that varies in width. The transect can sometimes also include circulation in the interior of the BoB, and thus the estimated volume transport and mean across-transect velocity might underrepresent the strength of the EICC along the eastern coast of

Sri Lanka. During the spring transition, the westward-flowing North Equatorial Current (NEC) is present in the southern BoB at 5°-8°N (Cutler and Swallow 1984; Wijesekera et al., 2016; Figure 2.1) and bifurcates at the southeastern coast of Sri Lanka (Shetye et al., 1993; Hacker et al., 1998). The bifurcation produces the observed northward surface flow along the eastern coast (Figure 2.4; Eigenheer and Quadfasel, 2000; Durand et al., 2009; Anutaliya et al., 2017). The reconstructed velocity profile shows that the northward current is usually confined to the upper 150-250 m of the water column (Figure 2.3a). Below the northward surface layer, a southward-flowing undercurrent is apparent every year of the PIES observing period, consistent with the previous study of Anutaliya et al. (2017) that is based on sporadic observations and numerical simulations.

Year-to-year variability

To examine year-to-year variability of the surface flow along the eastern coast of Sri Lanka, the 4-year seasonal cycle and signal with frequencies higher than 120 days are removed from the transport time series (Figure 2.5). The transport is compared to the low frequency component ($>$120 days) of the dipole mode index (DMI) that indicates IOD activity (Saji et al., 1999) and mean sea surface temperature in the Niño 3.4 region. The correlation between the transport anomaly and the DMI is 0.65 (significant at the 95% confidence level) indicating that an anomalous southward flow occurs during a negative IOD (nIOD) event. A nIOD event developed in June 2016 and reached its peak in October 2016. Negative IOD events are often associated with weakening of the easterlies over the equatorial IO in August - September (Saji et al., 1999; Schott et al., 2009) which results in the development of strong downwelling Kelvin waves at the eastern boundary and around the coastal rim of the BoB (Sreenivas et al., 2012). This flow opposes the seasonal northward flow during the fall monsoon transition, and thus, the northward flow is absent during the nIOD in 2016, consistent with previous numerical studies (Thompson et al., 2006; Dandapat et al., 2018). El Niño conditions potentially strengthen the northward flow during the fall monsoon transition and weakens the southward-flowing EICC during the northeast

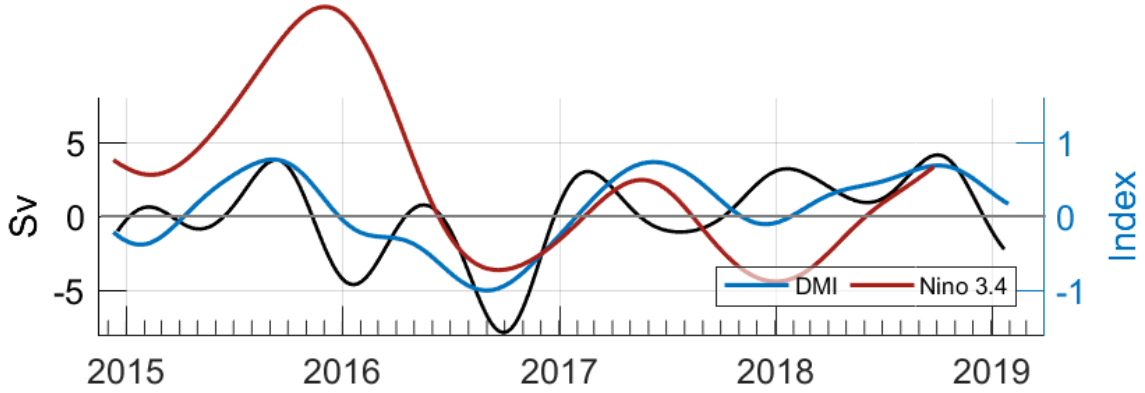

Figure 2.5: Volume transport (Sv) along the Sri Lankan eastern coast with the seasonal cycle and frequencies higher than 120 days removed (black), the 120-day lowpass filter dipole mode index (DMI; blue), and the Niño 3.4 index (maroon).

monsoon (Pant et al., 2015) due to a suppression of the seasonal downwelling Kelvin waves (Sreenivas et al., 2012). However, the transport anomaly during the 2015/2016 El Niño does not exhibit strong deviation from the seasonal cycle (Figure 2.5). The correlation with Niño 3.4 index is also low ($r = 0.01$) and not significant at the 95% confidence level.

Eddy salt flux at the Sri Lankan eastern coast

The estimated eddy salt transport ($F_s(t)$) across the eastern section in the upper 200 m of the water column agrees with that calculated from the few overlapping glider measurements, and gives a mean value (eddy salt flux) from April 2015 to December 2018 (when the SMAP

SSS is available) of 0.50×10^6 kg/s (Figure 2.6a; Table 2.1). A positive time-mean eddy salt flux indicates that either fresher water is being transported southward or more saline water is being transported northward along the Sri Lankan eastern coast; both conditions result in an increase of the salinity in the BoB. The estimated $F_s(t)$ exhibits high seasonal and year-to-year variability. The seasonal cycle in $F_s(t)$, constructed as the sum of the annual and semiannual harmonics, explains 21% of the total variance. The seasonal cycle exhibits a maximum in November and minimum negative salt transport in March (Figure 2.6a). The low-frequency (>300 days) component of $F_s(t)$ explains 7% of the total variability.

The mean eddy salt fluxes for the individual years over the observing period are positive and vary from 0.26 to 0.84×10^6 kg/s with an uncertainty of 0.19 $\times10^6$ kg/s (Table 2.2). The largest annual flux is observed in 2015. It is largely due to a positive salt transport event of 7.3×10^6 kg/s during the fall monsoon transition when anomalously saline water (relative to the time-mean value) is transported northward by the seasonal current along the eastern coast of Sri Lanka (Figure 2.3a, 2.4a). A brief period of positive salt transport occurs in November 2015 when the EICC is present and is transporting freshwater southward (Figure 2.6a). Note that the 2015 annual-mean eddy salt flux calculation is based on the salt flux estimation only from April to December due to the availability of the SMAP SSS, but the time-mean eddy salt flux over the missing months (January - March) is usually small (Figure 2.6a). Although the high annual eddy salt flux in 2015 coincides with the 2015/2016 El Niño, the influence of El Niño events on eddy salt flux along the eastern coast of Sri Lanka cannot be conclusively determined from our present four-year dataset. Note also the low correlation between Niño 3.4 index and the volume transport anomaly (Figure 2.5). However, interannual SSS variability in other parts of the BoB, e.g. the northeastern and central BoB, have proven to be unrelated to ENSO events (Chaitanya et al., 2015; Pant et al., 2015).

From 2016 to 2018, a positive eddy salt transport occurs twice a year: in the late spring monsoon transition into the southwest monsoon (May - August) and in the early northeast

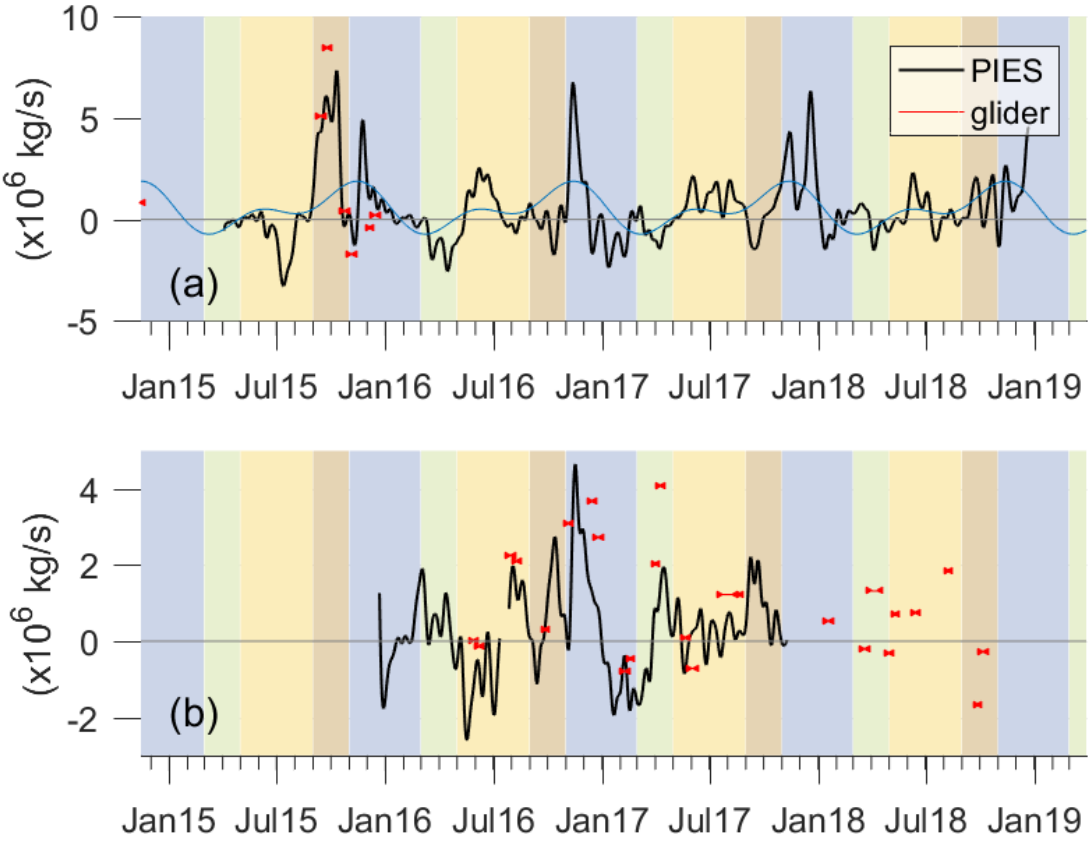

Figure 2.6: Estimated eddy salt flux (kg/s) at the eastern coast computed from gridded velocity and salinity profiles (a) and southern coast computed from across-transect mean velocity and salinity profiles (b) of Sri Lanka derived from glider measurements (red) and from PIES, satellite altimetry, and SMAP SSS (black). The length of the red line represents the time the glider took to complete the crossing. The seasonal cycle of eddy salt flux at the eastern section, constructed as the sum of the annual and semiannual harmonics, is plotted in blue. Background shading designates northeast monsoon season (blue), spring monsoon transition (green), southwest monsoon (yellow), and fall monsoon transition (brown).

Table 2.2: Annual-mean eddy salt flux ($\times 10^6$ kg/s) computed from gridded velocity and salinity profiles along the eastern coast of Sri Lanka over the observing period. Note that the average in 2015 only includes the salt flux estimation from April to December.

Annual mean salt flux ($\times 10^6$ kg/s)	
2015	0.84
2016	0.26
2017	0.56
2018	0.40

monsoon (November - December) with a bigger transport occurring during the northeast monsoon. During these periods, low-salinity water is transported southward along the coast. Recall that the satellite SSS does not capture salinity within 40 km of the coast. Since the EICC that transports freshwater southward is often confined to within $\sim$100 km of the coastline (Wijesekera et al., 2015), the estimated eddy salt transport during the northeast monsoon is likely underestimated. The smallest annual-mean salt flux of 0.26×10^6 kg/s is found in 2016 coinciding with a nIOD event. Typically, nIOD conditions are associated with anomalously southward flow during the fall monsoon transition and northeast monsoon seasons (Sreenivas et al., 2012; Pant et al., 2015), as well as anomalously low freshwater input into the BoB (Durand et al., 2011). This potentially results in an anomalously small amount of available freshwater exported during the northeast monsoon. During the 2016 nIOD event, the seasonal northward current along the Sri Lankan eastern coast that transports saline water into the BoB during the fall monsoon transition is absent (Figure 2.3a, 2.4a, 2.6a). While the current is anomalously southward in October 2016 (Figure 2.3a, 2.5), the SSS shows small deviation from the time mean value resulting in a weak negative salt transport. Also, an extended negative eddy salt transport is present in March - April with a magnitude of 2-3$\times10^6$ kg/s (Figure 2.6a).

In 2018, the positive eddy salt flux during the southwest monsoon is weaker than that during 2016-2017 due to the presence of slightly fresher water (relative to the time-mean salinity) and weak southward-flowing branch of the SLD at the Sri Lankan eastern coast. However, a

higher positive salt transport is observed during the fall monsoon transition of 2018 compared to the previous two years as saline water along the eastern coast is transported northward by the seasonal northward-flowing current (Figure 2.3a, 2.4a). The PIES observations highlight positive salt transport along the eastern coast of Sri Lanka occurs not only during the monsoon seasons, as found in previous studies (Vinayachandran et al., 1999; Han and McCreary, 2001; Vinayachandran et al., 2013; Wijesekera et al., 2015; Sanchez-Franks et al., 2019), but high positive salt transport also occurs during the fall monsoon transition in some years, e.g. 2015 and 2018.

2.4.2 Flow across the southern section

Overall description

Along the southern coast of Sri Lanka, the mean current in the upper 200 m of the water column is -0.2 Sv (positive eastward) over the period of December 2015 - November 2017 (Figure 2.4b). The surface flow reaches a minimum of -24.2 Sv and a maximum of 18.4 Sv. The subsurface flow ranges from -18.8 Sv to 24.2 Sv and has a mean of 2.3 Sv. The correlation coefficient between the surface and subsurface volume transport is 0.65, significant at the 95% confidence level. During the observing period, flow off the southern coast exhibits a strong seasonal cycle in the surface layer and is dominated by an eastward-flowing current in June - October and a westward-flowing current in November - May consistent with observations of the surface current based on surface satellite altimetry (Eigenheer & Quadfasel, 2000; Durand et al., 2009). In contrast to the surface layer, the subsurface flow does not show a distinct seasonal cycle.

Seasonal variability

The eastward SMC is present off the southern coast of Sri Lanka during the southern monsoon and fall transition (June - October) with a maximum surface flow of 13.6 - 24.0 Sv

in June of both years (Figure 2.4b). The eastward flow is surface intensified and can extend to the deepest observed depth of 600 m (Figure 2.3b). There is little evidence of a connection between the circulation off the Sri Lankan southern and the eastern coasts during the summer monsoon as the seasonal SLD often occupies the region off the eastern coast of Sri Lanka and so southward flow is dominant (Figure 2.1, 2.3a). The satellite altimetry suggests that the eastward SMC flows into the BoB at ∼85.5°E during the southwest monsoon, consistent with previous observations (Vinayachandran et al., 1999; Wijesekera et al., 2016). In September of 2017, the satellite altimetry shows a weak connection of the boundary currents along the southern and eastern coasts of Sri Lanka; the eastward-flowing SMC turns northward, centered at ∼83.5°E at 8°N.

During the winter monsoon and spring transition (November - May), flow off the southern coast is dominantly westward. A maximum westward flow of 18.0 and 24.2 Sv is present in December 2015 and November 2016, respectively. These periods of maximum westward flow also coincide with instances when southward flow is observed along the eastern coast of Sri Lanka suggesting a connection between the EICC and the WMC (Figure 2.1, Figures 2.4 and 2.3). The satellite surface geostrophic velocity also confirms the westward pathway of the surface EICC around the Sri Lanka southern coast during these periods (not shown). However, the continuous flow along the Sri Lankan eastern and southern coasts persists over only a relatively short period (∼1 month) as the circulation off the southeastern coast of Sri Lanka is often affected by a reflective Rossby wave from the eastern boundary of the BoB during this season (Vinayachandran et al., 2005b). The westward propagation of the wave from the eastern boundary of the BoB is also apparent in the satellite altimetry (Sreenivas et al., 2012). The arrival of the Rossby waves causes high sea surface height in the southern central BoB producing two effects. First, it reduces positive sea surface height gradient along the eastern transect toward the Sri Lankan coast weakening the EICC. Second, part of the EICC turns eastward flowing around the area of high sea surface height in the southern central BoB leaving only a weak westward flow along the

southern coast (Vinayachandran et al., 2005b).

Eddy salt flux at Sri Lankan southern coast

The time-mean eddy salt flux at the Sri Lankan southern coast is 0.26×10^6 kg/s in the upper 200 m of the water column indicating either westward flowing low-salinity water or eastward flowing high-salinity water (Figure 2.6b; Table 2.1). The variability of the eddy salt transport ($F_s(t)$) estimate based on PIES, satellite altimetry, and SMAP SSS is consistent with that estimated from glider measurements, although the magnitude of the PIES $F_s(t)$ is sometimes smaller. The inconsistency is mainly a consequence of the subsurface salinity profile that shows large variation and so cannot be successfully replicated by our simple construction (Section 2.3.2; Table 2.1). For example, the glider shows that the layer of salinity with values less than 35.0 extends to 180 m depth in April 2017 while it only extends to 60 m depth in December 2016 - this cannot be captured with our method. During the PIES observing period, positive eddy salt transport is observed in the spring monsoon transition, the late summer monsoon/ fall transition, and in the winter monsoon. The flow along the Sri Lankan southern coast transports low-salinity water westward during the spring monsoon transition, while the opposite is observed during the fall monsoon transition (Figure 2.6b). During the winter monsoon (November - December 2016), the biggest positive $F_s(t)$ of 4.6×10^6 kg/s is observed; the positive $F_s(t)$ corresponds to strong westward flow transporting anomalously freshwater that is associated with the EICC. In 2018, only glider measurements are available to confirm the presence of a positive $F_s(t)$ during the winter monsoon in January, the spring monsoon transition in April - June, and at the end of the southwest monsoon in August (PIES data were only just recovered). Negative $F_s(t)$ is present during the 2018 fall monsoon transition (September - October).

2.5 Discussion

2.5.1 Eddy salt flux along the eastern and southern coasts of Sri Lanka

As estimated from climatology, reanalysis products and numerical simulation, the long-term estimate of annual freshwater input into the BoB is ∼0.13 Sv (Rao and Sivakumar, 2003; Sengupta et al., 2006; Wilson and Riser, 2016) which translates into $\sim 4.5 \times 10^6$ kg/s of salt input to maintain the salinity balance in the BoB. Our measurements show that the 4-year mean eddy salt flux along the eastern coast of Sri Lanka contributes approximately 11% of the estimated BoB annual salt input, while the 2-year mean eddy salt flux along the southern coast contributes about 6% to the annual salt budget (Table 2.1). During the overlapping period, the correlation between salt fluxes along the eastern and southern coasts is low ($r = 0.12$) but significant at the 95% confident level (Figure 2.6).

Eddy salt transport during the monsoon seasons

Our PIES observations show the presence of the EICC along the eastern and southern coasts of Sri Lanka that transports freshwater out of the BoB (Figure 2.3, 2.4, 2.6) consistent with previous studies (Han and McCreary, 2001; Wijesekera et al., 2015). In 2016 when the EICC is observed at both transects, relatively fresh water is transported southward along the Sri Lankan eastern coast and westward along the southern coast resulting in an eddy salt transport of nearly 5×10^6 kg/s (Figure 2.6). However, the BoB saline water import during the southwest monsoon as determined from a hydrography survey, salinity climatology, and model simulations (Vinayachandran et al., 2013; Vinayachandran et al., 1999; Han and McCreary, 2001; Sanchez-Franks et al., 2019) is not observed by the southern PIES and satellite measurements, although the PIES clearly measure the SMC (Figure 2.3b, 2.4b). In June - July 2016 and July - August 2017, the satellite SSS does not exhibit a strong positive salinity anomaly associated with the eastward-flowing SMC resulting in a small positive or negative $F_s(t)$ (Figure 2.6b). Toward the

end of the southwest monsoon/ beginning of the fall monsoon transition, however, the estimated $F_s(t)$ shows a positive signal along the southern coast that is associated with the eastward transport of highly saline water, consistent with previous numerical results (Jensen, 2001b; Jensen 2003).

Eddy salt transport during the spring and fall monsoon transition

During the fall monsoon transition of the overlapping observing period in 2016 - 2017, the PIES observations provide little to no evidence of a continuous flow of water along the southern and eastern coast of Sri Lanka (Figure 2.6). In 2016, an anomalous year (section 2.4.1), eastward flow is briefly present along the southern coast in October transporting saline water (Figure 2.3b, 2.6b); however, flow along the eastern coast is southward (Figure 2.3a) resulting in a convergence at the southeastern coast of Sri Lanka. A connection between flow along the Sri Lankan eastern and southern coasts occurs for a short period in September 2017 (Figure 2.1, 2.3, 2.6). Still, the northward current along the eastern coast transports much fresher water (salinity of 33.1-33.2) compared to that along the southern coast where the salinity is 34.6-34.8. The altimetry-derived circulation shows that the eastward current that turns northward along the eastern coast is centered at $\sim$83.5°E in 2017 and the observed northward flow along the eastern coast likely transports the freshwater associated with the SLD during the previous southwest monsoon. In contrast, the PIES at the eastern transect, satellite altimetry, and satellite SSS suggest that saline water is being imported into the BoB along the southern and eastern coasts of Sri Lanka during the fall transition in 2015 and 2018 as the eastward-flowing surface current sharply turns northward to flow along the eastern coast centered at $\sim$82°E. The northward flow also transports anomalously saline water originating from the low-latitude region (to the south of 5°N) of the central or western Arabian Sea (to the west of 70°E) along the eastern coast of Sri Lanka (Figure 2.3a, 2.6a) as shown by the satellite measurements. This is consistent with a previous numerical study that indicated that the origin of saline water imported during the southwest monsoon is from the western equatorial Indian Ocean (Sanchez-Franks et al., 2019). Thus, large year-to-year variability of eddy salt

transport along the eastern and southern coasts of Sri Lanka during the fall monsoon transition depends heavily on location of the SMC. Also, the PIES observations highlight the role of saline water imported into the BoB via the boundary currents during the fall transition of some years.

Although a positive eddy salt transport of $\sim 2 \times 10^6$ kg/s associated with westward freshwater transport is present at the southern transect during the spring monsoon transition (Figure 2.6b), the PIES volume transport and satellite SSS suggest no connection between the eddy salt transport at the southern and eastern coast of Sri Lanka (Figure 2.3, 2.6). The positive eddy salt transport along the southern coast is likely dominated by the westward-flowing NEC that transports freshwater from the central or the eastern boundary of the BoB as observed by mooring measurements (Wijesekera et al., 2016). The mooring observations also show that the NEC is the strongest and associated with a strong freshwater anomaly at the southern-most mooring located at 6°N, 85.5°E while a weaker current associated with a smaller freshwater anomaly is observed at 8°N, 85.5°E. This results in small eddy transport with a magnitude smaller than 0.8×10^6 kg/s observed during the spring monsoon transition at the PIES eastern transect.

2.5.2 Eddy salt flux in the region within 40 km of the Sri Lankan coasts

As the satellite measured SSS is highly contaminated near the coast (Grodsky et al., 2018), the SSS within 40 km of the Sri Lankan eastern and southern coasts is not observed. However, the importance of salt flux in the coastal region cannot be neglected, particularly during the northeast monsoon when the strong and narrow EICC transports low-salinity water out of the Bay of Bengal (Han and McCreary, 2001; Wijesekera et al., 2015). While our eddy salt flux estimation is based on constant extrapolation of SSS toward the coasts, near-coast SSS observations from a few available Seaglider crossings (not shown) and historical hydrography surveys show that the SSS often gets lower toward the coast during the northeast monsoon (Donguy and Meyers, 1996; Rao and Sivakumar, 2003). One glider crossing at the southern section in January 2018 shows a lower SSS of nearly one salinity unit at 5.8°N compared to the most nearshore SSS

measured by the satellite at 5.4°N. Numerical simulation also suggests the presence of intensified low-salinity water toward the coasts (Vinayachandran et al., 2005a; Jensen et al., 2016) as forced by the difference between precipitation and evaporation over the BoB and river runoffs (Han and McCreary, 2001). During the fall monsoon transition when high-salinity water is transported northward into the BoB during some years (Figure 2.6a), SSS is also generally higher toward the coast as suggested by historical hydrographic surveys (Rao and Sivakumar, 2003) and numerical simulation (Jensen, 2001). Thus, the estimated eddy salt transport (Figure 2.6) likely serves as a lower bound during these high eddy flux seasons.

2.6 Summary

The study shows the effectiveness of PIES observations for continuously monitoring the volume transport along the eastern and southern coasts of Sri Lanka (Figure 2.4), although we note that the presence of only two PIES at each transect and does not always adequately capture the boundary current. When the boundary current is occasionally narrower than the PIES section, the estimated volume transport will include opposing currents in the interior of the BoB resulting in an underestimation of the boundary current transport. Simple simulations using glider measurements show that an addition of two more PIES along each transect would significantly reduce the transport uncertainty associated with the varying width of the boundary current from 3.7 Sv to 0.7 Sv.

Together with the satellite SSS, the PIES measurements and satellite altimetry provide a sensible estimate for the eddy salt flux at these sections (Figure 2.6), particularly along the Sri Lankan eastern coast. Glider measurements indicate that both velocity and salinity structures at the southern transect are more complex and our simple estimation technique is not quite sufficient to provide accurate salt flux estimation along that transect. At the eastern section, the estimated salt flux shows high seasonal and interannual variability (Figure 2.6a). It also compares well

with the eddy salt flux computed from the Seaglider measurements, although the SSS used in our calculation does not include values within ∼40 km offshore. With the boundary currents that are sometimes confined within 100 km off the Sri Lankan coast, such as the EICC, continuous SSS measurements near the coast could further improve the estimation of eddy salt flux.

2.7 Acknowledgement

This work is supported by the US Office of Naval Research (ONR) as part of two ONR Departmental Research Initiatives: Air-Sea Interactions Regional Initiative (ASIRI) and Northern Arabian Sea Circulation - autonomous research (NASCar) projects through ONR grants N00014-14-1-0629 (A. Anutaliya and U. Send), N00014-15-1-2189 (J. L. McClean), N00014-16-1-2313 (J. Sprintall). Hydrographic profiles are from the National Center of Environmental Information (Boyer et al., 2013) (https://www.nodc.noaa.gov/access/index.html). Argo data were collected and made freely available by the International Argo Program and the national programs that contribute to it (http://www.argo.ucsd.edu, http://argo.jcommops.org). The Argo Program is part of the Global Ocean Observing System. This study has been conducted using E.U. Copernicus Marine Service Information (http://marine.copernicus.eu/services-portfolio/access-to-products/?option=com_csw&view=details&product_id=SEALEVEL_GLO_PHY_L4_REP_OBSERVATIONS_008_047). SMAP salinity data are produced by Remote Sensing Systems and sponsored by the NASA Ocean Salinity Science Team. Data are available at www.remss.com.

Chapter 2 is a draft of manuscript in preparation for submission as “PIES observations of flows off the Sri Lankan eastern and southern coast”, by A. Anutaliya, U. Send, J. L. McClean, and J. Sprintall. The dissertation author was the primary investigator and author of this work.

Chapter 3

An Undercurrent off the East Coast of Sri Lanka

Abstract

The existence of a seasonally varying undercurrent along 8° N off the east coast of Sri Lanka is inferred from shipboard hydrography, Argo floats, glider measurements, and two Ocean General Circulation Model simulations. Together, they reveal an undercurrent below 100-200 m flowing in the opposite direction to the surface current that is most pronounced during boreal spring and summer and switches direction between these two seasons. The volume transport of the undercurrent (200-1000 m layer) can be more than 10 Sv in either direction, exceeding the transport of 1-6 Sv carried by the surface current (0-200 m layer). The undercurrent transports relatively fresh water southward during spring, while it advects more saline water northward along the east coast of Sri Lanka during summer. Although the undercurrent is potentially a pathway of salt exchange between the Arabian Sea and the Bay of Bengal, the observations and the OGCMs suggest that the salinity contrast between seasons and between the boundary current and interior is less than 0.09 in the subsurface layer, suggesting a small salt transport by the

undercurrent of less than 4% of the salinity deficit in the Bay of Bengal.

3.1 Introduction

Knowledge of the circulation in the southern Bay of Bengal (BoB) is crucial to understanding the contrasting salinity distributions of the Arabian Sea (AS) and the BoB since it controls the amount of water and salt exchanged between the two ocean basins. Observations and modeling studies have confirmed the role of the surface current along the Sri Lankan east coast in distributing mass and salt between the AS and the BoB. Drifters indicate that a strong surface-intensified current to the east of Sri Lanka during the northeast monsoon (November-January) transports low-salinity water out of the BoB toward the AS around the south coast of Sri Lanka (Wijesekera et al., 2015). An ocean general circulation model (OGCM) study also shows that significant mass and salt transport occur between the AS and the BoB along the eastern and southern coast of Sri Lanka (Jensen et al., 2016).

The surface current to the east of Sri Lanka is influenced by local alongshore winds, remote winds in the vicinity of the northern and eastern boundaries of the BoB, equatorial waves, and interior Ekman pumping (Yu et al., 1991; Shetye et al., 1993; McCreary et al., 1996; Shankar et al., 1996; Vinayachandran and Yamagata, 1997). This current has a strong seasonal pattern (Shankar et al., 2002; Lee et al., 2016) with recirculation loops that are highly variable in time and space (Durand et al., 2009). Some of the recirculations appear seasonally, such as the Sri Lanka Dome (SLD), a cyclonic eddy that is well developed in July (Vinayachandran and Yamagata, 1997). The SLD is driven by Rossby waves radiating from the eastern boundary and intensified Ekman pumping inside the BoB (Vinayachandran et al., 1999; Shankar et al., 2002; de Vos et al., 2014). The SLD propagates westward (Wijesekera et al., 2016b) toward the east coast of Sri Lanka resulting in a southward coastal surface flow during early summer. In October, the prevailing wind in the BoB starts reversing direction and blows southwestward. This marks the

start of the northeast monsoon when the local wind along the east coast of India drives the East India Coastal Current (EICC) southward with speeds exceeding 1 m s^{-1} extending from the east coast of India southward to the southern tip of Sri Lanka (Shetye et al., 1996; Wijesekera et al., 2015).

The subsurface circulation in this region is also potentially important as high-salinity water from the AS can be subducted beneath the fresher surface water originating from river runoff and precipitation in the northern BoB (Rao & Sivakumar, 2003; Sengupta et al., 2006; Vinayachandran et al., 2013; Gordon et al., 2016; Jensen et al., 2016); this is evident in observations and model studies both during the northeast (Wijesekera et al., 2015) and southwest monsoons (June- August) (Wijesekera et al., 2016b). Little is known about the subsurface structure of the boundary current along the east coast of Sri Lanka. Mooring observations show a reversing subsurface current occurring off the southern coast of Sri Lanka; it is most distinct during boreal spring and summer (Schott et al., 1994). In addition, reversal of the EICC along the east coast of India is observed below 100 m that is southward during the southwest monsoon and northward during the northeast monsoon, with the winter undercurrent being a more permanent feature (Mukherjee et al., 2014). The direction of this undercurrent is in good agreement with findings from a linear, continuously stratified ocean model (LSM) (McCreary et al., 1996). The LSM also suggests the presence of an undercurrent along the Sri Lankan east coast (centered at 8° N) that reverses its direction twice a year with model speeds ranging from 6 cm s^{-1} equatorward during boreal spring to 8 cm s^{-1} poleward during summer. This undercurrent has not been observed before and will be the focus of this study. We will investigate the vertical structure and seasonal variability of subsurface flows in the boundary current system off the eastern coast of Sri Lanka using OGCMs as well as observations from shipboard hydrography, Argo floats, and glider measurements. Knowledge of the vertical structure, variability, and associated dynamics of the boundary current will contribute to a better understanding of mass and salt exchanges in the northern Indian Ocean.

3.2 Data and Methodology

Shipboard hydrography and Argo Conductivity-Temperature-Depth (CTD) profiles, together with satellite altimeter-derived surface absolute dynamic topography (ADT), were used to determine the vertical structure of the current east of Sri Lanka. There were 13 shipboard hydrography and 116 Argo profiles available between 7-9° N and within 130 km of the Sri Lankan east coast that sampled to at least 1000 m depth (Figure 3.1). The hydrographic profiles were collected over the period of 2008-2017 while the Argo profiles were collected over 2007-2017. The gridded delayed-time ADT products were derived from Archiving, Validation, and Interpretation of Satellite Oceanographic (AVISO) Data (Ducet et al., 2000) which are available over the period of 1993-2016 with spatial and temporal resolutions of $1/4°$ latitude $\times$ $1/4°$ longitude and 7 days, respectively.

The hydrography-Argo based mean seasonal absolute geostrophic meridional velocity profiles were calculated by combining sheared velocity profiles from hydrography and Argo measurements and surface velocity from the ADT products. The number of hydrography and Argo profiles available were too few to calculate robust estimates of monthly meridional geostrophic velocity. Hence, to derive the seasonal sheared velocity profiles, we used 2-month (i.e. bimonthly) sliding mean dynamic heights calculated from hydrography-Argo profiles located to the west and east of the central position of the boundary current (Figure 3.1a); the position of the boundary current was determined from a longitude-depth velocity transect along 8° N derived from glider measurements and OGCMs (for example, Figure 3.2). The low-pass filtered geostrophic meridional sheared velocity profile is thus proportional to the corresponding difference between the eastern and western filtered dynamic heights. The number of hydrography and Argo profiles available in each bimonth period varied from 3 to 14 in the western region and from 4 to 24 in the eastern region (Figure 3.1b). The equally low-passed surface meridional velocity from the satellite ADT along 8° N between 81.75° E-82.5° E was added to the sheared profiles to yield

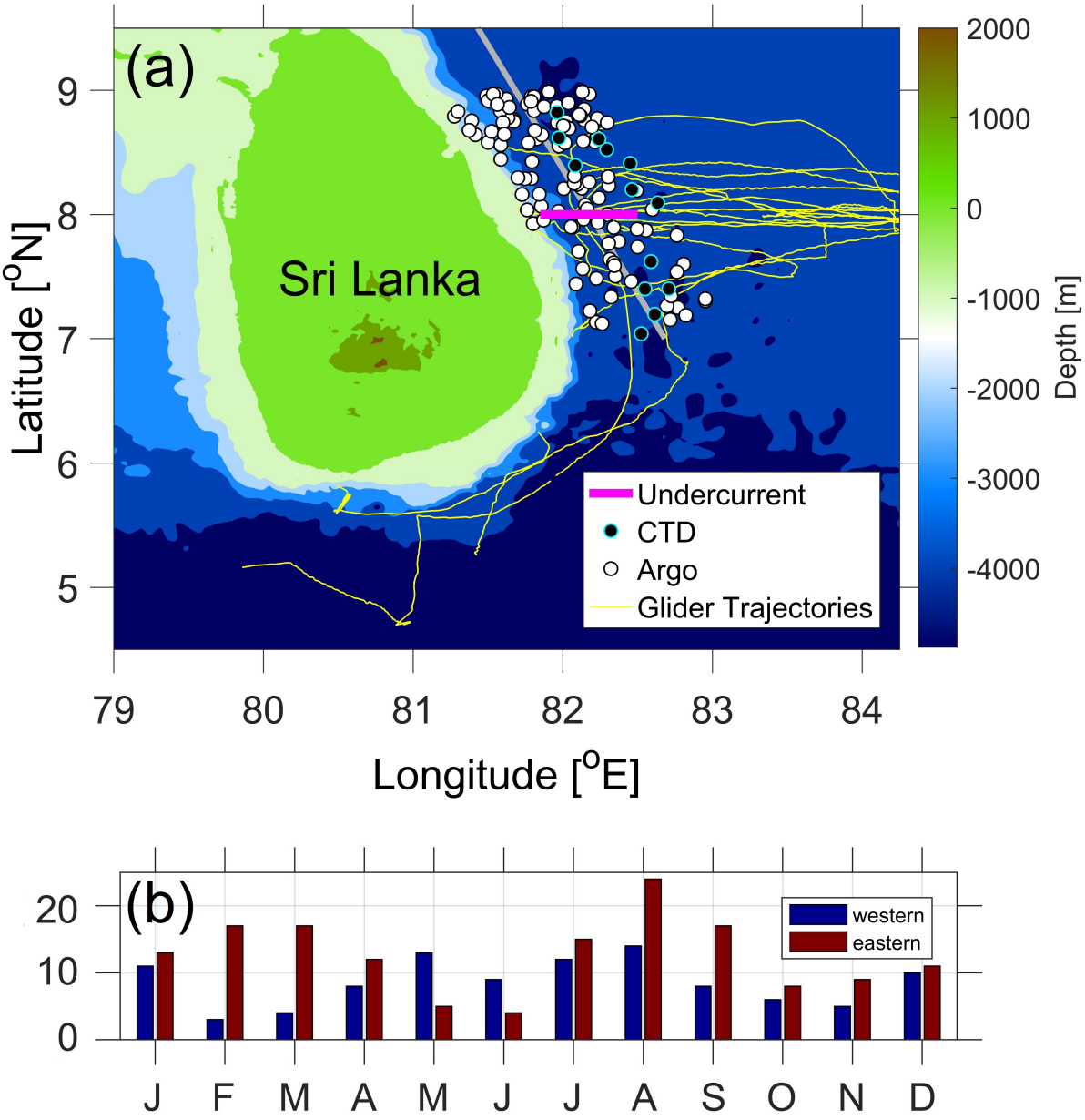

Figure 3.1: Bathymetry around Sri Lanka (a) with the location of the shipboard hydrography measurements (black dots), Argo profiles (white dots), and glider measurement transects (yellow lines). The grey line divides hydrography and Argo measurements into the eastern and western sectors used in the seasonal mean dynamic height calculation. The OGCM outputs are interpolated along 8° N (magenta line). The number of hydrography and Argo profiles available in the mean dynamic height calculation for each month for the eastern (red) and western (blue) sectors are shown in (b).

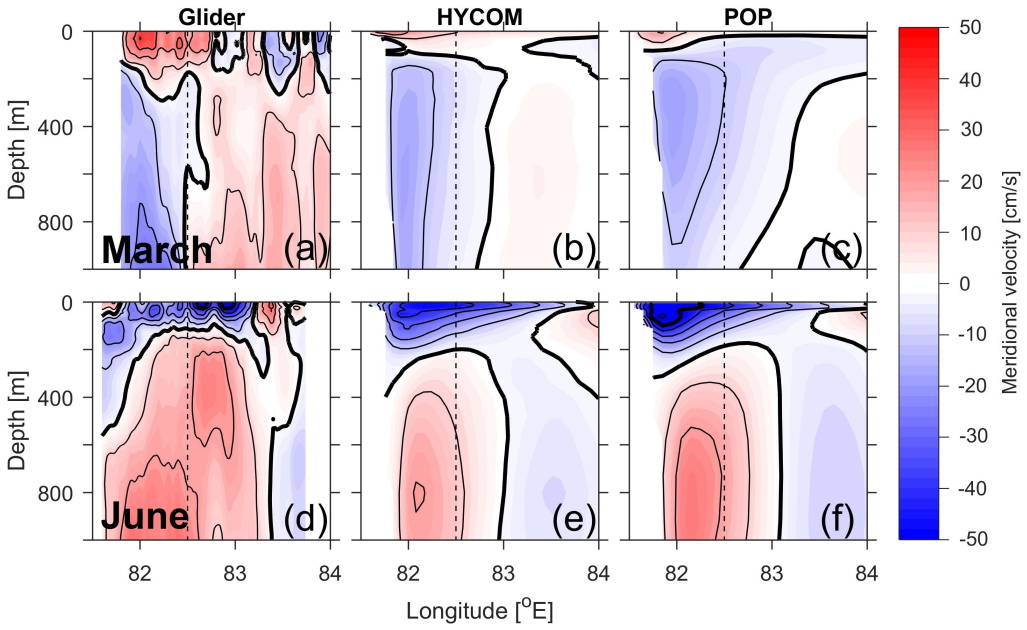

Figure 3.2: Geostrophic meridional velocity referenced to the depth-averaged velocity across 8° N from glider measurements during March 18-30, 2014 (a) and May 24 – Jun 8, 2014 (d), the mean absolute meridional velocity from HYCOM (b and e) and POP (c and f) in March and June over 2003-2012 and 1995-2007 periods, respectively. The black dashed line marks the typical eastern extent of the undercurrent core; the region bounded to its west is used for a subsequent averaging in Figure 3. Thin black lines are plotted every 10 cm s^{-1}, and thick black lines are plotted every 50 cm s^{-1}.

absolute geostrophic meridional velocity profiles.

Gliders were deployed to the east of Sri Lanka between 7° N and 9° N to collect salinity and temperature profiles from the surface to 1000 m depth during February 2014-January 2016 (Lee et al., 2016) (Figure 3.1a). The geostrophic velocities from the glider measurements are referenced in two ways. Glider temperature and salinity profiles are used to calculate geostrophic velocity across 8° N referenced to the glider depth-averaged velocity to examine the vertical structure of the undercurrent (e.g. Figure 3.2). Note that profiles sampled by the gliders were sporadic in time; the gliders took approximately 2-7 days to complete the transect and then could

take 5-30 days until the same transect was repeated. Thus, the glider velocity referenced to the depth-averaged current is less suitable to estimate the seasonal evolution of the circulation along Sri Lankan east coast (i.e. Figure 3.3). Instead, temperature and salinity profiles were used in the same way as the hydrography and Argo profiles to calculate bimonthly geostrophic meridional velocity.

Two global strongly eddy active OGCMs were used to study the vertical structure and seasonal variation of the boundary current, as well as its associated dynamics: 0.1° Parallel Ocean Program (POP) and 0.08° HYbrid Coordinate Ocean Model (HYCOM). Their horizontal resolutions correspond to 11 km and 9 km at 8° N, respectively. POP is a three-dimensional, z-level, primitive equation model (Smith et al., 2010). It was configured on a global tripole grid with 42 vertical levels and partial bottom cells. Its vertical grid spacing near the surface (top 50 m) is roughly 10 m. The POP simulation was initialized from year 30 of an earlier POP run that used the same set-up but was driven by a monthly climatology of Co-ordinated Ocean Reference Experiments (CORE) atmospheric surface fluxes (Maltrud et al., 2010). The subsequent POP simulation was forced by interannually-varying CORE-II fluxes for 1990-2007 (Delman et al., 2015). The POP output analyzed here consists of three-dimensional daily-averaged velocities and salinity for 1995-2007. HYCOM has a hybrid vertical coordinate with isopycnal coordinates in the open stratified ocean, a terrain-following coordinate for coastal regions, and a z-level coordinate in the mixed layer (Metzger et al., 2010). It was configured on a global tripole grid with 41 vertical layers. Vertical grid spacing very close to the surface is roughly 1 m increasing to 8 m over 36-85 m. The simulation was forced by 3-hourly Navy Operational Global Atmospheric Prediction System (NOGAPS) fields (Rosmond et al., 2002). However, the archived velocity fields used here are monthly and cover a shorter period compared to POP of 2003-2012.

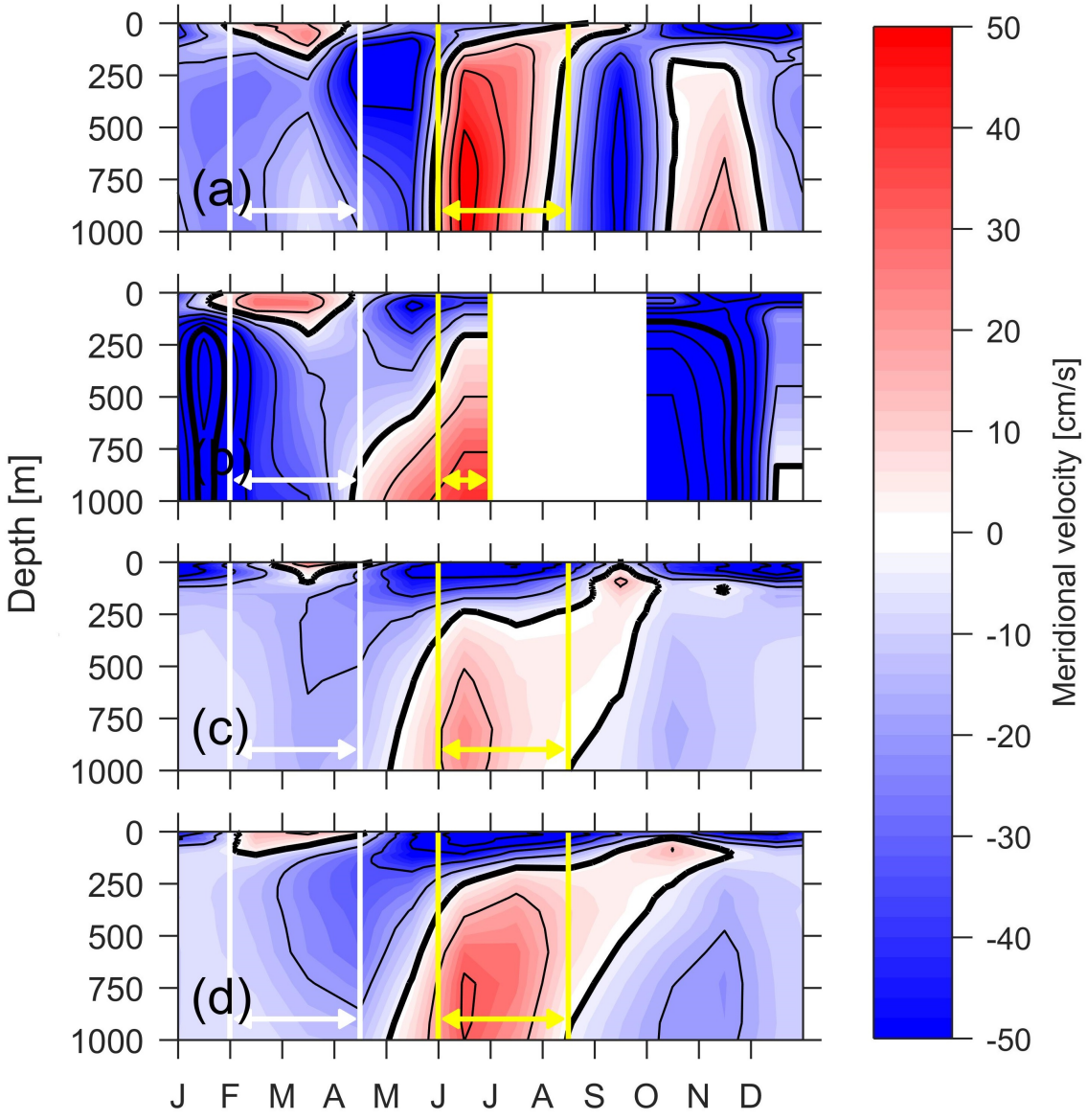

Figure 3.3: Bimonthly mean seasonal variation of the meridional geostrophic velocity referenced to the surface satellite ADT across the magenta transect in Figure 1 from hydrography and Argo measurements (a), glider measurements (b), monthly mean meridional velocity profiles from HYCOM (c), and POP (d) output. Line contours are plotted in the same manner as in Figure 2. White and yellow lines indicate periods when the undercurrent is most pronounced.

3.3 The Circulation east of Sri Lanka

3.3.1 Vertical structure

A zonal transect along 8° N is used to examine the circulation off the eastern coast of Sri Lanka. Both observations and OGCMs show a seasonally reversing surface current confined to the upper 100-200 m of the water column (Figures 3.2, 3.3). A subsurface current that flows in the opposite direction to that of the surface water, defined here as an undercurrent, is observed from glider measurements and the OGCMs particularly in March and June (Figure 3.2). As noted above, geostrophic velocities derived from glider measurements, during March 18-30, 2014 (Figure 3.2a) and May 28-June 8, 2014 (Figure 3.2d), are referenced to the depth-averaged velocity measured directly by the gliders. Velocity transects from HYCOM (Figure 3.2b, e) and POP (Figure 3.2c, f) were constructed from monthly averages of total velocity in March and June for the periods of 2003-2012 and 1995-2007, respectively.

The model transects show reasonable agreement with that from the gliders in regard to the vertical structure of both the surface current and undercurrent. In March, the core of the observed undercurrent is located about 55 km from the coast and has a maximum speed of 16-25 cm s^{-1} southward (Table 3.1). HYCOM and POP have maximum flows in the reverse direction to the surface i.e. southward, at 570 and 268 m, respectively (Figure 3.2a, b) while glider measurements show maximum subsurface flow at the deepest measured depth of 1000 m (Figure 3.2c). In June, a northward undercurrent is observed below approximately 250 m with a maximum speed greater than 20 cm s^{-1} at about 900 m (Figure 3.2d-f; Table 3.2). The summer undercurrent is approximately 165 km wide in the OGCMs. The velocity section derived from gliders shows a wider undercurrent of 210 km with two cores: a deep core that is approximately 100 km wide centered at 82.2° E and a shallow core at 400 m near 82.75° E (Figure 3.2d). This double-core feature is also evident in some individual model years, but is not present in the multi-year mean (Figure 3.2e, f).

Table 3.1: Statistics of the undercurrent across 8° N in March from the glider geostrophic velocity as presented in Figure 2 and mean absolute velocity from HYCOM and POP. Here, v_{max} represents maximum meridional velocity; depth of reversal is defined as the depth of the zero meridional velocity at the location of the maximum velocity; width of the undercurrent is defined as the distance from the coast at the depth of maximum velocity to the location where the meridional velocity is zero.

	v_{max} (cm s^{-1})	Depth of v_{max} (m)	Position of v_{max} (°E)	Depth of reversal (m)	Width (km)
Glider	-25.3	1000.0	82.06	232.0	107.8
HYCOM	-16.2	570.4	82.00	83.3	151.9
POP	-18.9	268.5	81.95	77.4	209.1

Table 3.2: Same as Table 1 but for June.

	v_{max} (cm s^{-1})	Depth of v_{max} (m)	Position of v_{max} (°E)	Depth of reversal (m)	Width (km)
Glider	29.6	1000.0	81.90-82.40	117.3-300	206.9
HYCOM	20.6	800.8	82.08	244.8	165.1
POP	27.6	918.4	82.15	244.1	172.8

Investigation of individual years of HYCOM and POP velocity fields reveals that although the location of the undercurrent core varies in depth and longitude, it is nearly always confined to the west of 82.5° E. Thus, this longitude limit will be used in subsequent averages over the undercurrent regime, and is indicated by the dashed line in Figure 3.2. The spring undercurrent exists in all years in the model simulations except for in 2007 and 2011 in HYCOM when an El Niño occurs in the preceding year. POP also shows a weakening of the spring undercurrent following an El Niño event, except in 1998 when the northward-flowing surface current is absent and the southward current extends from the surface to approximately 550 m depth.

3.3.2 Seasonal variation

Bimonthly mean meridional velocities computed from hydrography and Argo profiles and glider measurements are shown in Figure 3.3a and 3.3b respectively. These observed geostrophic

velocities are all referenced to surface velocity from the ADT. The model monthly mean total meridional velocities (Figure 3.3c, d) were constructed from the OGCMs by averaging the monthly mean velocity across 8° N along the transect from the eastern coast of Sri Lanka to 82.5° E (depicted by the magenta transect in Figure 3.1), which captures most of the undercurrent signal (Figure 3.1; Table 3.1, 3.2).

Surface circulation

Both surface and subsurface currents have strong seasonal variability (Figure 3.3). The surface current reverses its direction twice a year in agreement with previous studies (Yu et al., 1991; McCreary et al., 1996; Shetye et al., 1996; Vinayachandran and Yamagata, 1997; Vinayachandran et al., 1999; Eigenheer and Quadfasel, 2000; Durand et al., 2009; de Vos et al., 2014; Wijesekera et al., 2015; Lee et al., 2016). The mean meridional surface current is northward during boreal spring (Figure 3.2a-c, Figure 3.3) as the westward flowing North Equatorial Current often bifurcates at the east coast of Sri Lanka at approximately 7.5° N splitting into a northward and southwestward branch (Shetye et al., 1993; Hacker et al., 1998). The SLD emerges during the southwest monsoon. Its western branch is responsible for the observed southward flow along the eastern coast of Sri Lanka in that season (Figure 3.2d-f, Figure 3.3). During boreal fall, the surface current is northward. Similarly, northward surface flow was also observed in mooring measurements in the southern BoB in late July of 2015 at 85.5° E (Wijesekera et al., 2016b). During the winter, the southward-flowing EICC extends from the Indian east coast to the southern tip of Sri Lanka (Schott et al., 1994; Wijesekera et al, 2015) resulting in strong southward flow at 8° N (Figure 3.3).

Subsurface circulation

An undercurrent flowing in the opposing direction to the surface current is a prominent and consistent feature among the observations and OGCMs in boreal spring (beginning of February

to mid-April) and summer (beginning of June to mid-August) (Figure 3.3). In boreal spring, the southward-flowing undercurrent extends from approximately 200 to 900 m depth with a velocity maximum core in the range of 300-600 m depth. The velocities derived from hydrography and Argo profiles and glider measurements confirm the existence of the undercurrent below 150-250 m, although the magnitudes are not consistent (Figure 3.3). This may be due to interannual variation in intensity and position of the subsurface reversed flow, combined with the sporadic sampling of the hydrography and Argo data.

During the southwest monsoon, the northward-flowing undercurrent is apparent in both observations and the OGCMs (Figure 3.3). The undercurrent starts developing in May and reaches its maximum speed in June. The OGCMs also suggest an upward phase propagation during summer and early fall (May- October) with a speed of approximately 1.5 m day^{-1} in the upper 200 m of the water column (Figure 3.3c, d). This feature is also evident in the geostrophic velocity derived from hydrography-Argo profiles in the upper 100 m of the water column (Figure 3.3a).

To gain a better understanding of the subsurface circulation, we examine the POP velocity fields at 729 m , which encompasses the depth location of the undercurrent core in boreal spring and summer (Figures 3.2, 3.3; Tables 3.1, 3.2). In March, the undercurrent is strong and confined to 82.5° E along the entire Sri Lankan east coast . The undercurrent usually turns eastward around 6° N to combine with an eastward-flowing current along the Sri Lankan south coast, as shown in the simplified schematic derived from the POP 729 m velocity fields (Figure 3.4a). However, in some years (e.g. 1995, 1999, 2005, and 2007), the undercurrent turns westward around the southern coast of Sri Lanka and forms a narrow current, about 50-70 km wide, on the northern side of the eastward flow (Figure 3.4a). Note that a similar circulation is observed in the POP velocity fields at 318 m in March, albeit the flow is stronger. In boreal summer, there is a convergence of the eastward-flowing current along the south coast of Sri Lanka and a westward-flowing current in the southwestern BoB at approximately 7° N, 82.25° E , which is also shown in the simplified schematic (Figure 3.4b). Both OGCMs agree that the convergence

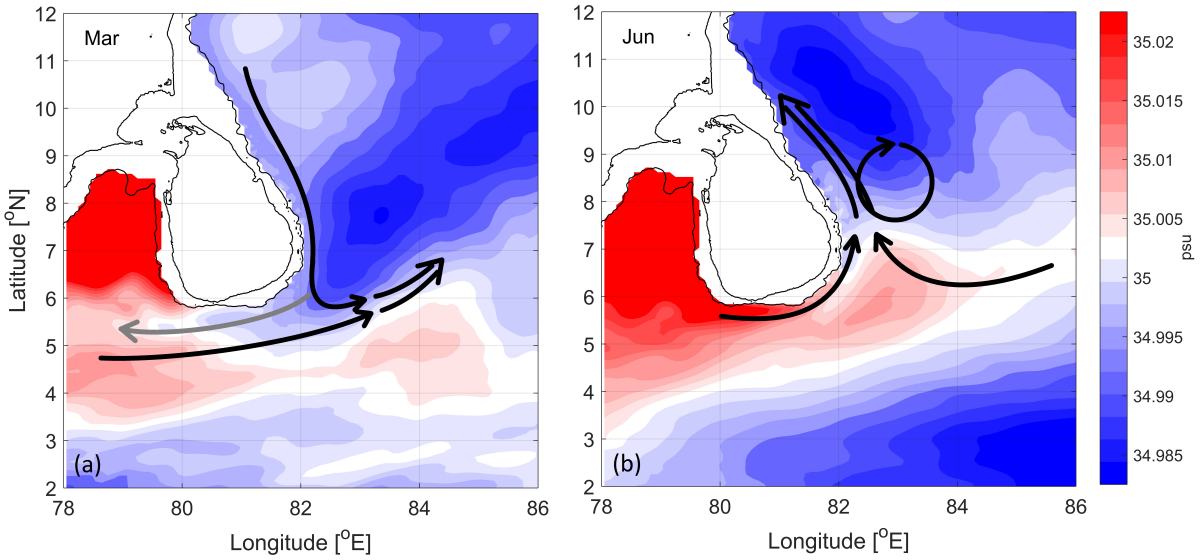

Figure 3.4: Simplified schematic of the undercurrent along the east and south coast of Sri Lanka at 729 m depth based on POP outputs in March (a) and June (b) plotted over the corresponding POP monthly mean salinity. The black arrows represent the annual current patterns at 729 m, and the gray arrow shows circulation that is observed occasionally. The 0 and 1000 m bathymetry contours are plotted as thin black lines.

produces the undercurrent flowing north along the east coast of Sri Lanka that injects relatively saline water into the BoB. In addition, an anticyclonic eddy often develops along the east coast, trapping local saline water inside, which is then propagated northward with the eddy .

During boreal fall (mid-August to end of October) and winter (beginning of November to end of January), flows in the subsurface layer are less consistent between the observations and the OGCMs (Figure 3.3). The models suggest that the subsurface current is not persistent across the years during fall and winter . Longitude-depth transects of meridional velocity across 8° N from POP and HYCOM (not shown) do not show a well-defined undercurrent near the east coast of Sri Lanka in the top 1000 m of the water column during these seasons.

3.3.3 Depth-integrated volume transport

Monthly volume transports computed from the OGCMs and volume transport computed from the discrete glider sections (referenced to depth-average velocity; e.g. Figure 3.2) across the

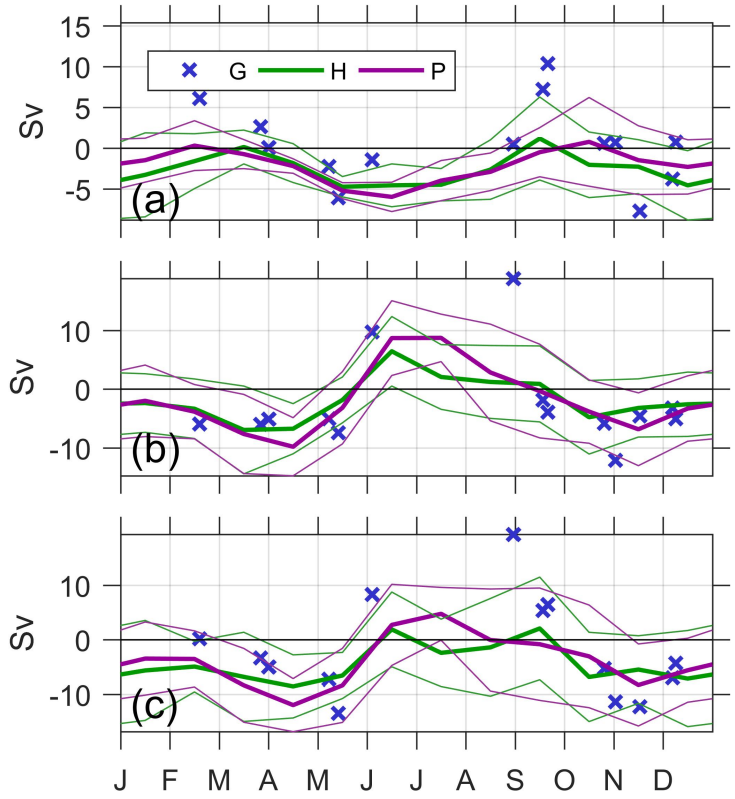

Figure 3.5: Meridional volume transport across 8° N from the Sri Lankan east coast to 82.5° E (dashed line in Figure 2) calculated from glider geostrophic velocity referenced to the depth-averaged velocity (G; blue cross) and absolute velocity fields from HYCOM (H; thick green line) and POP (P; thick purple line) over the 0-200 m (a), 200-1000 m (b), and 0-1000 m (c) layers. Thin lines designate the mean value ± one standard deviation.

8° N transect between the eastern coast of Sri Lanka and 82.5° E (Figure 3.1a) over the upper (0-200 m) and lower (200-1000 m) layers are presented in Figure 3.5. The seasonal variation from HYCOM, POP, and glider measurements agree well, especially in the subsurface layer. Mean volume transport in the upper layer (0-200 m) has a semi-annual cycle that ranges from 1 to 6 Sv into and out of the BoB (Figure 3.5a). Southward flows are observed in the surface layer during boreal summer and winter. The flows are weakly northward during boreal spring and fall.

Depth-integrated transport in the subsurface layer is southward throughout the year except during the summer when the northward-flowing undercurrent is present (Figures 3.3, 3.5b).

Table 3.3: Mean transport and seasonal salinity range of the undercurrent (200-1000 m) across 8° N in boreal spring (February to mid-April as highlighted by white lines in Figure 3) and summer (June to mid-August as highlighted by yellow lines in Figure 3) from hydrography-Argo profiles, glider measurements, HYCOM, and POP. Seasonal salinity range is the approximate difference between boreal spring and summer extremes in average seasonal cycle. Note that the statistics representing glider measurements are derived from gridded velocity referenced to its depth-averaged velocity (e.g. Figure 2) and salinity interpolated onto 8° N.

	Mean transport (Sv)		Seasonal salinity range
	Spring	Summer	
Hydrography-Argo	-6.9	9.7	0.09
Glider	-5.7	11.42	0.04
HYCOM	-4.6	3.0	0.01
POP	-5.7	6.8	0.01

The undercurrent transport is approximately 5-7 Sv out of and 3-11 Sv into the BoB during boreal spring and summer, respectively (Table 3.3). Moreover, the OGCMs suggest only a small mean volume transport of the subsurface current during fall and winter compared to its standard deviation (Figure 3.5b) implying that the fall and winter undercurrent is not well defined in these seasons and indeed can flow northward in some years. Volume transport over the 0-1000 m layer ranges from -12 to 5 Sv and exhibits an annual cycle similar to that in the lower (200-1000 m) layer (Figure 3.5c).

3.4 Discussion

The circulation in the southern BoB is complex as it is controlled by various forcings, such as local winds, Ekman pumping, and equatorial waves, which impact the region in different seasons. The mechanisms driving the undercurrent remain unclear and although beyond the scope of this study we put forward some informed hypotheses based on previous studies and our observations. The Rossby waves, equatorial waves, and Ekman pumping are likely to be important for producing the undercurrent: a Hovmöller diagram of POP meridional velocity across 8° N (Figure 3.6) shows the westward propagation of the velocity signal at 729 m depth

originating from the eastern boundary of the BoB that takes about four months to cross the southern BoB. It has a propagation speed of 12 cm s^{-1} in good agreement with the phase speed of a mode 2 baroclinic Rossby wave in this region (Shankar et al., 1996; Killworth and Blundell, 2003; Wijesekera et al., 2016a). A westward-propagating signal first develops at the eastern boundary of the BoB in April-May at the same time that the Wyrtki Jet, a surface-intensified eastward-flowing current observed in the equatorial Indian Ocean during the monsoon transitions (Wyrtki, 1973), reaches this eastern boundary. The westward-propagating signal reaches the east coast of Sri Lanka in September contributing to the southward-flowing subsurface current (Figures 3.3); this is consistent with findings from the LSM study (McCreary et al., 1996). In April, the westward propagating meridional flows originating at 83° E-85° E (Figure 3.6b) are associated with the subsurface anticyclonic eddy observed along the east coast of Sri Lanka during the summer (Figure 3.4b). The influence of equatorial waves on the undercurrent is still unclear and more studies are needed. Upward phase propagation is present during summer and early fall (Figure 3.3) implying the influence of equatorial waves on the subsurface flow during this time (Luyten and Roemmick, 1982). Equatorial waves are also known to impact currents along the Indian east coast (Mukherjee et al., 2014) and Sri Lankan south coast (Schott et al., 1994; Shankar et al., 2002).

Ekman pumping can also significantly impact the circulation along the eastern coast of Sri Lanka (McCreary et al., 1996; Vinayachandran et al., 1999). The LSM study of McCreary et al. (1996) suggested that Ekman pumping drives the undercurrent east of Sri Lanka from April to December. The model undercurrent has a core at 400-500 m that can reach a maximum speed of 10 cm s^{-1} southward and northward in March-April and August, respectively. Although this value agrees quite well with that of the spring undercurrent observed in the observations and OGCMs, the magnitude given by the LSM during the summer is about half that shown in this study (Figure 3.3). During the winter, the mean subsurface current of the observations and OGCMS agrees with the results from the LSM (McCreary et al., 1996) within one standard deviation. This implies that

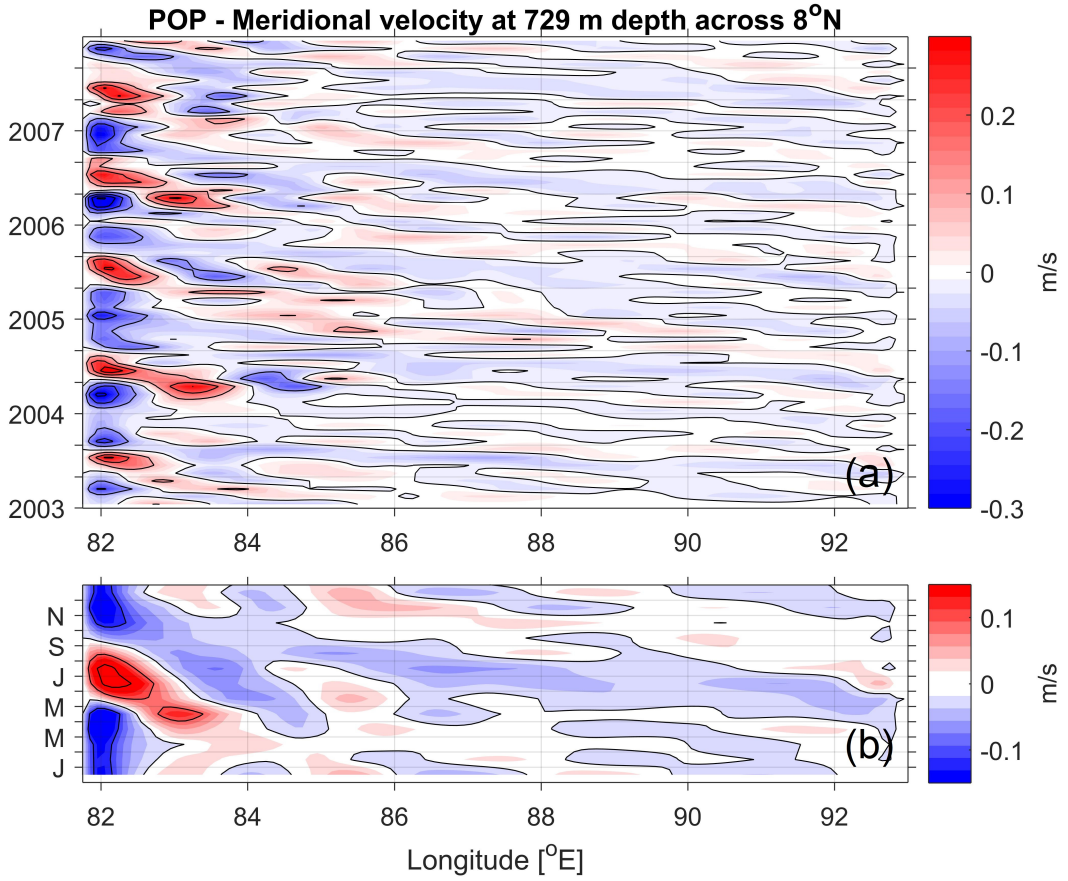

Figure 3.6: Time-longitude plots of monthly meridional velocity (a) and seasonal mean velocity (b) over 2003-2007 across 8° N at 729 m from POP. Note the difference in color scale.

a combination of local alongshore winds, Ekman pumping, and equatorial waves, which are the main mechanisms driving the subsurface current during the winter in the LSM, is important in producing the subsurface current in only some years.

Circulation in the subsurface layer along the Sri Lankan east coast is characterized by reversed flows relative to the surface during boreal spring and summer similar to the subsurface circulation along the Indian east coast and Sri Lankan south coast described by previous studies (Schott et al., 1994; McCreary et al., 1996; Mukherjee et al., 2014). During the southwest monsoon, the current along the Sri Lankan south coast (Schott et al., 1994), Sri Lankan east coast (Figure 3.2d-f; Table 3.2), and Indian east coast (Mukherjee et al., 2014) reverses its direction below approximately 100-150 m. The subsurface current flows eastward along the southern coast of Sri Lanka (Schott et al., 1994) in agreement with the circulation pattern derived from the POP velocity fields (Figure 3.4b) and poleward along the Sri Lankan and the Indian east coast (McCreary et al., 1996; Mukherjee et al., 2014). This suggests the possibility of a subsurface conduit connecting the region off the Sri Lankan south coast to the northern BoB. However, the subsurface poleward current along the Indian east coast is not always apparent (Mukherjee et al., 2014), although it is also possible that the undercurrent during this season occurs below the deepest measurement at 300 m from the Mukherjee et al. (2014) study. In boreal spring, mooring measurements along the Sri Lankan south coast (Schott et al., 1994) verifies the existence of the eastward-flowing subsurface current observed in the POP velocity fields (Figure 3.4a). The subsurface current extends from approximately 250 m to 1010 m (Schott et al., 1994). Unlike the summer subsurface circulation, flow at and north of 12° N is poleward over 0-300 m (Mukherjee et al., 2014), in the opposite direction to the undercurrent off the Sri Lankan east coast (Figures 3.2a-c, 3.3). However, since the core location of the spring undercurrent is highly variable from year to year, direct velocity measurements in the deeper layer would help to gain a better understanding of the pathways of the subsurface circulation along the western boundary of the BoB during boreal spring.

Although velocity and salinity fields from POP suggest the possibility of significant salt exchange between the AS and the BoB, the estimated salt transport via the undercurrent is small based on the data and models we have available. POP velocity fields show that the summer undercurrent injects relatively saline water into the western boundary of the BoB that can be trapped in a northward-propagating seasonal anticyclonic eddy (Figure 3.4b). The source of the saline water is mostly from the southwest of Sri Lanka, although sometimes, such as in 1998, it originates from the eastern BoB . Relatively fresher water is transported southward along the east coast of Sri Lanka in the subsurface layer in spring (Figures 3.4a, 3.7). It can be advected westward along the Sri Lankan south coast in some years depending on the strength and location of the deep eastward-flowing Wyrtki jet (Reppin et al., 1999). The time series of salinity averaged over the width of the undercurrent (from the east coast of Sri Lanka to 82.5° E) and the volume transport of the POP undercurrent (over 200-1000 m) along 8° N clearly show a positive correlation i.e. the undercurrent tends to export freshwater from the BoB and import saline water into the BoB (Figure 3.7). The hydrography-Argo profiles, glider measurements, and HYCOM also show that poleward subsurface transport is associated with relatively saline water and vice versa (not shown). The correlation coefficient between the subsurface transport and salinity computed from POP is 0.50, significant at the 95% confidence level. The salt flux due to the fluctuations of the flow and of the salinity (departures from the 13-year climatology) in the 200-1000 m layer from POP is 0.04 $\times$ 10^6 kg s^{-1} (Figure 3.7), while the estimated salt flux from the hydrography-Argo profiles and glider measurements are 0.19×10^6 and 0.09×10^6 kg s^{-1}, respectively. The difference between the observational and POP salt fluxes arises from the smaller salinity range of the model compared to the observations (Table 3.3). The estimated salt input is up to 4% of the total expected salt transport into the BoB of $4.5\text{-}4.9\times10^6$ kg s^{-1}, which is estimated from the annual freshwater input of 0.13-0.14 Sv (Rao and Sivakumar, 2003; Sengupta et al., 2006; Wilson and Riser, 2016). Note that the total net salt transported by POP into the BoB across 8° N is 4.3×10^6 kg s^{-1}; this value is in good agreement with the expected salt transport

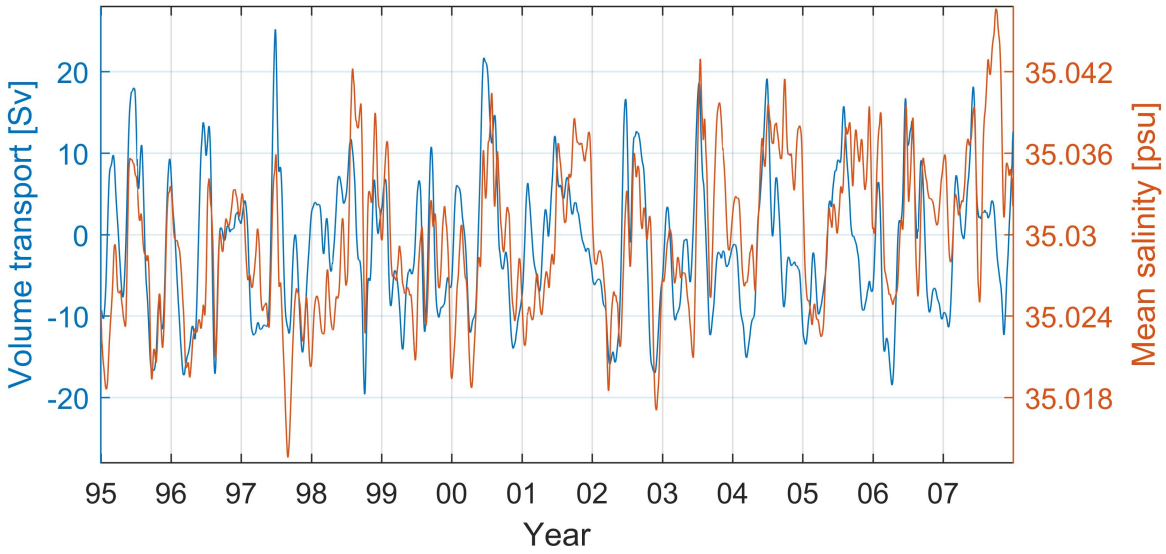

Figure 3.7: Time series of volume transport (blue) and mean salinity (orange) between 81.5° E and 82.5° E over the 200-1000 m layer from POP.

discussed above. Estimates of salt flux by the mean flow over the same depth layer from POP and HYCOM are even smaller: the mean undercurrent transport of 1.5-2 Sv in the OGCMs is fresher than the interior northward flow as judged from HYCOM and sparse hydrography and Argo profiles (not shown), but the salinity contrast at this depth layer is smaller than 0.01. In addition, the small salt transport from the mean flow in the 200-1000 m layer might be due to the core of the undercurrent moving vertically such that this layer may sometimes include opposite flows or smaller salinity contrasts with the interior (Figures 3.2, 3.3; Table 3.1, 3.2).

An alternative interbasin-exchange pathway is through the interior of the BoB, particularly during the southwest and northeast monsoon (Vinayachandran et al., 1999; Wijesekera et al.,

2015; Wijesekera et al., 2016b). Observations indicate that the eastward-flowing southwest monsoon current (SMC) has a role in the injection of saline water originating in the AS into the southern central BoB during early summer. As the summer progresses, the seasonal cyclonic (i.e. the SLD) and anticyclonic eddies influence the pathway of the SMC (Vinayachandran and Yamagata, 1997; Vinayachandran et al., 1999). Mooring observations at 85.5° E from 5° N to 8° N reveal a northward-flowing subsurface SMC that is associated with high salinity water (Wijesekera et al., 2016a; Wijesekera et al., 2016b). During the northwest monsoon, mass and salt exchange between the AS and the BoB is also observed in the interior over the 50-75 m layer in the southern BoB, approximately between 82°5̇ E and 85° E (Wijesekera et al., 2015).

3.5 Summary

The velocity fields derived from hydrography and Argo profiles, glider measurements, POP, and HYCOM reveal the presence of an undercurrent off the east coast of Sri Lanka during boreal spring and summer, which has opposite direction to the seasonally reversing surface flow. The location and width of the core of the undercurrent change seasonally. The undercurrent shows the greatest interannual variability during spring, which is likely due to the influence of El Niño events. The observations and OGCMs suggest that the undercurrent over the 200-1000 m layer transports more water than the surface current over the 0-200 m layer. The mechanisms driving the undercurrent are still unclear, though Ekman pumping is likely to affect the undercurrent especially during the boreal spring (McCreary et al., 1996; Vinayachandran et al., 1999). Upward phase propagation is distinct during the summer suggesting the influence of equatorial forcing on the circulation across 8° N. Our analyses do not observe the direct influence of Rossby waves on the modification of the spring and summer undercurrent. Although the POP velocity fields suggest a potential pathway in salt exchange between the AS and the BoB, salt transport across 8° N by the undercurrent estimated from POP and the observations is expected to be less than 4%

of the total salt input into the BoB required to balance the freshwater sources. More studies are needed to determine the mechanisms driving the undercurrent and its role in interbasin salt and mass exchange. In turn, this knowledge will lead to a better understanding of property exchanges in the northern Indian Ocean.

3.6 Acknowledgement

This work is supported by the US Office of Naval Research (ONR) as part of two ONR Departmental Research Initiatives: Air-Sea Interactions Regional Initiative (ASIRI) and Northern Arabian Sea Circulation - autonomous research (NASCar) projects through ONR grants N00014-14-1-0629 (A. Anutaliya and U. Send), N00014-15-1-2189 (J. L. McClean), N00014-16-1-2313 (J. Sprintall), N00014-13-1-0478, N00014-15-1-2296, N00014-15-1-2231 (L. Rainville and C. Lee). J. Metzger and A. Wallcraft are supported by the "Eddy resolving global ocean prediction including tides" project under ONR program element 0602435N. Hydrographic profiles are from the National Center of Environmental Information (Boyer et al., 2013) (https://www.nodc.noaa.gov/access/index.html). Argo data were collected and made freely available by the International Argo Program and the national programs that contribute to it (http://www.argo.ucsd.edu, http://argo.jcommops.org). The Argo Program is part of the Global Ocean Observing System. The altimeter products were produced by Ssalto/Duacs and distributed Aviso, with support from Cnes (http://www.aviso.altimetry.fr/duacs/). The HYCOM simulation was performed using grants of computer time from the Department of Defense High Performance Computing Modernization Program. This is NRL contribution NRL/JA/7320-17-3395, which is approved for public release and distribution is unlimited. The POP simulation was carried out using the Extreme Science and Engineering Discovery Environment (XSEDE), which is supported by National Science Foundation grant number ACI-1548562. POP output is available from XSEDE. Thanks to He Wang (SIO) for helpful discussions about the salt transport calculation.

Also, thanks to Judy Gaukel (SIO) for extracting and transferring the OGCM files.

Chapter 3, in full, is a reprint of the material as it appears in Ocean Science, “An undercurrent off the east coast of Sri Lanka”, by A. Anutaliya, U. Send, J. L. McClean, J. Sprintall, L. Rainville, C. M. Lee, S. U. P. Priyantha, A. J. Wallcraft, and E. J. Metzger (2017). The dissertation author was the primary investigator and author of this paper.

Chapter 4

Mooring and seafloor pressure end-point measurements at the southern entrance of the Solomon Sea: subseasonal to interannual flow variability

Abstract

Variability of the flow across the Solomon Sea's southern entrance was examined using end-point subsurface moorings and seafloor pressure sensors, reconstructed velocity profiles based on satellite-derived surface velocity and bottom pressure-derived subsurface velocity, and 1993-2017 proxy volume transport based on satellite altimetry. The reconstructed velocity correctly represents the fluctuating surface flow and subsurface core providing a high-frequency continuous observing system for this sea. The mean equatorward volume transport over 0-500 m depth layer is 15.2 Sv (1 Sv $\equiv 10^6$ m^3/s) during July 2012 – May 2017. The measurements resolve the full spectrum of the volume transport including energetic subseasonal variability that

fluctuates by as much as 25 Sv over one week. At low-frequency timescales, the study finds that linear Rossby waves forced by Ekman pumping in the interior of the Pacific not only influence seasonal fluctuations as found by previous studies, but also interannual variability. As found previously, the El Niño Southern Oscillation highly influences interannual volume transport. During the 2015/2016 El Niño, observations show the seasonal cycle to be suppressed from the second half of 2014, prior to the mature phase of the El Niño, to September 2016 along with an increase in across-transect transport. At subseasonal timescales, local Ekman pumping and remote wind stress curl are responsible for a third of the subseasonal variance. The study highlights the importance of high-frequency observations at the southern entrance of the Solomon Sea and the ability of a linear Rossby model to represent the low-frequency variability of the transport.

4.1 Introduction

The surface New Guinea Coastal Current (NGCC) and the subsurface New Guinea Coastal Undercurrent (NGCU) serve as the Low Latitude Western Boundary Current (LLWBC) of the subtropical cell in the Pacific Ocean (McCreary & Lu, 1994). This LLWBC system is a major conduit of flow between the South Pacific Ocean and the equatorial Pacific as it replenishes the equatorial Warm Pool and supplies the Equatorial Undercurrent (EUC) (Tsuchiya et al., 1989; Grenier et al., 2011) and the Indonesian Throughflow (Fine et al., 1994; Waworuntu et al., 2000). Since the equatorial Pacific impacts large-scale atmospheric convection and climate modes (Picaut et al., 1996; Gu & Philander, 1997; McPhaden & Zhang, 2002), such as El Niño Southern Oscillation (ENSO) (Melet et al., 2010b; Davis et al., 2012; Zilberman et al., 2013; Ganachaud et al., 2014), variability of the NGCC/ NGCU current system potentially influences climate variability.

In the past, historical shipboard Acoustic Doppler Current Profiler (SADCP) data, Spray

gliders, and Argo floats have been used to quantify the mean and variability of the NGCC/ NGCU current system. The time-series mean of the volume transport into the Solomon Sea (hereafter referred to as the inflow) at its southern entrance has been found to be 15 Sv over 0-300 m, 15 Sv over 0-700 m, and 19 Sv over the 0-1000 m layer, respectively (Cravatte et al., 2011; Davis et al., 2012; Zilberman et al., 2013). Seasonal variations as high as 30 Sv are captured by glider measurements at the southern entrance (Davis et al., 2012); the volume transport reaches its minimum in February and maximum in July - August (Kessler et al., 2019). Interannual variability of the circulation in the Solomon Sea is strongly influenced by ENSO signals (Melet et al., 2010b; Melet et al., 2013). Strengthening (weakening) of the equatorward flow through the Solomon Sea occurs during El Niño (La Niña) events (Davis et al., 2012; Zilberman et al., 2013). None of these measurement systems are able to resolve the variability on shorter timescales (i.e. the subseasonal variability that is < 60 days).

In this study, we address the variability of the volume inflow at the southern entrance of the Solomon Sea at subseasonal, seasonal, and interannual timescales using high-frequency end-point measurements from dynamic height moorings and seafloor pressure sensors (PIES: Pressure with Inverted Echo Sounders; Kennelly et al., 2007). The measurements are available hourly and resolve signals with periods as short as 3 days, hence the time series are not subject to aliasing such as that which might result from less frequent sampling in the presence of high eddy activity in this region (Melet et al., 2010b; Hristova & Kessler 2012; Gourdeau et al., 2014). Moreover, these continuous observations allow for the development of a volume transport proxy using satellite altimeter data over the observational period, and thus allows extension of the time series to the 1993 - 2017 period. The 25-year proxy timeseries provides us with a valuable dataset to examine the interannual variability of the Solomon Sea inflow.

To understand the governing mechanisms associated with the variability of the circulation in the Solomon Sea, numerical ocean model simulations have shown that the regional circulation is influenced by the annual march of the trade winds and the Asian monsoon winds (Kessler &

Gourdeau, 2007; Hristova & Kessler, 2012). Further, the seasonality of the trade winds produces Rossby waves that affect the South Equatorial Current (SEC) approximately from 2° to 10° S (Chen & Qiu, 2004; Melet et al., 2010a). The arrival of downwelling (upwelling) Rossby waves at the Solomon Strait excited by the annual winds from the Central Pacific in March-April (September-October) produces southeastward (northwestward) surface flow at the southern entrance of the Solomon Sea (Melet et al., 2010b; Gourdeau et al., 2014). In the southwestern Pacific (from approximately 10° S to 30° S), wind stress curl dominates the annual variability of the thermocline depth (Wang et al., 2000; Chen & Qiu 2004; Kessler & Gourdeau 2007) and potentially influences the Solomon Sea inflow. Observations of sea surface height from satellite altimetry (Chen & Qiu 2004; Melet et al., 2010b), thermocline depth (Wang et al., 2000), and surface velocity from satellite-tracked drifters (Hristova & Kessler, 2012) demonstrate the influence of Rossby waves and wind stress curl in the western subtropical Pacific on the annual variability of the flow. However, to date, no high-frequency in-situ measurements have been available to demonstrate the influence of local and remote forcing on the regional circulation, particularly at the subseasonal timescale. Therefore, using our observations, we also aim to examine the role of Rossby waves, the subtropical wind stress curl, and local winds on the variability of the Solomon Sea inflow at subseasonal, seasonal, and interannual timescales.

The paper is organized as follows. The data sets and methodology are described in section 2 and 3, respectively. Section 4 presents the estimated mean and variability at subseasonal, seasonal, and interannual timescales of the current system derived from the end-point measurements. Section 5 describes the impact of Rossby waves and local and remote winds on the variability of the inflow into the Solomon Sea. Discussion of the results and a summary are found in Sections 6 and 7, respectively.

4.2 Data sets

4.2.1 In-situ measurements

A subsurface mooring and a PIES were deployed on either side of the southern Solomon Sea, spanning a section sufficiently far from the equator to compute geostrophic currents across the section. One site is near Gizo, Solomon Islands (8.2° S, 157.0° E), and the other near Misima island, Papua New Guinea (10.6° S, 152.8° E). Figure 4.1 shows a map of the study area, and table 4.1 contains the deployment particulars. The subsurface moorings collected data during multiple deployments from mid-2012 through mid-2017, and were discontinued afterward. Each mooring contained six instruments for temperature and salinity distributed over the upper 500 m of the water column (Table 4.1). The intent of these measurements is to provide vertical profiles of density, and thereby the vertical shear of the geostrophic flow by differencing dynamic height (or geopotential anomaly) profiles measured at the two measuring sites. The actual instrumental sensors are for temperature and conductivity, and a subset of the instruments had pressure sensors. Pressure values for the remaining instruments were determined by interpolation along the (known) mooring wire lengths. Before each deployment and after each recovery, a calibration/validation effort was carried out that compared mooring sensors either against ship-based CTD casts (following Kanzow et al., 2006), or against a reference instrument submerged locally at a pier. Salinity water samples from bottles were used as well. Sensor drift was removed assuming linear drifts over time. In the adjusted data, salinity accuracy is estimated conservatively at $\sim$0.01-0.02, with the largest errors in the upper instruments due to bio-fouling of the conductivity sensor.

PIES were deployed on the seafloor at approximately 300 m depth, which is the depth of the subsurface velocity core at the Solomon Sea southern entrance (Davis et al., 2012). The PIES were deployed in early 2012 at both sites, and after multiple re-deployments, the measurements are still continuing to date (March 2019). Table 4.1 lists the deployment details. PIES measure

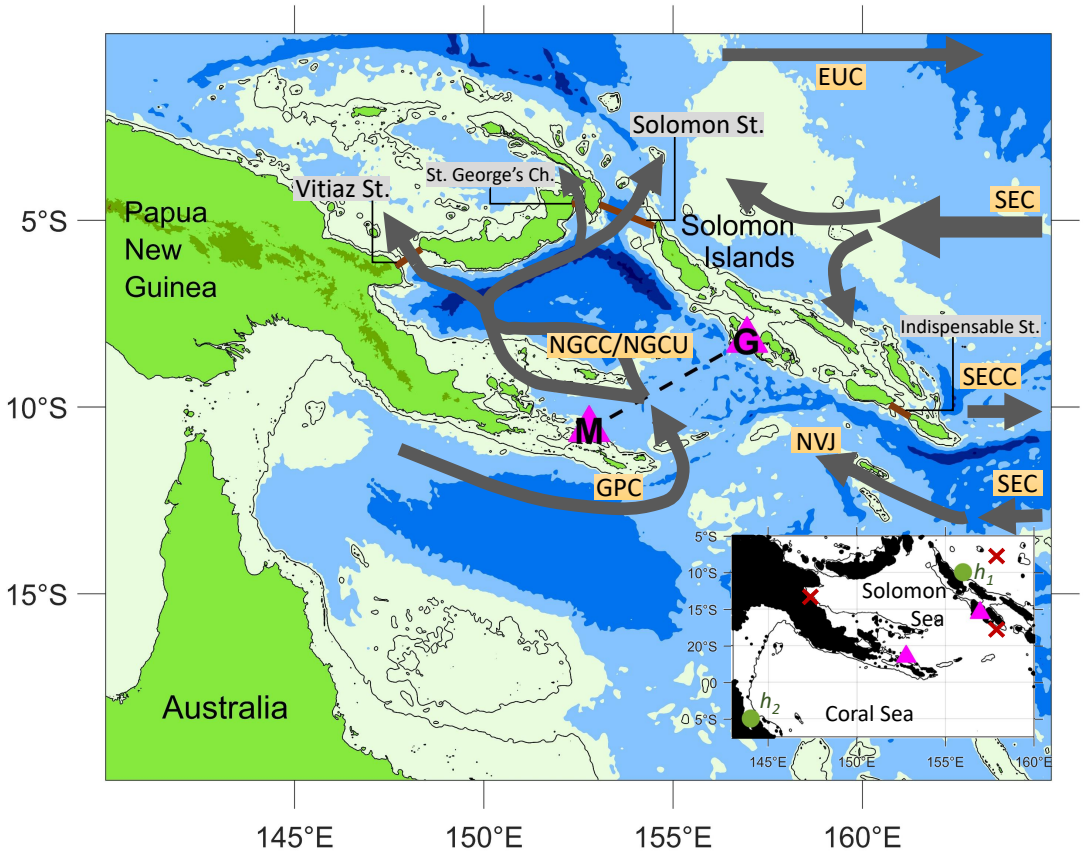

Figure 4.1: Bathymetry of the Solomon Sea and its surroundings along with the location of the moorings and PIES (magenta triangles) near Misima (M) and Gizo (G) Islands. Schematic of dominant Solomon Sea currents are represented by the gray arrows; NGCC is New Guinea Coastal Current, NGCU is New Guinea Coastal Undercurrent, GPC is Gulf of Papua Current, NVJ is North Vanuatu Jet, EUC is Equatorial Undercurrent, SEC is South Equatorial Current, SECC is South Equatorial Countercurrent. Black contours are plotted for 0 and 1000 m depth. The inset shows locations used to construct the proxy volume transport (maroon crosses) and Δh (green circles).

Table 4.1: Deployment times, locations, and instrument depths of the moorings and PIES at Misima and Gizo. The six instruments of every mooring deployment each had sensors for conductivity and temperature, and at least three of each mooring (marked with asterisks) also had pressure. PIES instruments have sensors for seafloor pressure and water-column acoustic travel time.

	Misima			**Gizo**		
Deployment	Time	Location	Instrument Depth [m]	Time	Location	Instrument Depth [m]
Mooring 1	07/2012 - 08/2015	10°34.51' S 152°41.53' E	64*, 112, 162, 261*, 361, 507*	07/2012 - 03/2015	08°14.04' S 156°56.34' E	60*, 109, 158, 257*, 357, 504*
Mooring 2	08/2015 - 05/2017	10°34.52' S 152°41.40' E	62*, 112, 162, 262*, 362, 508*	03/2015 - 07/2016	08°14.12' S 156°56.30' E	63*, 110, 159, 258*, 359, 508*
Mooring 3	-	-	-	07/2016 - 11/2017	08°14.21' S 156°56.28' E	89*, 138, 188, 287*, 386, 534*
PIES 1	02/2012 - 09/2014	10°36.12' S 152°47.10'E	311	02/2012 - 07/2016	08°12.90' S 156°57.45' E	320
PIES 2	09/2014 - 09/2018	10°36.11' S 152°47.15'E	285	07/2016 - ongoing	08°12.89' S 156°57.42' E	326
PIES 3	09/2018 - ongoing	10°36.13' S 152°47.14'E	285	-	-	-

seafloor pressure and water-column acoustic travel time. Here, only the pressure data are used, which are particularly accurate from this instrument. The acoustic travel time data are available in principle, but their usefulness is limited by the shallow instrument deployment depth and they are redundant with the much more accurate water column information from the temperature and salinity data used here. The data processing procedure for the removal of the mean value, trend, and tides in the pressure signal follows that described by Kennelly et al. (2007). Ultimately, the data product is a time series of pressure anomalies, from which geostrophic velocity fluctuations at the depth of the PIES can be calculated. This is akin to a geostrophic reference "level of known motion". However, because the mean and low-frequency variability are removed as a consequence of data processing (section 3.2), only velocity fluctuations on timescales faster than

each individual deployment duration (2-4 years) are captured in these data.

Spray gliders have been operated in the Solomon Sea since mid-2007; they measure temperature, salinity, and depth-average current across the southern entrance of the Solomon Sea in the upper 1000 m of the water column (Davis et al., 2012; Kessler et al., 2019). The gliders typically take about one month to cross the southern entrance, making 100-150 profiles during each transect crossing. They crossed the entrance every month prior to 2013 and roughly every 3 weeks afterward. The glider measurements were used to correct the satellite-derived surface velocity. Also, the measurements provide an independent estimate of the volume transport at the Solomon Sea southern entrance. Temperature and salinity profiles from Argo floats were utilized to extrapolate the density profiles between the surface and the shallowest mooring measurement (typically 60-90 m; Table 4.1). There were 68 and 123 Argo floats within 1° of the mooring at Gizo and Misima, respectively. Vertical resolution of the temperature, salinity, and pressure sampled by the Argo floats was 10 m near the surface and 50 m at 500 m. Argo floats were also used to determine an error associated with the mooring-derived sheared flow due to vertical density interpolation.

4.2.2 Remotely-sensed data

The all-sat-merged absolute dynamic topography (ADT) gridded products, deduced from the mean dynamic topography and the gridded satellite sea level anomaly (SLA), are available on a $\frac{1}{4}°$ grid at daily resolution and cover the period of 1993-2017. The data were linearly interpolated in space to the Gizo and Misima sites. The ADT products at the two observing sites were used to calculate the surface geostrophic velocity, and the SLA products were used to construct a proxy for the volume transport. Surface wind data were used to better understand the impact of local Ekman pumping and remote winds on the inflow variability and also to examine the impact of Ekman transport on the across-transect volume transport. The Version 2 Cross-Calibrated Multi-Platform (CCMP) from Remote Sensing Systems provided gridded surface vector winds

on a $\frac{1}{4}^\circ$ grid with a temporal resolution of 6 hours (Wentz et al., 2015). The CCMP winds were available from July 1987 to December 2017.

4.3 Methodology

4.3.1 Sheared velocity

Density was calculated from the measured temperature and salinity at 6 depths over the water column (Table 4.1), then interpolated onto a 1-m vertical grid. Cubic interpolation was performed below the depth of the shallowest mooring sensor, while the missing surface portion was derived from the mean density profile measured by nearby Argo floats. Mean sheared velocity across the transect between the mooring sites ($v_{sheared}(p,t)$) was calculated from the difference of the dynamic height profiles measured between Misima (M) and Gizo (G), similar to the method described by Kanzow et al. (2006):

$$v_{sheared}(p,t) = \frac{1}{f\Delta x}\int_{p_{ref}}^{p}\left(\delta(p,t)^G - \delta(p,t)^M\right)\mathrm{d}p, \tag{4.1}$$

where f is the Coriolis parameter at the mean latitude (9.4° S), Δx is distance between the two measurement sites (∼532 km), p_{ref} is pressure at the reference level of 500 dbar, δ is specific volume anomaly defined as,

$$\delta(p,t) = \frac{1}{\rho(p,t)} - \frac{1}{\rho_{(35,0)}(p)}, \tag{4.2}$$

$\rho_{(35,0)}(p)$ is density of seawater with salinity of 35 and temperature of 0° C. To estimate the uncertainty associated with interpolating density profiles from the mooring measurements, "mooring-like" density profiles were estimated from subsampling 68 and 123 Argo density profiles measured near Gizo and Misima at the mean depth of the six mooring sensors (Table 4.1). The Argo float

density profiles were treated as the true density profiles and subsampled like a mooring to obtain an uncertainty of 2.7 Sv in the sheared volume transport. The estimated uncertainty is associated with density interpolation between mooring sensors and extrapolation of the density profiles toward the surface. The surface geostrophic velocity relative to 500 m derived from the mooring density profiles, glider data, and Argo float data have a similar mean value; the root-mean-square (rms) difference is smaller than 4.5 cm s^{-1}. Vertically integrated sheared flow across the transect calculated from the three data sets also agree well; the mean values agree within 2 Sv. This suggests that the uncertainty associated with mooring density interpolation and extrapolation in the sheared transport estimate is small. With the instrumental errors, the total rms uncertainty in the sheared transport across the transect is estimated to be 3.1 Sv.

4.3.2 Velocity fluctuation at PIES depth

Velocity fluctuations at the mean depth of the PIES during each deployment ($\sim$300 m) were calculated from the PIES bottom pressure measurements and were combined with $v_{sheared}$ in order to obtain the total geostrophic volume transport variability. The PIES bottom pressure measurements were averaged over one-hour bins. Then the seven most dominant tidal constituents were removed using UTide (Codiga, 2011). In addition, an exponential-linear trend associated with pressure drift (Kennelly et al., 2007) was removed. At these measurement sites, the dynamic range of the pressure fluctuation is 0.2 dbar and the sensor drift over a 4-year deployment ranges from less than 0.1 to 0.6 dbar. To remove tidal signals that might remain in the detrended records, the tidal constituents that were previously removed were added back to the detrended pressure fluctuation, after which the seven major tidal constituents were again removed. Finally, a 3-day lowpass Butterworth filter (the inertial period at this latitude) was applied to the pressure fluctuations. Velocity fluctuations at the depth of the PIES (v'_{sub}) were estimated from the pressure

fluctuations (p'_{sub}) (Kanzow et al., 2006):

$$v'_{sub}(t) = \frac{1}{f\Delta x}\left(\frac{p'^{G}_{sub}(t)}{\rho^{G}} - \frac{p'^{M}_{sub}(t)}{\rho^{M}}\right). \tag{4.3}$$

The barotropic volume transport fluctuations are then calculated assuming a slab flow which is a product of v'_{sub}, Δx and the 500 m layer. The rms error associated with the slab flow including uncertainty from the detrending and instrument error is 4.8 Sv.

4.3.3 Absolute geostrophic velocity

To produce the absolute geostrophic velocity, $v_{sheared}$ is referenced to the depth of the PIES at ~300 m. Then, the same fluctuation for the entire water column (v'_{sub}) is added to the sheared profiles. However, the resulting transport still needs a constant offset to adjust for the unknown vertical placement of each PIES with respect to the geoid. The offset is found from an alternative estimate of the volume transport, calculated from the mooring measurements and ADT where the ADT provides an estimate of the surface absolute geostrophic velocity, and the moorings provide sheared velocity profiles relative to the surface. The mean component in the ADT, however, is subject to 5-10 cm of error over the Solomon Sea (Rio & Hernandez, 2004); thus, a time-invariant correction to the ADT-derived velocity is needed. The correction is estimated as the difference between surface velocity derived from the ADT and that from gliders which is 3.3 cm s^{-1} over the period when glider data are available (2007-2016). Thus, 3.3 cm s^{-1} was subtracted from the ADT-derived surface absolute geostrophic velocity (hereafter referred to as ADT_c) before it is combined with the mooring sheared velocity profiles that are referenced to the surface. The offset velocity between the mooring/PIES and mooring/ADT_c velocity profiles, determined separately over each PIES deployment period, is given by the difference between the mean profile of the two estimates.

The resulting absolute geostrophic velocity derived from our in-situ measurements re-

solves frequencies lower than the inertial period in this region (3 day) and spans a period of nearly 5 years (July 2012 - May 2017) overlapping with the 2015/2016 El Niño event. Thus, the resulting time series are useful to understand inflow variability on timescales longer than 3 days, i.e. subseasonal, seasonal, and interannual timescales.

4.3.4 Proxy volume transport from the satellite SLA

In addition to the observations, a proxy for the volume transport derived from the satellite SLA is used to examine variabilities on seasonal and interannual timescales. The proxy time series is based on a linear regression between the observed absolute volume transport in the 0-500 m layer over the 5 year observing period and satellite SLA at 3 locations: near Gizo Island (157.9° E, 9.1° S), near Vitiaz St. (147.4° E, 7.4° S), and within the SEC (157.9° E, 5.1° S; Figure 4.1). The locations were selected empirically to maximize the correlation between the proxy volume transport and the observations, but they also represent regions responsible for the flow variability in the Solomon Sea (Melet et al., 2010b; Cravatte et al., 2011; Hristova & Kessler, 2012). As the satellite-derived SLA near Vitiaz St. used in the regression is located in the coastal region where large uncertainties can arise in satellite SLA, it is compared to the nearby tide gauge station at Lae (Holgate et al., 2013; PSMSL, 2019), Papua New Guinea, (147.0° E, 6.75° S). The available tide gauge record is between September 1984 and January 2000 with intermittent gaps that are as large as 13 months. For the overlapping period of $\sim$63 months, the satellite SLA agrees reasonably well with tide gauge data ($r = 0.75$). Since the satellite SLA has roughly weekly resolution, a 10-day lowpass filter was applied to the volume transport and SLA time series. The concurrent SLA proxy time series can then be extended using the full 25-year satellite SLA measurement from 1993 to 2017. During the period overlapping with the observations, the proxy volume transport captures 64% of the variance in the observed transport. The explained variance is significantly higher than a proxy based simply on SLA at the two mooring sites which captures 50% of total variance of the observed inflow, while using more than three locations did

not substantially improve the skill. In addition, as pointed out by Kessler et al. (2019), a proxy derived simply from SLA at two locations across the southern entrance can easily fail to capture volume transport variations when the dominant subsurface layer flow does not correlate with flow in the surface layer.

For simplicity, the total volume transport across the southern entrance of the Solomon Sea over the 0-500 m depth layer will be referred to as the NGCC/NGCU current system; even though the NGCC and NGCU are usually confined to the western part of the basin and the NGCU often extends to 1000 m (Davis et al., 2012; Gasparin et al., 2012; Germineaud et al., 2016). We are decomposing the volume transport into the surface-layer flow, defined as flow across the southern entrance of the Solomon Sea from the surface to $\sigma_\theta = 24.0$ (equivalent to the mean depth of 130 m), and the thermocline-layer flow, defined as the flow from $\sigma_\theta = 24.0$ to 500 m. However, since our end-point observing system cannot capture the actual depth of the σ_θ = 24.0 isopycnal along the transect, the surface layer transport was estimated as the vertical integral of the across-transect mean velocity profile between the surface to the horizontal-average (but time-variable) depth of the σ_θ = 24.0 isopycnal between the two moorings multiplied by the transect length. The thermocline transport was computed similarly, except the vertical integral was calculated between the time-varying average depth of the 24.0 isopycnal and 500 m. The rms errors associated with the use of the across-transect average isopycnal depth and across-transect mean velocity profile rather than the true (but unknown) varying isopycnal depth and velocity along the transect are 0.8 and 1.3 Sv in the surface and thermocline layer, respectively. In each layer, the error was estimated using output from a global coupled 0.1° Parallel Ocean Program2/Los Alamos Sea Ice Model (POP2/CICE4; Appendix A) simulation as the rms difference between an end-point "mooring-like" volume transport and that calculated from the model density and velocity fields. The flow in the surface and thermocline layers will be interchangeably referred to as the NGCC and NGCU respectively. Inflow variability in three different frequency bands will be considered: between 3 and 60 days (subseasonal variability), between 60 and 400 days, and lower than 400

days (interannual variability). Separately, the seasonal cycle is examined.

4.4 Mean and variability of the NGCC and NGCU

4.4.1 Temperature and salinity relationship

Potential temperature versus salinity relationships from the 2012 - 2017 mooring deployments at the Misima (western side) and Gizo (eastern side) sites show a lower salinity range in the water column at Gizo relative to that at Misima (Figure 4.2), similar to the salinity profiles measured by gliders (Gourdeau et al., 2017). The signature of the South Pacific Tropical Water (SPTW), identified by a salinity maximum at σ_θ = 24.5, is apparent at both locations. In the thermocline layer, the Misima salinity is up to 0.1 higher than that at Gizo as the Gulf of Papua Current (GPC) and the NVJ that transport SPTW into the Solomon Sea mainly flow along the western part of the basin. In addition, the Gizo mooring salinity measurements show a distinct seasonal cycle at the depth of the salinity maximum (σ_θ = 24.5); relatively low salinity is present in March - April and high salinity is present in July - August. The seasonality in salinity at Gizo yields higher variability in dynamic height compared to that at Misima. Therefore, seasonal variability in the sheared component of the cross-passage volume transport is largely contributed by dynamic height variability in the eastern Solomon Sea at Gizo. The sheared transport produced by the Gizo dynamic height and the mean profile of Misima dynamic height can capture 83% of the sheared transport variance.

4.4.2 Mean and overview of the inflow variability

Vertical structure

Horizontally-averaged geostrophic velocity across the transect is presented in Figure 4.3a. The surface velocity is highly fluctuating. A poleward-flowing current is distinct from around

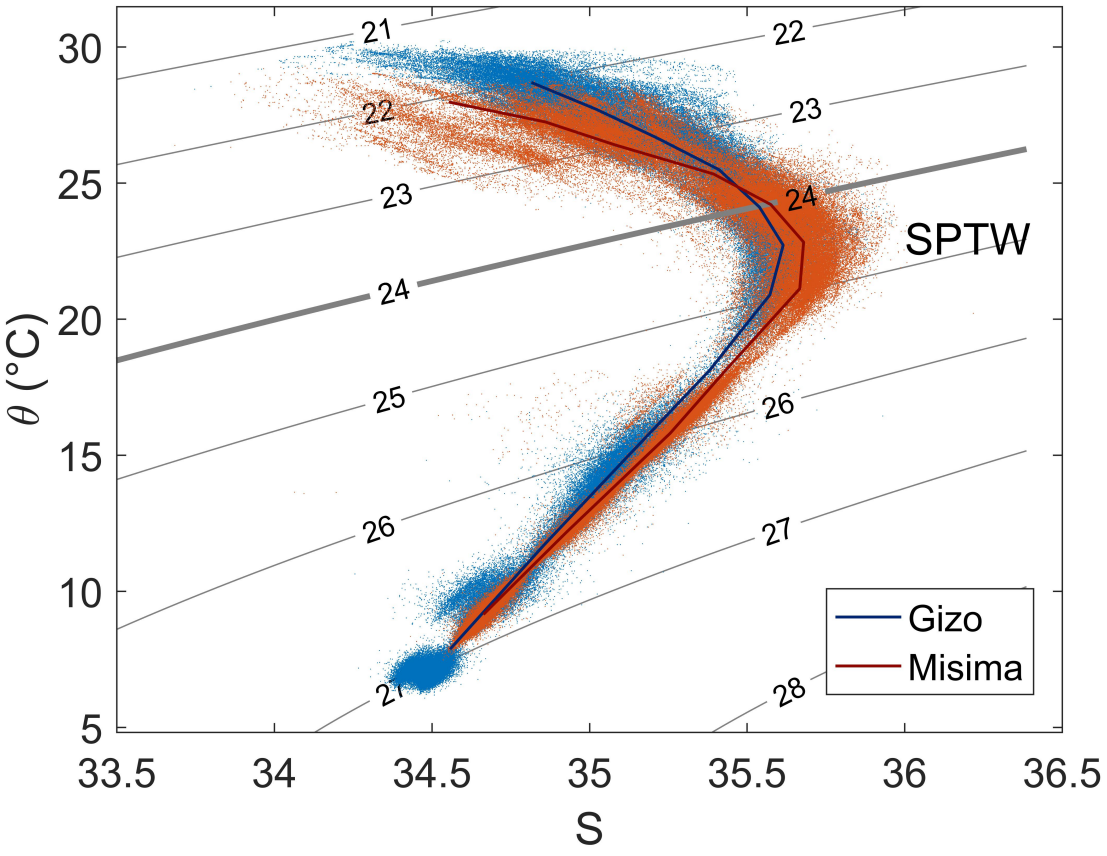

Figure 4.2: Scatter plot between potential temperature (θ) and salinity (S) at Gizo (blue) and Misima (orange) measured by moorings between July 2012 and May 2017 at 6 depth levels in the top 500 m of the water column overlaying isopycnal (σ_θ) contours. Mean $\theta - S$ at Gizo and Misima is plotted in dark blue and brown lines, respectively.

January to May in 2013, 2014, and 2017. The poleward current in 2015 is weak and in 2016 it is nearly absent. Between 120 and 300 m, a subsurface velocity maximum that intensifies in June - September of 2013 is present. To further investigate the vertical structure of the volume transport through the Solomon Sea, the time series of the velocity fluctuation profiles derived by removing the time-mean velocity profile over the period of the observations (Figure 4.3a) are decomposed into Empirical Orthogonal Functions (EOFs) and the corresponding Principal Components (PCs). The first two modes explain 98% of the variance (Figure 4.4). The first leading EOF mode, explaining 82% of the velocity variance, is surface-intensified and decays with depth. The corresponding PC highly correlates with volume transport in the 0-500 m depth layer ($r = 0.97$). The second EOF mode has a sheared structure with one maximum at the surface and the other at 300 m emphasizing the subsurface fluctuation in the transport. The depth of reversal is at 140 m similar to the mean depth of σ_θ = 24.0 supporting the choice of using σ_θ = 24.0 to separate the NGCC from the NGCU. The second PC corresponds more closely to the absolute geostrophic velocity at 500 m depth ($r = 0.74$).

Mean and variability

The absolute geostrophic transport in the upper 500 m estimated from the moorings and PIES over the period of July 2012 - May 2017 fluctuates between -20.6 and 43.9 Sv (positive equatorward) with a mean of 15.2 Sv, in good agreement with estimates from previous observations (Cravatte et al., 2011; Davis et al., 2012; Zilberman et al., 2013) and numerical simulation (Djath et al., 2014). The temporal standard deviation is 11.0 Sv (Figure 4.5a; Table 4.2). The rms error associated with the volume transport calculation which includes that from mooring interpolation and extrapolation (2.7 Sv), detrending of the PIES time series (3.0 Sv), instrument error (4.4 Sv), unresolved across-transect eddy propagation (3.0 Sv) and the use of constant f (1.5 Sv), is 6.8 Sv (variances of the different error components were added together; Thomson & Emery, 2014). In the surface layer, the volume transport across the transect ranges from -15.6 Sv

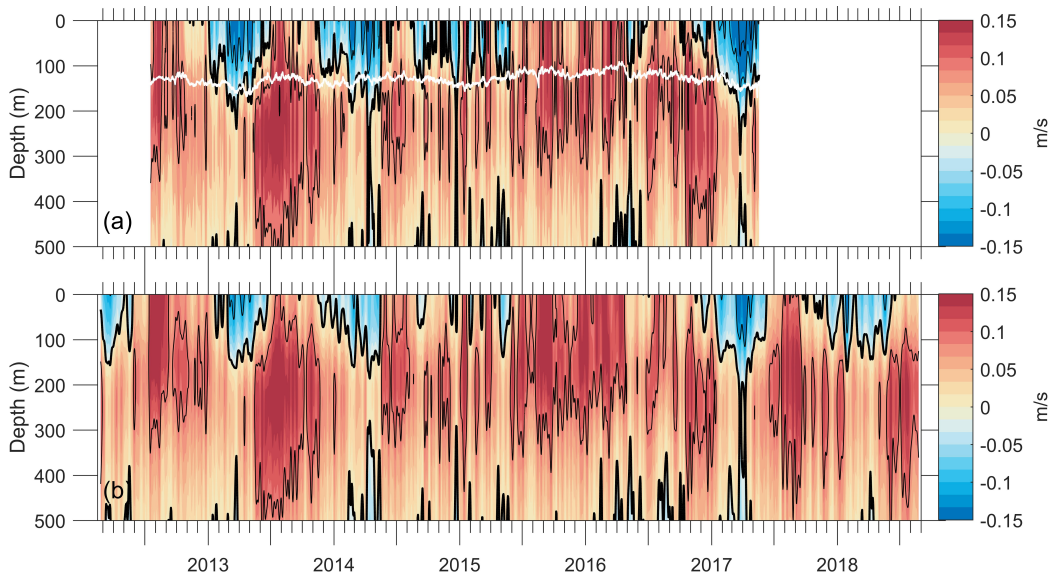

Figure 4.3: 3-day lowpass filtered across-transect mean velocity time series estimated from (a) moorings and PIES, and (b) PIES, ADT_c, and the first two empirical orthogonal functions (EOFs) derived from (a). The thick black line highlights the zero contour, the thin black lines represent 0.1 m s^{-1} contours, and the white line in (a) shows σ_θ = 24.0.

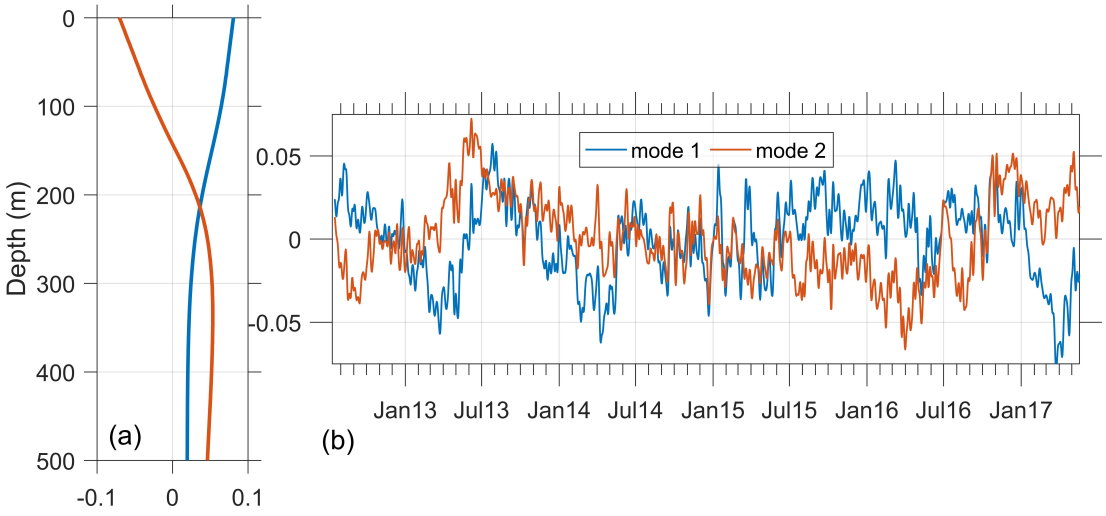

Figure 4.4: (a) The first two EOFs and (b) their corresponding principal components (PCs) computed from the 3-day lowpass filtered mooring/PIES velocity time series (Figure 4.3a).

Table 4.2: Mean and standard deviation of volume transport at the southern entrance of the Solomon Sea in the upper 500 m of the water column estimated from different techniques. Mean volume transport in the surface (surf.) and thermocline (therm.) layers is shown in the parenthesis.

Dataset	Time Period	Mean (Sv) (surf./therm.)	Standard Deviation (Sv)
Mooring/PIEs	July 2012 - May 2017	152 (1.7/13.5)	11.0
PIES/ ADT_c	February 2012 - September 2018	15.0 (2.7/12.3)	9.4
Proxy from ADT_c	January 1993 - December 2017	12.4	9.3

to 13.0 Sv with a mean of 1.7 Sv and has a strong annual cycle in the first two years of the record (July 2012 - July 2014). In the thermocline layer, the volume transport is usually equatorward and ranges from -5.0 to 33.6 Sv with a mean of 13.5 Sv (Figure 4.5b; Table 4.2).

The mean of the proxy transport is in good agreement with the shorter observed period at 12.4 Sv with a standard deviation of 9.3 Sv (Table 4.2). Note that the mean volume transport of the proxy and the observations is the same (15.2 Sv) during the overlapping period by construction as the proxy volume transport is derived from a linear regression between the observed volume transport and SLA over that period. However, when the regression-derived coefficients are applied to the SLA outside of that period, it can result in a different time mean over the extended period (1993 - 2017).

The glider transport error bar (Figure 4.5a) is estimated as the standard deviation of the mooring/PIES time series spanning 6 weeks centered at the time when the glider reaches its mid-crossing location. The error bar reflects the error from asynchronous sampling across the southern entrance by the glider. The mooring/PIES transport agrees well within their errors with most of glider transport estimates; the rms difference is 7.1 Sv. During May - November 2013, volume transport calculated from the mooring/PIES measurements is consistently higher than that from the glider measurements (Figure 4.5). Therefore, we compared the SLA derived from the mooring and PIES at the Gizo site, which has the dominant dynamic height signal, to the satellite along-track SLA during that period (not shown) to verify the mooring/PIES measurement. The

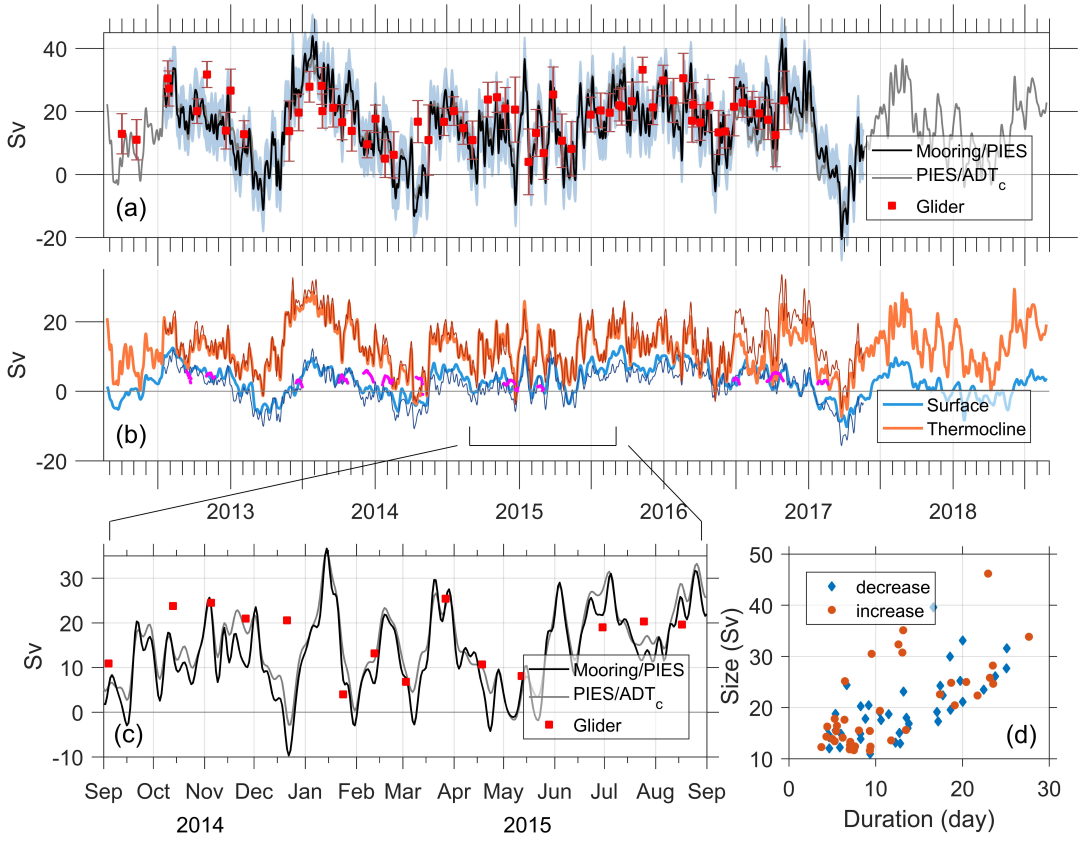

Figure 4.5: 3-day lowpass filtered absolute geostrophic volume transport calculated from the PIES/ADT$_c$ (gray), mooring/PIES observations (black) with the associated uncertainty shown in blue shading and volume transport calculated from glider measurements (red squares) with the estimated uncertainty shown in red bars, (b) the volume transport in the surface (thin blue) and thermocline (thin orange) layer computed from mooring/PIES measurements compared to those from PIES/ADT$_c$ reconstruction (thick lines). The thick magenta lines show some examples of net across-transect volume transport produced by an eddy propagating through the transect assuming a constant f. (c) Magnification of (a) over September 2014 to August 2015, and (d) scatter plot showing the magnitude and duration of extreme events identified from the 3-day lowpass filtered volume transport estimated from the mooring/PIES measurements.

along-track satellite SLA increases from April to July of 2013 and matches the amplitude of the mooring/PIES SLA. This evidence strongly corroborates the transport result calculated from the mooring and PIES measurements during this period. Ekman transport across the transect, which is not captured by our geostrophic transport estimates, is relatively small as the prevailing wind over the Solomon Sea is along the basin (northwestward or southeastward wind); the across-transect Ekman transport is at most 2.0 Sv with an rms value of 0.5 Sv.

Using the vertical EOF modes to reconstruct volume transport from PIES measurements and the ADT_c

In addition to the mooring/PIES observations, the volume transport inflow can be estimated from subsurface velocity derived from the PIES measurements, surface velocity derived from the ADT_c, and the first two vertical EOF modes from the 3-day lowpassed mooring/PIES time series (Figure 4.4a). The sole use of PIES and ADT_c allows for a more cost-effective means of long-term monitoring of the NGCC/NGCU at the southern Solomon Sea. Compared to the proxy volume transport that only uses the ADT_c, the addition of the PIES subsurface measurements both provides information on the vertical structure of the transport (Figure 4.3b) as well as improves the correlation of the volume transport with that computed from mooring/PIES measurements ($r = 0.95$; Figure 4.5a). A profile of horizontally averaged velocity across the transect is reconstructed as a linear combination of the first two EOF modes constrained by two direct measurements of geostrophic velocity derived from the ADT_c and PIES. The reconstructed velocity time series not only show the surface fluctuation, but also the subsurface core of the current (Figure 4.3b). The time series resolves variability on various timescales (Figure 4.5a, b) including much of the highly fluctuating subseasonal variability that cannot be resolved by the ADT_c alone (Figure 4.5c). The PIES/ADT_c combination also provides 6.5 years of inflow estimates from March 2012 to September 2018, and thus is useful for examining the inflow condition during and after the 2015/2016 El Niño.

The surface and thermocline volume transport was estimated as the reconstructed flow above and below the time-mean σ_θ = 24.0 isopycnal depth of 130 m (Figure 4.5b); assuming a constant depth layer yields uncertainty of 0.7 Sv in both the surface and thermocline layers. In the upper 500 m of the water column, the rms difference between the reconstructed and observed volume transport is 3.2 Sv over the overlapping period (Figure 4.5a). The largest discrepancy is near the surface (Figure 4.3, 4.5b) reflecting the inconsistency between the surface geostrophic velocity derived from the ADT_c and that estimated from the surface extrapolation of mooring dynamic heights.

Although the reconstructed velocity profile depends on the first two vertical EOF modes, it is not sensitive to the detailed structure of the EOFs. Using EOF modes calculated from glider measurements with one surface-intensified mode and one sheared mode with a subsurface maximum at approximately 300 m, the resultant velocity profiles are not significantly different from that reconstructed with EOFs from moorings and the PIES.

4.4.3 Variability of the Solomon Sea inflow

Subseasonal variability

The volume transport over the 0-500 m depth layer with frequencies lower than the inertial period (3 days) derived from mooring and PIES measurements reveals sudden changes in the inflow at the southern entrance of the Solomon Sea that are as large as 25 Sv over one week (Figure 4.5c). Extreme transport events are defined here as sudden changes in volume transport that are larger than the standard deviation of the volume transport (10.4 Sv; Table 4.2) that occur over less than 30 days with a rate greater than 1 Sv per day. The extreme events are scattered throughout the record but are more extreme and abundant during the onset of the 2015/2016 El Niño (from the end of 2014 to August 2015). A scatter plot shows the distribution of the event sizes (Figure 4.5d). The rate of change in volume transport ranges from 1 Sv per day (by

construction) to 3.9 Sv per day. Variance of the volume transport in the subseasonal frequency band (3-60 days) accounts for 37% of the total variance.

Remotely-sensed observational and numerical studies have suggested that mesoscale eddies are abundant at the entrance of the Solomon Sea (Melet et al., 2010b; Hristova et al., 2014). We want to explore whether these sudden changes we observe in the transport might be related to eddy variability at the entrance to the Solomon Sea. The mesoscale eddies in the Solomon Sea are more numerous in March - May and during La Niña conditions, while fewer eddies are observed in July - August and during El Niño conditions (Qiu & Chen 2004; Hristova et al., 2014; Gourdeau et al., 2014). When an eddy propagates across our observing transect, calculation error can arise as the eddy is not fully sampled by our end-point measurements. The across-transect volume transport is calculated based on the difference between dynamic height measured by the two end-point moorings assuming a constant f of the mid-latitude, although the moorings are at different latitudes (Figure 4.1). In a scenario of a symmetric eddy propagating across the observing transect, dynamic height at each flank of the eddy would adjust to compensate for the difference in f along the transect to balance the volume transported by the two flanks. This results in a net gradient in dynamic height which is observed by the moorings. With the constant f assumption, our calculation then yields a volume transport, although the eddy does not transport volume.

To estimate the error in our transport calculation arising from the cross-transect eddy propagation, 12 eddies were manually identified from the satellite SLA over the observing period. For the identified eddies, we calculated volume transport from the SLA using a constant f and 500 m depth layer to simulate that calculated from the mooring measurements. This estimate is compared to the "more resolved" volume transport calculated by varying f along the transect (Appendix B). The difference between the two estimates (V_e) roughly reflects an error of volume transport that our calculation produces when an eddy is present at the transect: examples are indicated in Figure 4.5b. This exercise illuminates two important results. First, the subseasonal

fluctuations due to the calculation error associated with the eddies rarely coincide with the observed extreme transport events. Second, the magnitude of the transport error attributed to the presence of an eddy is much smaller than the extreme transport events. The magnitude of V_e is at most 6.0 Sv when assuming an eddy depth of 500 m (Figure 4.5b), and only $\sim$3.6 Sv when an eddy depth of 300 m is assumed. Our observations show the abundance of the extreme transport events during the 2015/2016 El Niño (the end of 2014 to August 2015; Figure 4.5a) suggesting that the events are not related to the presence of mesoscale eddies. Also, the extreme transport events are often associated with sudden changes in both the surface and thermocline layers (Figure 4.5b) while the eddies are thought to intensify roughly over the upper 150 m (Hristova et al., 2014; Gourdeau et al., 2017).

In addition, Kessler et al. (2019) found that the dominant subseasonal variability at the surface is associated with the basin-scale eddy that propagates along the major axis of the Solomon Sea from the southern entrance toward the equator with a speed of $\sim$0.20 m s^{-1}. The analysis suggests a possibility of subseasonal variability in the transport observed by the moorings as an artifact of their locations that are not on the same phase line, i.e. the eddy arrives at Gizo $\sim$20 days before it does at Misima. Therefore, we performed a simple analysis on subseasonal variability of satellite surface velocity from locations on the same phase line across the southern entrance (not shown). The resultant surface velocity also shows energetic subseasonal variation that is comparable to the surface velocity derived from ADT at the mooring locations. The extreme transport events in our observations are therefore actual fluctuations in the flow. In section 5.2.1, we will discuss the mechanism associated with these rapid fluctuations.

Seasonal cycle

The seasonal cycle is computed from the observations by fitting annual and semiannual harmonics to the mooring/PIES transport time series. The seasonal cycle accounts for only 27% of the total variance reflecting a high variation from one year to another (Figure 4.6). The annual

harmonic contributes 22% while the semiannual harmonic contributes 5% to the total variance. The seasonal cycle has a maximum in July - August. The strengthening of the NGCC/NGCU results in broadening of the equatorward inflow that extends toward the eastern boundary of the Solomon Sea (Germineaud et al., 2016; Ganachaud et al., 2017); thus, the SPTW transported by the NGCC/NGCU is present in the eastern basin and high salinity at $\sigma_\theta = 24.5$ is observed at Gizo in July - August. A seasonal minimum inflow occurs in March - April when the Solomon Strait inflow brings anomalously fresh water into the Solomon Sea (Alberty, 2018) and at the Gizo site. The strong inflow from the Solomon Strait is mostly confined to the northern and eastern part of the basin (Melet et al., 2010b) resulting in seasonally low saline water observed at Gizo in March - April; thus, distinct salinity seasonality is measured by the Gizo mooring (see Section 4.4.1). The seasonal cycle shows a rapid increase of the equatorward flow from April to July and a gradual decrease during the rest of the year particularly from October to December.

Since the proxy volume transport covers a much longer period of 25 years, the proxy seasonal cycle can be computed by averaging each day of the year of the proxy volume transport over 25 years (Figure 4.6, 4.7a). Also in this case, the seasonal cycle of the proxy record has a minimum in March and maximum in July - August and explains 33% of the total variance. Similar to that derived from the observations, the proxy seasonal cycle shows asymmetry in the increasing and decreasing phases. The standard error ranges from 1 Sv in June - July to 1.9 Sv in March - April.

Interannual variability

The proxy interannual transport, calculated by removing the seasonal cycle and variability faster than 400 days, ranges from -10.7 to 9.4 Sv and is highly correlated with the mean sea surface temperature in the Niño 3.4 region (Figure 4.7b). Niño 3.4 explains 66% of the variance of the proxy interannual transport with a mean lag of 2.7 months, although the lag varies across different ENSO events. The variable lag is likely due to changes in wind stress patterns in the

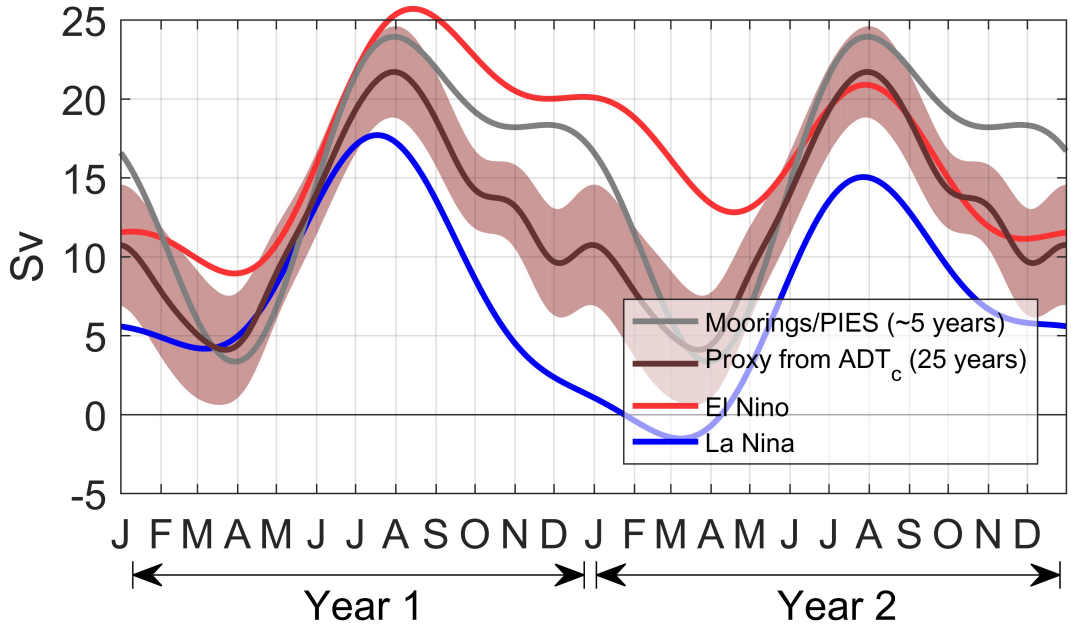

Figure 4.6: Seasonal cycle derived from fitting annual and semiannual harmonics to the moorings/PIES transport (black) and that derived from averaging proxy transport over 25 years (maroon) ± 2 standard errors (shaded maroon). Semiannual, annual, and biennial harmonics of the volume transport over the developing phase (Year 1) and decaying phase (Year 2) of El Niño (red) and La Niña (blue) years are also presented.

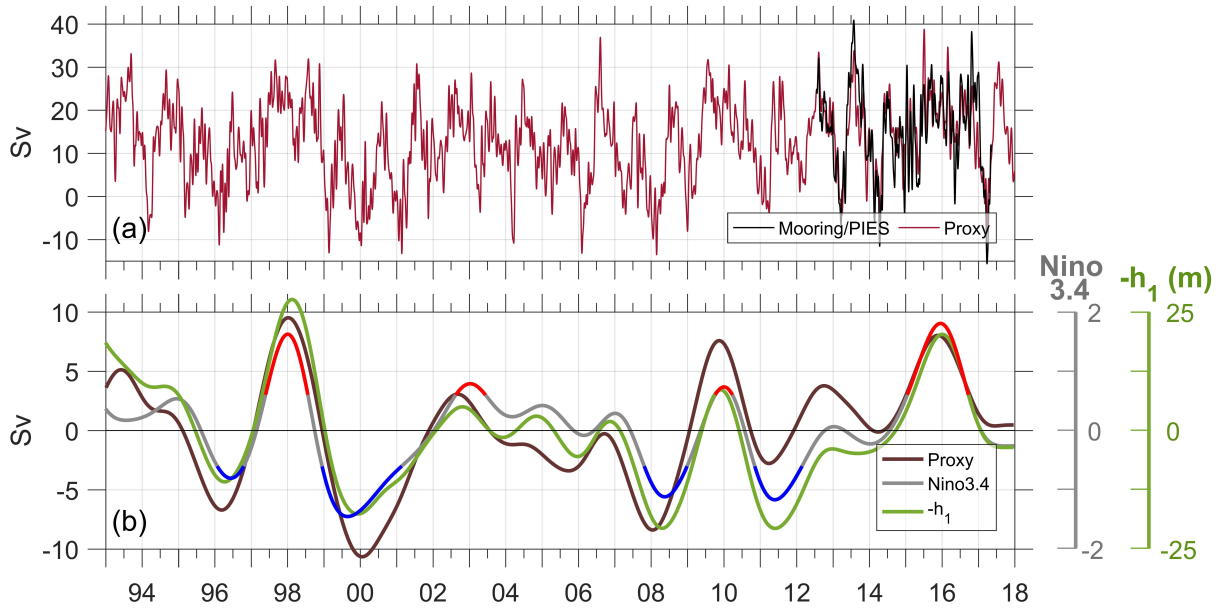

Figure 4.7: (a) The proxy volume transport (maroon) compared with the 10-day lowpass filtered mooring/PIES volume transport (black) over the upper 500 m of the water column, and (b) interannual component ($>$ 400 days) of the proxy volume transport (brown), interannual pycnocline depth near the Solomon Strait (h_1, green), and 2.7-month lag of Niño 3.4 index (gray). The Niño 3.4 index that is greater (less) than 0.6 (-0.6) is highlighted in red (blue) indicating El Niño (La Niña) condition.

interior of the Pacific Ocean during ENSO events that excite westward-propagating Rossby waves arriving at the western Pacific Ocean. During El Niño conditions, wind stress over the Solomon Island chain is northwestward and that over the equatorial Pacific is anomalously eastward causing negative wind stress curl between the equator and 15° S and east of the Solomon Island chain to approximately 140° W. Further south between 15° S and 25° S and west of 140° W, anomalous wind stress causes anomalous positive wind stress curl. The meridional opposing wind stress curl pattern in the western Pacific produces a meridional shoaling of the pycnocline toward the equator during El Niño. During La Niña conditions, the anomalous wind is generally in the opposite direction which causes deepening of the pycnocline toward the equator (Kessler & Cravatte, 2012). The mechanism suggests a modification of the SEC during both phases of ENSO events and implies that the dynamics governing the interannual variability of the downstream circulation into the Solomon Sea and the Coral Sea is fundamentally similar.

In addition, the semiannual, annual, and biennial harmonics were fitted to the proxy transport during El Niño (1997/1998, 2002/2003, 2009/2010, and 2015/2016) and La Niña years (1996/1997, 1999/2000, 2008/2009, and 2011/2012) to understand the impact of ENSO events on the seasonal cycle (Figure 4.6). The harmonics during El Niño conditions (September of the developing year (year 1) - April of the decaying year (year 2)) are significantly higher (5-13 Sv) compared to the 25-year proxy seasonal cycle. The seasonal minimum transport is anomalously high (at the end of March/ beginning of April of year 2), and the period of seasonal maximum is prolonged (June of year 1 - January of year 2). This results in a weak seasonal cycle during El Niño years. The opposite conditions appear in the harmonics of the transport during La Niña years. Minimum transport is intensified (3-11 Sv lower than the proxy seasonal cycle) and extended from December of year 1 to April of year 2, while the maximum transport in July - August is significantly lower than the proxy seasonal cycle during both year 1 and year 2. Compared with a previously estimated proxy of transport anomalies from satellite-derived SLA between Papua New Guinea and Solomon Islands over the 1993 - mid-2004 period (Melet et al., 2010b), our

interannual proxy (Figure 4.7) generally has higher fluctuations due to a thicker depth layer of 500 m compared to their 150 m depth layer. While our proxy exhibits similar features, higher interannual volume transport is present at the beginning of 1993 and lower transport occurs at the beginning of 2003.

The 2015/2016 El Niño

Both mooring/PIES observations and the proxy transport suggest that the interannual variability (>400 days) contributes 10% to the total variance. The across-transect mean velocity profiles show a weakening of the seasonal poleward surface flow in January - May of 2015, during the onset of the 2015/2016 El Niño (Figure 4.3). The poleward flow is nearly absent during the El Niño in 2016. Also, the seasonal maximum subsurface NGCU core in July - August does not extend as deep in 2014 - 2016 compared to that in 2013, 2017, and 2018. To examine the impact of the 2015/2016 El Niño on the inflow seasonal variability, signals with frequencies higher than 60 days and lower than 400 days were filtered out from the volume transport in the surface, thermocline, and upper 500 m of the water column (Figure 4.8a, b). While the variability in the 60-400 day band is distinct prior to July 2014 and after September 2016, the filtered transport over the 0-500 m depth layer clearly shows a weakened seasonal signal in July 2014 - August 2016 which is contributed by both surface and thermocline layers. Thus, the observations suggest a weakening of both surface and thermocline seasonal cycles prior to the 2015/2016 El Niño event (second half of 2014) and a suppression during and after the El Niño (January 2015 - September 2016) similar to the finding from the proxy transport (Figure 4.6). Following the El Niño event in September - December 2016, the volume transport in the thermocline layer increases before it returns to the values observed during pre-El Niño conditions in 2017. The increase in volume transport following an El Niño event was similarly suggested by glider observations after the 2009 El Niño (Davis et al., 2012). The increase corresponds to a strong subsurface core that extends over 100 - 500 m depth comparable to that which usually occurs during the seasonal

maximum in July - August (Figure 4.3, 4.8a).

4.5 Forcing mechanisms

4.5.1 Linear Rossby wave model

Model description

As westward-propagating Rossby waves from the interior of the Pacific Ocean arrive at the Solomon Sea, they modify the pycnocline depth and affect the local circulation. Thus, following e.g. Chen and Qiu (2004) and Kessler and Gourdeau (2007), we adopted a 1.5-layer linear Rossby wave model that predicts the depth of pycnocline (h; positive downward) in the Solomon Sea based on wind stress curl in the interior of the Pacific Ocean. As the deeper layer is stagnant by assumption, the derived pycnocline depth only reflects the depth that is forced solely by wind stress curl in the interior:

$$\frac{\partial h}{\partial t} + c_r \frac{\partial h}{\partial x} + Rh = -curl\left(\frac{\tau}{f\rho_0}\right), \tag{4.4}$$

where ρ_0 is surface density. Wind stresses (τ) are provided by the CCMP wind products and are averaged in 0.5° -1° latitude-longitude grid boxes. The mean long Rossby wave speed (c_r) is calculated at each latitude (y) across the Pacific Ocean using values provided by Chelton et al. (1998). The damping timescale (R) is chosen to be 1/24 months^{-1} and the result is not sensitive to the choice of R. The assumption of a stagnant deeper layer (i.e. the NGCU) is clearly not valid, but the variability of the NGCU resembles that of the NGCC ($r = 0.73$). Therefore the actual pycnocline depth slope still follows the sea surface slope but with a much smaller amplitude than that from the 1.5 layer case (the variability of the thermocline volume transport is $\sim$5% bigger than that of the surface transport; Figure 4.5b). Thus, the presence of the NGCU in this scenario only modifies the magnitude of pycnocline depth difference (Δh) across the Solomon Sea, but the

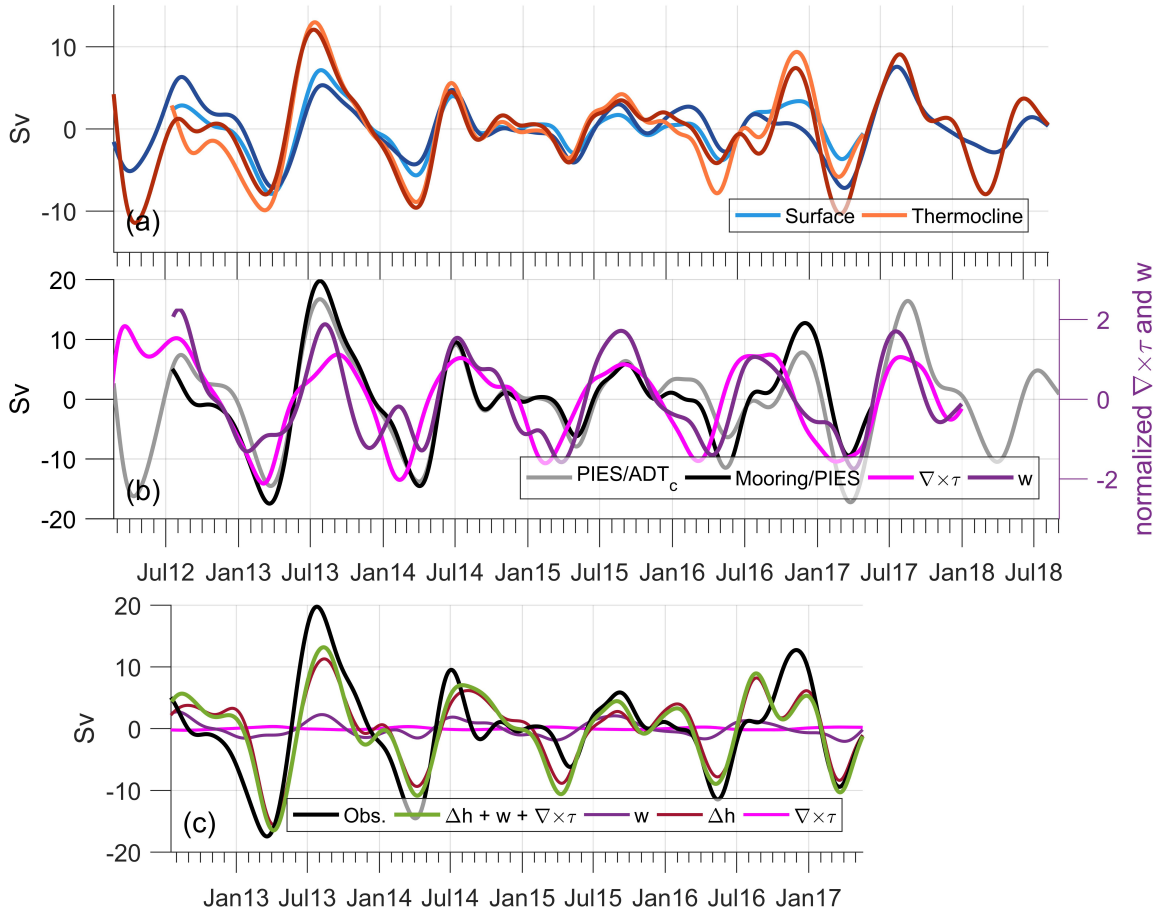

Figure 4.8: (a) 60 - 400 day demeaned filtered volume transport in the surface (light blue) and thermocline (orange) layers estimated from the mooring/PIES observations and from the PIES/ADT$_c$ reconstruction (dark blue and red), (b) 60-400 day demeaned filtered total volume transport over the upper 500 m of the water column from mooring/PIES (black) and PIES/ADT$_c$ (gray) in Sv compared to 60-400 day filtered wind stress curl in the western subtropical Pacific ($\nabla \times \tau$, magenta) and filtered local Ekman pumping (w, purple) normalized by their standard deviation, (c) 60-400 day filtered volume transport from mooring/PIES observations (black) compared to modeled volume transport (green) estimated from multi-variable regression using filtered pycnocline depth difference (Δh), w, and $\nabla \times \tau$. The model transport is decomposed into transport (Sv) contributed by Δh (maroon), w (purple), and $\nabla \times \tau$ (magenta).

proportionality with the surface layer flow remains. At each latitude, the general solution can be found by integrating Ekman pumping (RHS of Eq. 4.4) from the eastern boundary of the Pacific Ocean (x_E) along the Rossby wave characteristics:

$$h(x,y,t) = -\frac{1}{c_r(y)} \int_{x_E}^{x} \exp\left[-\frac{R}{c_r(y)}(x-x')\right] \times \text{curl}\left[\tau\left(x', y, t - \frac{x-x'}{c_r(y)}\right) / (f(y)\rho_0)\right] dx'. \quad (4.5)$$

Since wind stress and wind stress curl are much noisier than the volume transport particularly in the 3-10 day frequency band, the resultant h is much noisier compared to the volume transport. This reflects the limitation of the linear Rossby model in capturing variability of the inflow at high frequency. Therefore, a 10-day lowpass filter is applied to h and it is compared to the 10-day lowpass filtered volume inflow in the subsequent sections.

The observed volume transport

The locations where h is generated to produce Δh, the proxy for volume transport, were not at the actual mooring/PIES locations since the linear model only captures variability of h forced by Ekman pumping in the interior of the Pacific Ocean. The model also does not allow us to take the complex topography in the area into account and does not include the impact of coastal Kevin waves; the difference in h between the actual observing sites is therefore unlikely to adequately capture dynamics associated with the inflow. Rather, the locations were selected empirically based on the correlation between Δh and the NGCC and NGCU volume transports (Figure 4.9a). The difference between the pycnocline depth ($\Delta h = h_1 - h_2$) derived from the linear model evaluated at the Solomon Strait (h_1 at x_1 = 156° E, y_1 = 6° S) and the Gulf of Papua (h_2 at x_2 = 144° E, y_2 = 14° S; Figure 4.1) correlates well ($r = 0.81$) with the observed NGCC volume transport (Figure 4.9a). For the upper 500 m of the water column, Δh captures 46% of the total transport variance ($r = 0.68$). The decrease in the percentage of the explained variance indicates the reduced effect of the wind stress curl in the deeper part of the water column ($\sim$130-500 m).

The pycnocline variation implies the influence of Rossby waves at all latitudes between 6° to 14° S that reach the Solomon Island chain and travel along the coastal waveguide within the NGCC. Positive correlation indicates shoaling of h_1 and deepening of h_2 corresponding to an equatorward NGCC, and vice versa. Although some of the subseasonal variability including the extreme events in the NGCC is captured by Δh (e.g. in May - June 2013, June 2014, and January - February 2017), the model only explains a small fraction of the variance in the subseasonal frequency band.

The proxy volume transport (interannual variability)

The linear Rossby wave model is also used to study the impact of Rossby waves on the interannual variability of the proxy inflow. The interannual component (>400 days) of h_1, h_2 and the proxy volume transport over 1993 - 2017 period was examined. The interannual variability of both h_1 and h_2 are similar, despite a weaker signal and a lag in h_2 compared to h_1 due to its location further to the southwest and the slower propagation speed of Rossby waves there. The similarity is due to the interannual wind stress curl that is roughly uniform between the equator and 15° S to the west of 160° W (Kessler & Cravatte, 2012). Surprisingly, h_1 alone is a good indicator of the interannual variability of the Solomon Sea inflow over the upper 500 m of the water column ($r = 0.93$); it shoals during El Niño events and deepens during La Niña events (Figure 4.7b). This shows a strong association between Rossby waves arriving at the Solomon Strait and the Solomon Sea inflow over the top 500 m of the water column on the interannual timescales.

Contribution of wind stress curl in the Pacific to Δh variance

The cumulative variance of the pycnocline depth difference produced by the wind stress curl as a function of longitude (X) is calculated to understand the contribution of wind stress curl

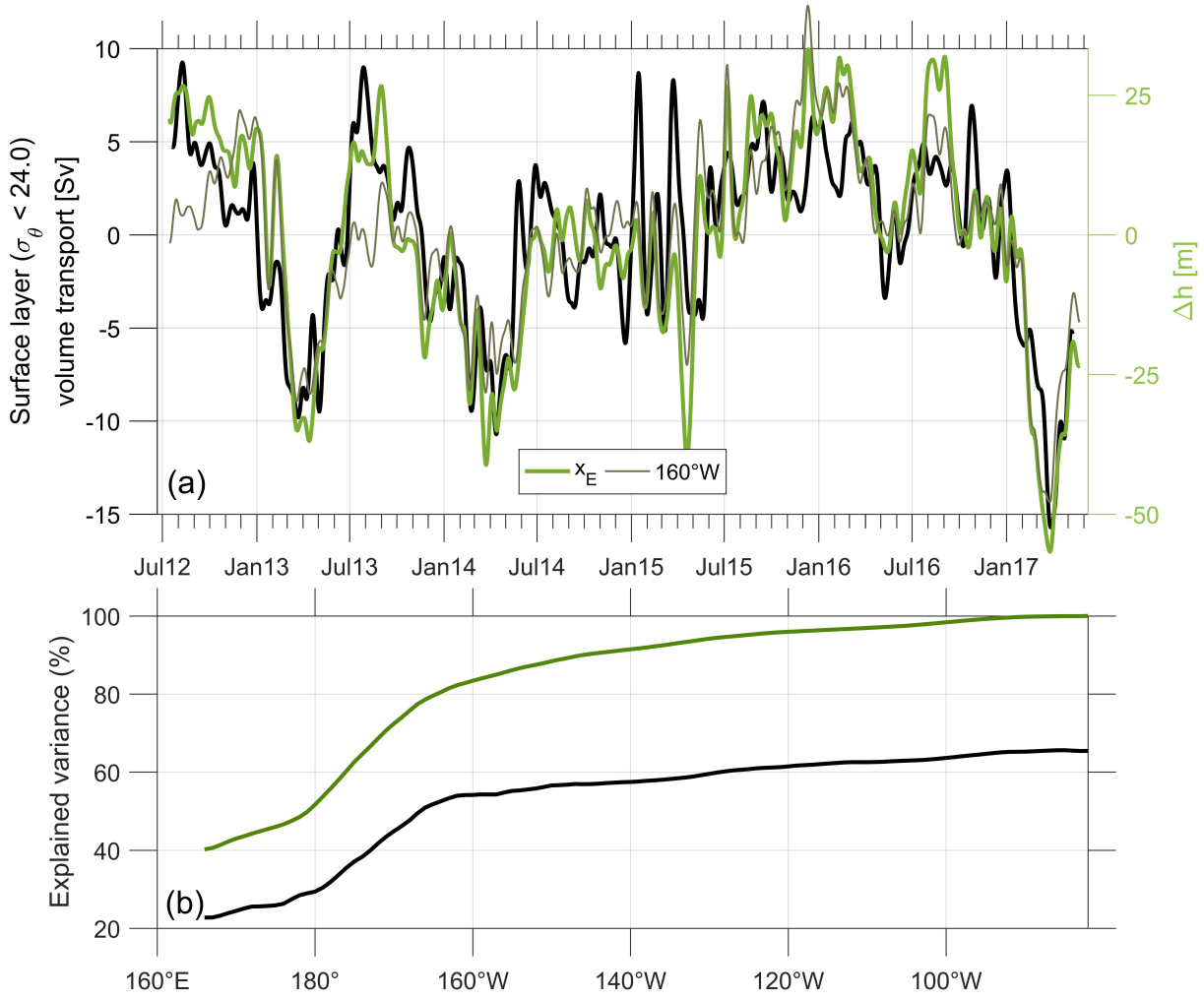

Figure 4.9: (a) 10-day lowpass filtered mooring/PIES surface volume transport with its mean removed (black) compared to Δh near the Solomon Strait (156° E, 6° S) and in the Gulf of Papua (144° E, 14° S) forced by wind stress curl to the west of the eastern boundary of the Pacific Ocean (x_E, bright green) and west of 160° W (thin dark green), and (b) percent of Δh (green) and the NGCC (black) variance explained by Δh forced by wind stress curl to the west of each longitude.

at each longitude (Qiu & Chen, 2010),

$$S(X) \equiv 1 - \frac{\langle [\Delta h(x_E,t) - \Delta h(X,t)]^2 \rangle}{\langle \Delta h^2(x_E,t) \rangle}, \tag{4.6}$$

where the angle bracket denotes the time average over the observational period (July 2012 - August 2017) and $\Delta h(X,t)$ is the difference between $h_1(X,t)$ and $h_1(X,t)$ where $h_1(X,t)$ and $h_2(X,t)$ are computed similarly from integrating Ekman pumping from X to x_1 and x_2,

$$h_1(X,t) = -\frac{1}{c_r(y_1)} \int_x^{x_1} \exp\left[-\frac{R}{c_r(y_1)}(x_1 - x')\right] \times \text{curl}\left[\tau\left(x', y_1, t - \frac{x_1 - x'}{c_r(y_1)}\right) / (f(y_1)\rho_0)\right] dx'. \tag{4.7}$$

Note that when replacing X with x_E, the result from Eq. 4.7 is the same as that from Eq. 4.5 when integrated to x_1 along y_1. The percentage of explained variance increases rapidly in the western Pacific Ocean, particularly to the west of 160° W (Figure 4.9b). The Δh forced by wind stress curl west of 160° W reproduces that forced by wind stress curl over the entire Pacific Ocean well and captures 54% of the total variance in the NGCC (Figure 4.9).

4.6 Local and Remote winds

Subseasonal timescale

Ekman pumping/suction ($w = \nabla \times \frac{\tau}{\rho f}$) and wind stress averaged in a 3° longitude × 1° latitude grid over and nearby the Solomon Sea are examined in an effort to understand the mechanism associated with the subseasonal variability and extreme transport events. The wind stress and wind stress curl are, however, much noisier than the volume transport particularly at frequencies higher than 10 days. Hence a 10-60 day bandpass filter, which preserves characteristics of the extreme events reasonably well, is applied to the wind forcing and volume transport to examine the impact of wind stress and wind stress curl on the subsesasonal inflow.

Ekman pumping near Gizo (centered at 9.5° S, 159° E), where high variability in dynamic height is found, is reasonably correlated with the bandpassed observations at a lead of 4-16 days; at a 11-day lead, it explains 24% of the variance and is significant at the 95% level (Figure 4.10a). Ekman suction is present at Gizo roughly 11 days before the maximum of the extreme events, while Ekman pumping is present about 11 days before the minimum of the events. A movie (not shown) of the bandpassed Ekman pumping over the Solomon Sea finds that the extreme events are usually associated with changes in Ekman pumping at either side of the southern entrance. Prior to a sudden increase of the volume transport, w increases at Gizo and decreases at Misima, which lowers the sea surface height (SSH) at Gizo compared to that at Misima driving the flow toward the equator. The opposite is observed for a sudden volume transport decrease.

The effect of wind stress on the subseasonal inflow variation is examined by simultaneously regressing zonal and meridional subseasonal (10-60 day) wind stress against the subseasonal volume inflow varying the lag in the volume transport from 0 to 20 days. The coefficients in front of the zonal and meridional wind stress components give the direction of wind stress that has the highest correlation to the subseasonal inflow (Peterson et al., 2012). High correlation values are found over the Coral Sea and south of the Solomon Sea when wind stress leads by 10-14 days (Figure 4.10b, c). Also, the inflow is mainly associated with southerly wind stress to the east of 155° E, south of 10° S. The highest correlation is found over the Coral Sea when wind stress leads by 11 days (19° S, 163.5° E; $r = 0.50$). The correlation decreases slightly with an increased lead in wind stress toward the southern entrance of the Solomon Sea implying that the subseasonal inflow variation is not locally driven by wind stress. Rather it suggests that the wind stress over the Coral Sea modifies the source of the NGCC/NGCU current system as the equatorward wind stress drives volume transport westward through Ekman dynamics creating a gradient in SSH that results in geostrophic equatorward volume transport. When considering the wind stress and Ekman pumping together through multi-variable regression, the result explains 33% of the subseasonal variability over the observing period. However, over the period with

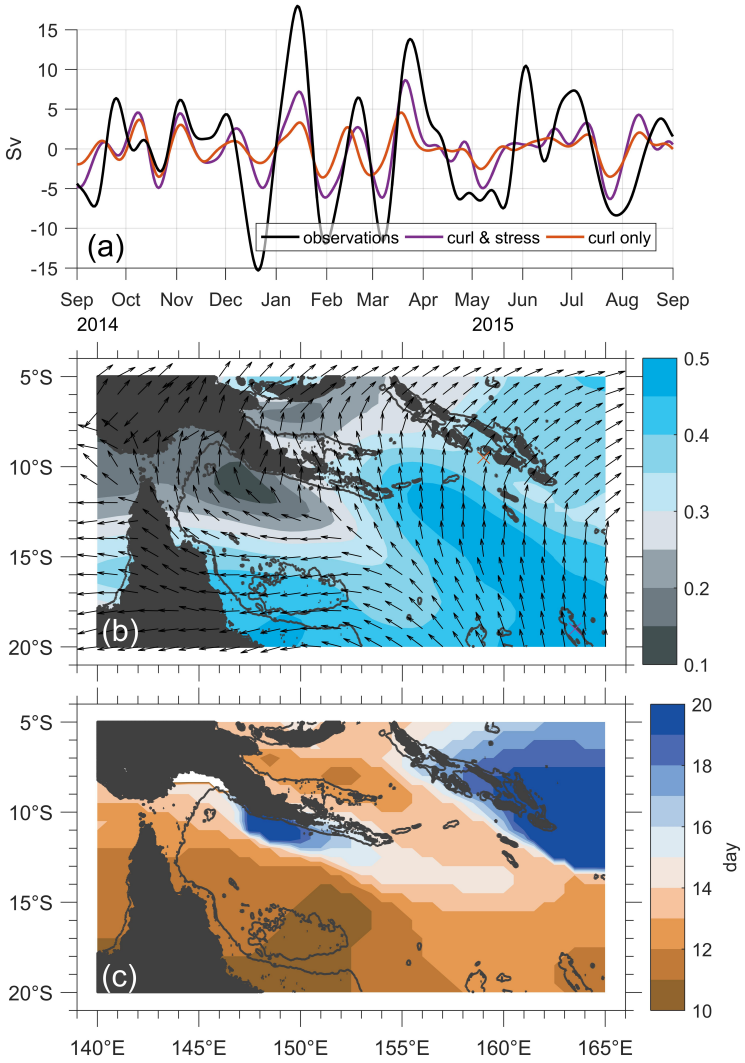

Figure 4.10: (a) Subseasonal (10-60 day) volume transport inflow (black) and estimated volume transport by linear regression with only wind stress curl that leads by 11 days (orange) and with both wind stress curl that leads by 11 days and concurrent wind stress (purple). (b) Direction of subseasonal wind stress (arrows) that yields maximum correlation between subseasonal volume transport and that calculated from the zonal and meridional wind stress through linear regression (color contour) with (c) the corresponding lead in the wind stress. The orange cross in (b) shows the location of wind stress curl used in the linear regression in (a) and the purple cross shows the location of maximum correlation between subseasonal volume transport and subseasonal wind stress.

pronounced extreme events (September 2014 - August 2015), the local and remote winds explain 58% of variance in the 10-60 day band (Figure 4.10a).

Variability between 60 and 400 days

The observed volume transport is first filtered to eliminate signals with frequencies higher than 60 days and lower than 400 days and is then compared to similarly filtered mean wind stress curl over the western subtropical Pacific and local Ekman pumping (Figure 4.8b). The annual variability of the circulation in the western subtropical Pacific is known to be driven by uniformly phased wind stress curl between 12° to 30° S as it alters the circulation of the subtropical gyre (Kessler & Gourdeau, 2007) and hence also potentially influences the Solomon Sea inflow. The mooring/PIES observations show an increase of the inflow with a lag of 34 days following an increase of wind stress curl averaged between 150° and 165° E, 10° and 20° S ($r = 0.71$). The time lag suggests a delayed response of the subtropical gyre circulation to the change in the wind stress curl. In addition, the effect of local Ekman pumping on the inflow is examined as it modifies annual variation of the surface velocity in the Solomon Sea (Melet et al., 2010a). Ekman pumping over the Solomon Sea exhibits clear variation; Ekman pumping (suction) is present in the western (eastern) part of the basin in August - September, while the opposite occurs in January - April. The Ekman pumping along either side of the basin correlates well with the inflow ($r = \sim 0.6$). However, a linear multi-variable regression of the mean wind stress curl, local Ekman pumping, and Δh from the Rossby model against the observed inflow shows that 60 - 400 day variability of the inflow is mainly associated with Δh (Figure 4.8c); Δh alone explains 65% ($r = 0.81$) of the variability. An addition of the wind forcing insignificantly increases the explained variance to 66%. Although high correlations are found between the wind forcing and the volume inflow, they are due to their distinct seasonal cycle (Figure 4.8b). Also, both filtered local Ekman pumping and remote wind stress curl exhibit little interannual variation compared to the filtered transport, i.e. seasonal cycle suppression in the Ekman pumping and wind stress curl is not apparent during

the 2014 - 2016 period. Therefore, we conclude that the Rossby waves that propagated from the interior of the Pacific Ocean between 6° and 14° S mainly influences the 60 - 400 day variability of the 0-500 m inflow at the southern entrance of the Solomon Sea.

4.7 Discussion

4.7.1 Extreme subseasonal changes in the volume inflow

The extreme transport events measured by the moorings and PIES are as large as the seasonal fluctuation of the inflow (Figure 4.5). The events are unlikely to be associated with mesoscale activities in this region (Figure 4.5b; Appendix B). They are more abundant and prevalent during the 2015/2016 El Niño (Figure 4.5c). During the neutral ENSO conditions (prior to July 2014 and after September 2016), the increasing (decreasing) extreme events are larger and more abundant between March and July of 2013 and 2014 (between August and February of 2012/2013, 2013/2014 and 2016/2017; Figure 4.5a). This suggests a connection between the extreme events and the seasonal cycle; sudden increases (decreases) in the volume transport are more dominant during the increasing (decreasing) phase of the seasonal cycle. The local wind stress curl produces a pycnocline tilt along the transect resulting in a sudden increase or decrease of the volume transport in the top 500 m of the water column, while the remote wind stress over the Coral Sea (19° S, 163.5° E) potentially modifies the source of the NGCC/NGCU current system. Overall, the local and remote winds together only explain 33% of the subseasonal variance (Figure 4.10) leaving a large portion of the variance unexplained. Intraseasonal Kelvin waves driven by anomalous westerly winds, such as those created by the Madden Julian Oscillation (MJO), could play an important role in influencing the observed subseasonal transport; intraseasonal Kelvin waves become more energetic and the MJO extends further east during El Niño conditions (Kessler 2001; Rydbeck et al., 2019). However, examining the influence of intraseasonal Kelvin waves on the subseasonal variability of the Solomon Sea inflow is beyond the scope of this study.

4.7.2 60 - 400 day variability and the seasonal cycle

Variability between 60 and 400 days accounts for half of the total variance in the volume transport at the southern entrance of the Solomon Sea; the variability is dominated by the seasonal cycle (annual plus semi-annual harmonics) that accounts for 27% of the total variance (Figure 4.6). While previous studies suggest the influence of western Pacific subtropical wind stress curl, local Ekman pumping, and westward propagating Rossby waves on Solomon Sea circulation, we found that only the impact of Rossby waves forced by Ekman pumping in the interior of the Pacific (Eq. 4.4) significantly influences the 60-400 day transport variability (Figure 4.8c). The Rossby waves potentially determine the seasonal latitudinal shift of the SEC that previous observations and numerical studies have identified to influence the circulation in the Solomon Sea (Chen & Qiu, 2004; Melet et al., 2010a; Cravatte et al., 2011). The SEC core located at 8° - 10° S strengthens the westward-flowing NVJ and increases the volume transport into the southern Solomon Sea during the period of maximum inflow (July - August), whereas the SEC core is near the Solomon Strait (3° - 6° S) during the period of minimum inflow at the southern entrance (March - April). The northward migration of the SEC during March - April strengthens the flow into the Solomon Sea at the Solomon Strait (Germineaud et al., 2016; Alberty, 2018). At the surface, the Solomon Strait inflow turns southeastward and exits the Solomon Sea at the southern entrance (Hristova & Kessler 2012) consistent with the seasonal poleward surface flow from the mooring/PIES observations (Figure 4.3).

4.7.3 2015/2016 El Niño compared with other El Niño events

The intensity and development of the 2015/2016 El Niño was very different from other El Niño events (McPhaden, 2015; Jacox et al., 2016). The 2015/2016 El Niño developed while the equatorial Pacific was already anomalously warm due to anomalous bursts of westerly winds along the equator in the previous year (at the beginning of 2014). This results in one of only

a few El Niño events that are associated with warming of the tropical Pacific extending over a one-year period (Harrison & Larkin, 1996; McPhaden, 2015; Levine & McPhaden, 2016). During the period when the tropical warm water volume grows quickly in the first half of 2014 (Levine & McPhaden, 2016), the NGCC/NGCU shows no significant change. However, seasonality in both the NGCC and NGCU is suppressed in late 2014 (Figure 4.3, 4.5, 4.8) when the El Niño development ceased due to a strengthening of the easterlies (Levine & McPhaden, 2016), i.e. the suppression occurs even before the mature phase of the 2015/2016 El Niño in the second half of 2015. Although the warm condition ends roughly in June 2016 (Figure 4.7b), the seasonal cycle remains suppressed until August 2016. This suggests a strong response of the LLWBC during the 2015/2016 event to the tropical warm water volume with a lag of about 3-6 months. During more "typical" El Niño events, the inflow interannual variability is expected to not exceed 9 Sv (Figure 4.7b) and the seasonal cycle should not be suppressed for a period longer than 2 years.

4.8 Summary

The mooring and PIES measurements, together with the remotely-sensed satellite altimetry, provide the first high temporal resolution volume inflow observations at the southern entrance of the Solomon Sea (Figure 4.5) along with the mean across-transect velocity profiles in the upper 500 m of the water column (Figure 4.3). Velocity profiles are also reconstructed from the satellite surface velocity and PIES subsurface velocity as a linear combination of the leading vertical EOF modes derived from the mooring/PIES measurements. The strong subsurface flow in July - August is correctly estimated by the reconstruction and the surface poleward flow during January - May period is clearly observed. The reconstructed velocity partially resolves the high-frequency variability that is not observed in the satellite surface velocity alone. Both time series reveal energetic volume fluctuation at subseasonal, seasonal, and interannual timescales.

The majority of the energy in the total variance lies within the 60-400 day frequency band;

the dominant variability is described by weak equatorward volume transport in January - May and strong equatorward transport in June - October consistent with that described by previous studies (Cravatte et al., 2011; Davis et al., 2012; Kessler et al., 2019; Figure 4.6, 4.8b). The weak flow is due to the seasonal reversal of the NGCC, while the strong flow is caused by seasonal strengthening of the NGCU (Figure 4.3, 4.5). The observations show that the inflow is primarily driven by westward-propagating Rossby waves at the seasonal timescale consistent with findings from previous numerical and altimetric studies (Chen & Qiu, 2004; Melet et al., 2010a; Melet et al., 2010b; Gourdeau et al., 2014). The Δh derived from the linear Rossby model (Eq. 4.4), particularly between 6° and 14° S, west of 160° W, can reproduce 54% of the inflow variance (Figure 4.9).

The interannual variability of the inflow is closely related to ENSO as described by earlier observational studies (Davis et al., 2012; Zilberman et al., 2013; Kessler et al., 2019; Figure 4.7b). In addition, our observations show the strengthening of the equatorward flow in the upper 500 m of the water column accompanied by the weakening of the seasonal cycle (Figure 4.5); the El Niño suppresses the seasonal cycles of both the NGCC and the NGCU (Figure 4.3, 4.8). The proxy transport shows the weakening of seasonal cycle during other El Niño events, particularly from September of year 1 to April of year 2 (Figure 4.6). During La Niña conditions, the phase of seasonal minimum flow is prolonged and the minimum is intensified. The inflow fluctuation is also well-captured by the modeled pycnocline depth near the Solomon Strait; it explains 86% of the interannual variance (Figure 4.7b). In addition, the high temporal resolution of the observations allows us to examine the inflow variability that is as fast as 3-60 days that accounts for 37% of the total variance. Vigorous subseasonal volume fluctuations that contain more than a third of the total energy in the volume transport are found (Figure 4.5c, d) emphasizing the need for continuous high temporal resolution inflow monitoring. The subseasonal fluctuation can be explained partly by the local and remote winds (Figure 4.10). Still a large fraction of the subseasonal variability cannot be explained and remains an open question for future studies.

Acknowledgements

This project is a part of the Consortium on the Ocean's Role in Climate (CORC) supported by National Oceanic and Atmospheric Administration (NOAA) through grants NOAA -NA15OAR4320071. This material is based upon work supported by the National Aeronautics and Space Administration under Grant Number 80NSSC17K0373 to Arachaporn Anutaliya. Any opinions,findings, and conclusions or recommendations expressed in this material are those of the author(s) and do not necessarily reflect the views of the National Aeronautics and Space Administration. Janet Sprintall was supported by National Science Foundation Grant OCE1029487. Julie L. McClean was supported by DOE U.S. Office of Science Award DE-SC0012778. Mooring and PIES measurements were collected and made freely available by the international OceanSITES project and the national programs that contribute to it. The authors would like to thank R. Davis from Scripps Institution of Oceanography (SIO) and W. Kessler (NOAA/Pacific Marine Environmental Laboratory) for the Spray underwater glider measurements (under the CORC program) and your generous help regarding the data handling. Argo data were collected and made freely available by the International Argo Program and the national programs that contribute to it (http://www.argo.ucsd.edu and http://argo.jcommops.org). The Argo Program is part of the Global Ocean Observing System. This study has been conducted using E.U. Copernicus Marine Service Information (http://marine.copernicus.eu/services-portfolio/access-to-products/?option=com_csw&view=details&product_id=SEALEVEL_GLO_PHY_L4_REP_OBSERVATIONS_008_047). CCMP Version-2.0 vector wind analyses are produced by Remote Sensing Systems.Data are available at www.remss.com. We would like to acknowledge high-performance computing support from Yellowstone (ark:/85065/d7wd3xhc) provided by NCAR's Climate Simulation Laboratory, sponsored by the National Science Foundation. Funding for the POP simulation was provided by a DOE BER grant entitled "Ultra High Resolution Global Climate Simulation" via a Los Alamos National Laboratory sub-contract. We are grateful for support

by the local authorities and partners, including Prof. Chalapan Kaluwin of the University of Papua New Guinea, cognizant PNG agency, Danny Kennedy of Dive Gizo, Mr. Chanel Iroi of the Solomon Islands Meteorological Service. Thanks to Bruce Cornuelle, Sarah Gille, Shantong Sun, and Marion Alberty (all SIO) for helpful discussion and help improve the results. Thanks to three anonymous reviewers for their constructive comments.

Chapter 4, in full, is a reprint of the material as it appears in Journal of Geophysical Research, "Mooring and seafloor pressure end-point measurements at the southern entrance of the Solomon Sea: subseasonal to interannual flow variability", by A. Anutaliya, U. Send, J. Sprintall, J. L. McClean, M. Lankhorst, and J. Koelling (2019). The dissertation author was the primary investigator and author of this paper.

Chapter 5

Observations of the Solomon Sea inflow and outflow

5.1 Introduction

Flow through the Solomon Sea in the tropical southwest Pacific Ocean, is mainly dominated by a Low Latitude Western Boundary Current (LLWBC) system consisting of the New Guinea Coastal Current (NGCC) and New Guinea Coastal Undercurrent (NGCU). The currents enter the Solomon Sea at its southern entrance and leave at three main exits: Vitiaz Strait, St. George's Channel, and Solomon Strait, located to the north of the Sea (Figure 5.1). The LLWBC plays an important role in transporting water from the subtropics to the equatorial region of the Pacific Ocean, hence contributing to the characteristics and quantities of equatorial water masses (McCreary and Lu, 1994; Johnson and McPhaden 1999; Lee and Fukumori 2003). Variability of the LLWBC is also highly correlated with the volume of warm water in the equatorial Pacific (Ishida et al., 2008) that influences El Niño Southern Oscillation (ENSO) (Wyrtki, 1985). Therefore, determining the volume transport and examining the variability and pathways of flow through the Solomon Sea would allow a better understanding of equatorial dynamics.

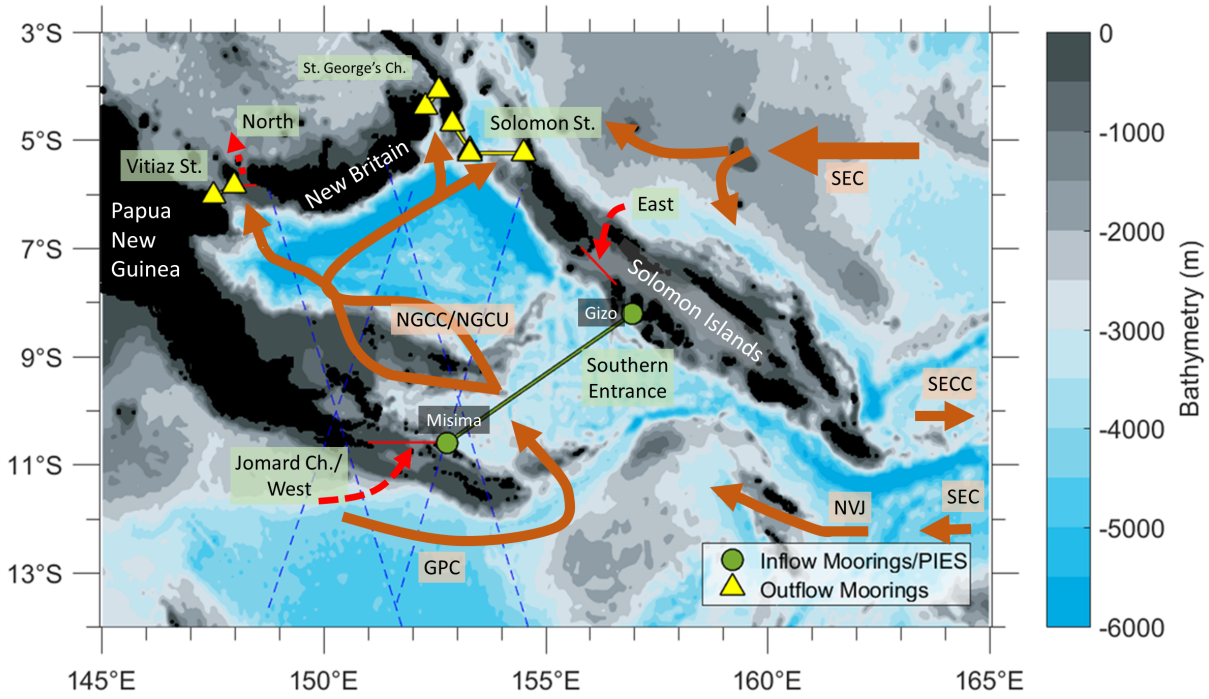

Figure 5.1: Bathymetry of the Solomon Sea and its surroundings along with the location of the moorings at the southern entrance and the three main exits. A schematic of the dominant currents in the Solomon Sea region are shown by the orange arrows and possible flow through the side channels are shown by the red dashed arrows; NGCC/NGCU denotes the New Guinea Coastal Current/New Guinea Coastal Undercurrent, GPC is Gulf of Papua Current, NVJ is the North Vanuatu Jet, SEC is the South Equatorial Current, and SECC is the South Equatorial Countercurrent. Locations of the along-track satellite sea surface height transects used for volume transport proxy through Jomard Channel is shown by blue dashed lines.

Despite the importance of the LLWBC, measurements in the Solomon Sea have been quite sparse in the past. Long-time mean volume transport has been estimated from historical hydrographic data (Cravatte et al., 2011), Argo float measurements (Zilberman et al., 2013) or volume transports have been calculated from discrete cruises (e.g. Butt and Lindstrom, 1994; Gasparin et al., 2012). Continuous observations of flow through the Solomon Sea only began in the last decade when the first glider was deployed in 2007 (Davis et al., 2012; Kessler et al., 2019). Subsurface moorings and bottom pressure sensors were deployed in 2012 at the southern entrance of the Solomon Sea (Anutaliya et al., 2019). The volume time series determined from these instruments show high variability on subseasonal, seasonal, and interannual timescales with a time-mean value of 15-20 Sv in the 0-700 m depth layer (Davis et al., 2012) and 15 Sv in the 0-500 m depth layer (Anutaliya et al., 2019). At the main exits of the Solomon Sea, moorings were deployed to examine the partitioning and properties of the flow leaving the Solomon Sea over the July 2012 - February 2014 period (Alberty et al., 2019; Ganachaud et al., 2014). At the exits, the flow is highly fluctuating at subseasonal and seasonal timescales with a mean value of 17.3 Sv above $\sigma_\theta = 26.7$ (mean depth of $\sim$400 m).

This study aims to compare the recent time series of flows into the Solomon Sea (hereafter referred to as the inflow) and out of the Solomon Sea at the three main exits (hereafter referred to as the outflow or the total outflow) for the overlapping period of July 2012 - February 2014, focusing on the high-frequency mooring and PIES observations. Together with the observations, output from a global ocean general circulation model (OGCM) simulation that is mesoscale eddy-resolving in the study region will also be examined to determine the relationship between the Solomon Sea inflow and outflow. The paper is organized as follows. Section 2 describes the mooring observations and the numerical simulation, while the comparison between the inflow and the outflow from the observations and numerical simulation is discussed in Sections 3 and 4, respectively. The summary and discussion are presented in Section 5.

5.2 Datasets

5.2.1 Observations

Solomon Sea Inflow

Volume transport and mean across-transect velocity in the upper 500 m of the water column were calculated from continuous measurements of end-point subsurface dynamic height moorings and pressure sensing inverted echo sounders (PIES) (Anutaliya et al., 2019). The mean velocity is integrated horizontally across the transect to obtain transport per unit depth and interpolated onto a vertical grid with a regular spacing of 20 m. The instruments were deployed near Gizo, Solomon Islands (8.2° S, 157.0° E), and near Misima island, Papua New Guinea (10.6° S, 152.8° E) over a period from July 2012 to May 2017 (Figure 5.1). Detailed information on the moorings and PIES deployment as well as calculation of the across-section velocity and volume transport are found in Anutaliya et al. (2019). The moorings and PIES only capture the geostrophic component of the current. The Ekman velocity (u_e and v_e) component is estimated as a function of depth (z), in the same way as Alberty et al. (2019), using an estimate of empirical turbulent viscosity (A) from Santiago-Mandujano and Firing (1990):

$$u_e = \frac{\sqrt{2}}{fd} e^{z/d} \left[\tau^x \cos\left(\frac{z}{d} - \frac{\pi}{4}\right) - \tau^y \sin\left(\frac{z}{d} - \frac{\pi}{4}\right) \right], \tag{5.1}$$

$$v_e = \frac{\sqrt{2}}{fd} e^{z/d} \left[\tau^x \sin\left(\frac{z}{d} - \frac{\pi}{4}\right) + \tau^y \cos\left(\frac{z}{d} - \frac{\pi}{4}\right) \right], \tag{5.2}$$

where f is Coriolis parameter, d (defined as $\sqrt{\frac{2A}{|f|}}$), where A is a function of wind speed and ranges from 0 to 0.03 m^2/s at the southern entrance) is the surface Ekman layer thickness, and τ^x (τ^y) is zonal (meridional) wind stress obtained from the Version 2 Cross-Calibrated Multi-Platform (CCMP). The CCMP are gridded surface vector winds with a ¼° resolution and a temporal resolution of 6 hours (Wentz et al., 2015). The mean across-transect Ekman transport

Table 5.1: Mean, standard deviation, and estimated error of the observed volume transport from July 2012 to February 2014 in the upper layer (shallower than σ_θ = 26.7) across each channel. Values from POP outputs over the 2005 - 2009 period are presented in parentheses.

Channel	Mean (Sv)	Standard deviation (Sv)	Estimated error (Sv)
Southern entrance	13.8 (17.4)	9.8 (6.9)	3.3
All exits	17.3 (17.6)	6.5 (6.6)	2.1
Vitiaz St.	9.1 (12.4)	2.1 (2.8)	1.9
St. George's Ch.	1.8 (1.3)	1.5 (0.7)	0.3
Solomon St.	6.4 (3.9)	4.9 (4.9)	0.8

is small with a root-mean-square (rms) value of 0.5 Sv; the surface Ekman velocity has strong seasonal cycle ranging from -0.15 m/s in June - July to 0.15 m/s in January - March. Uncertainty of the instantaneous volume transport above σ_θ = 26.7 is estimated to be 5.8 Sv by Anutaliya et al. (2019). Uncertainty of the time-mean volume transport of 3.3 Sv is obtained by dividing the instantaneous uncertainty by the square root of the number of independent observations (determined using an autocorrelation function) over the 19-month period.

Solomon Sea Outflow

Subsurface moorings were deployed at the major exits of the Solomon Sea: Vitiaz Strait (3 moorings), St. George's Channel (2 moorings), and Solomon Strait (4 moorings), from July 2012 to March 2014 (Alberty et al., 2019) (Figure 5.1). The moorings were equipped with acoustic Doppler current profilers (ADCPs) to measure velocity from the near surface (30-50 m) to near the bottom. The measured velocity at each passage was then interpolated across each channel and also extrapolated to the surface and bottom. Alberty et al. (2019) provide further details of the mooring deployments and the velocity interpolation/extrapolation, as well as different schemes of velocity interpolation/extrapolation and the sensitivity of the total transport estimates to these choices. In this study, we use the volume transport based on the "most-realistic" velocity interpolation and extrapolation as well as the uncertainty associated with the volume transport provided by Alberty et al. (2019) (Table 5.1).

In addition to cross-transect velocity and transport per unit depth, volume transport at both the inflow and outflow will be analyzed. As the deepest measured depth of the inflow mooring is at 500 m, the volume transport above the surface and thermocline layer, defined here as flow above σ_θ = 26.7 (equivalent to a mean depth of $\sim$400 m at both the entrance and the exits) and hereafter interchangeably referred to as the upper layer, will be analyzed to understand the relationship between the inflow and the outflow.

5.2.2 Numerical Simulation

The seasonal cycle of Solomon Sea inflow and outflow is investigated using a 0.1° configuration of the Parallel Ocean Program 2 (POP2) that is coupled to the Los Alamos Sea Ice Model (POP2/ CICE4) and run in the Community Earth System Model (CESM) framework (McClean et al., 2018). In addition, the volume storage in the Solomon Sea is also examined using model output. POP/CICE has a spatial resolution of approximately 11 km in this region and is configured on a global tripole grid with 42 vertical levels and partial bottom cells. It is forced with Co-ordinated Ocean-ice Reference Experiments II (CORE-II) interannually-varying atmospheric surface fluxes (Large and Yeager, 2009) and run from 1948-2009. The POP bathymetry is based on the high-resolution ETOPO2v2 (Smith and Sandwell, 1997). The POP output analyzed here consists of three-dimensional daily-averaged velocity, potential density, sea surface height, and wind stress for 2005-2009.

5.3 Across-transect velocity and volume transport from the observations

5.3.1 Mean and overall variability of the inflow and outflow

The mean volume transport at the southern entrance of the Solomon Sea in the upper layer is 13.8 $\pm$ 3.3 Sv (equatorward transport is positive) while that at the three main exits is 17.3 $\pm$ 2.1 Sv over the period of July 2012 - February 2014 (Table 5.1). The difference between the mean inflow and outflow transports occurs mainly in the subsurface transport (Figure 5.2a, b); the mean maximum inflow of 51.6 Sv/km (1 Sv/km = 10^3 m^2/s) is at 230 m depth while the mean maximum outflow reaches 81.4 Sv/km at a similar depth of 210 m (Figure 5.2f). At the exit, the mean total subsurface flow is dominated by outflow in both Vitiaz Strait and Solomon Strait, although the vertical structure of the mean total outflow largely resembles that of flow at Solomon Strait. Temporal variability of the transport per unit depth at the southern entrance agrees well with that at the three main exits with strong (weak) equatorward subsurface flow and equatorward (poleward) surface flow in June - September (January - May) (Figure 5.2a-d). The vertically integrated volume inflow in the upper layer also agrees with the total outflow within their uncertainties, despite a few exceptions such as in November 2012, January - February 2013, and April 2013 (Figure 5.3a). Overall, the outflow is greater than the inflow; periods when the inflow is greater than the outflow are only briefly evident (less than 2 months) (Figure 5.3b). The difference between the inflow and outflow does not have distinct seasonal variability.

In general, the volume inflow per unit depth correlates well with the total volume outflow per unit depth with correlation coefficients (r) exceeding 0.5 (significant at 95% level) at all gridded depth levels in the upper 500 m of the water column (Figure 5.2e). The highest correlation is 0.9 at 110 m depth and the lowest correlation is 0.5 at 290 m depth. Note that both the inflow and outflow in the upper $\sim$60 m of the water column are estimated with higher uncertainties as the

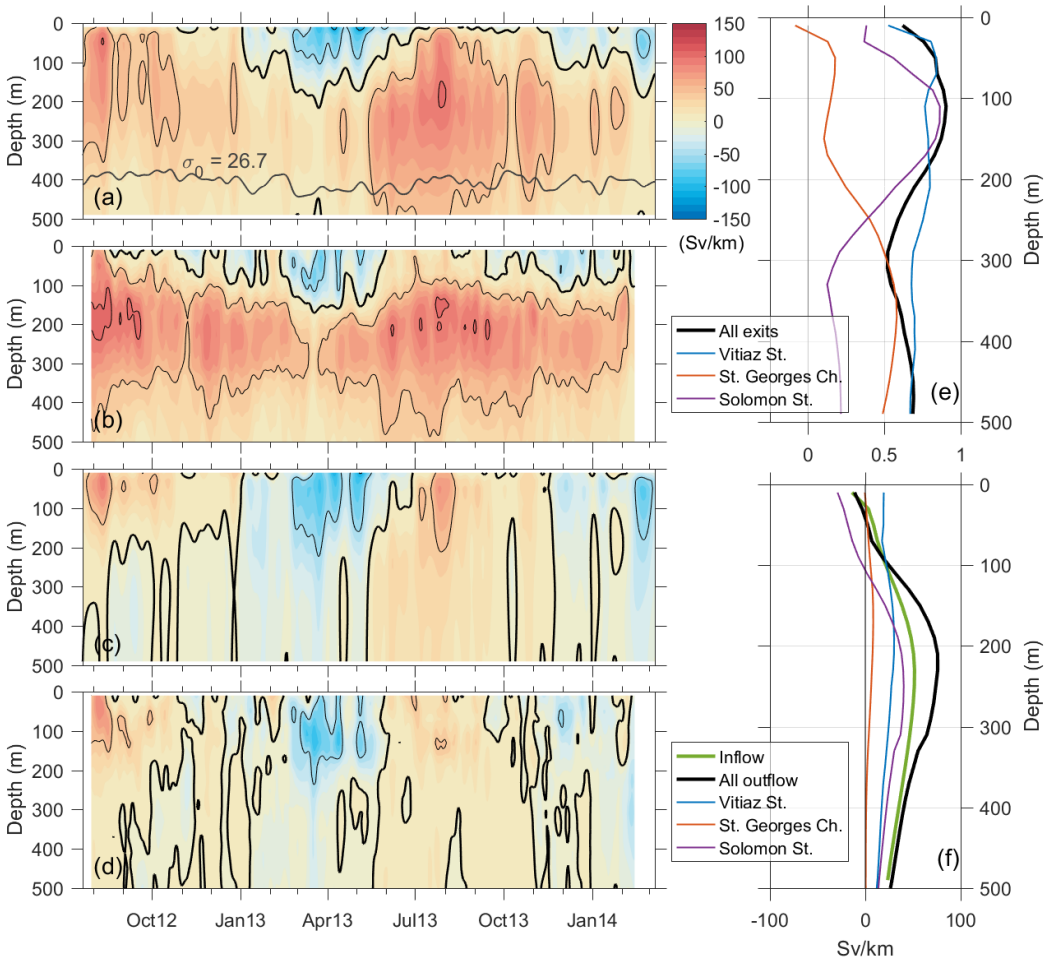

Figure 5.2: Transport per unit depth in the upper 500 m of the water column at the southern entrance (a) and the three main exits combined (b), transport per unit depth anomaly computed by removing the time-mean transport per unit depth profile from the transport per unit depth at the southern entrance (c) and the three main exits combined (d). Correlation between volume inflow per unit depth at the southern entrance and volume outflow per unit depth at Vitiaz Strait (thin blue line), St. George's Channel (thin red line), Solomon Strait (thin purple line), and all three exits combined (thick black line). Time-mean volume transports per unit depth at the southern entrance (thick black line), Vitiaz Strait (thin blue line), St. George's Channel (thin red line), Solomon Strait (thin purple line), and all three exits combined (thick black line) are shown in (f). Thick black contour indicates level of zero flow and thin black contour is plotted every 50 Sv/km.

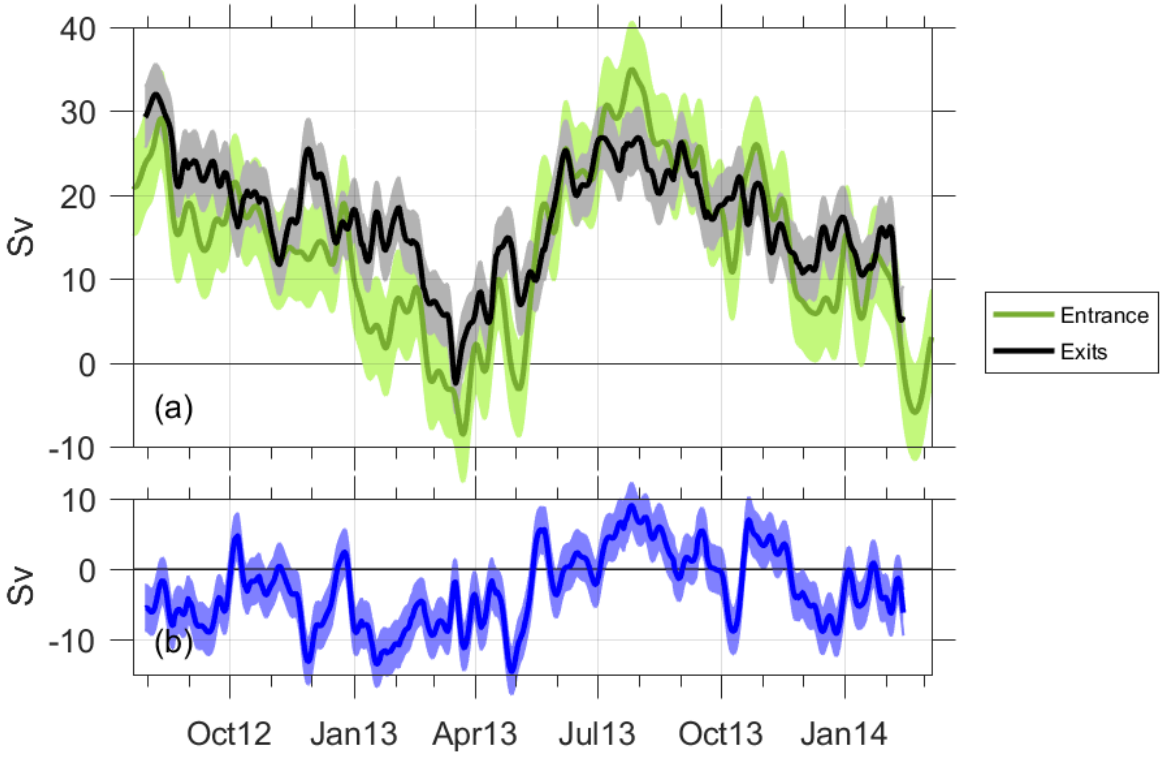

Figure 5.3: Volume transport in the surface and thermocline layer ($\sigma_\theta \leq 26.7$) observed at the Solomon Sea southern entrance (thick green) and its three main exit passages (thick black) that can be decomposed into the volume transport at Vitiaz Strait (thin blue), St. George's Channel (thin red), and Solomon Strait (thin purple) (a) with green and gray shading represents uncertainties of the estimated transport at the entrance and exits, respectively. The main-channel net inflow (southern entrance inflow minus outflows at Vitiaz Strait, St. George's Channel, and Solomon Strait) is shown in (b).

measurements were extrapolated to the surface in both locations (Anutaliya et al., 2019; Alberty et al., 2019); thus, the correlation in the upper $\sim$60 m of the water column should be interpreted with caution. The correlation between the inflow and outflow at Vitiaz Strait is the highest among the three exit channels. The high correlation reflects that a large portion of the NGCC/NGCU system in the 0-500 m depth layer that enters the Solomon Sea at its southern entrance flows equatorward along the western part of the basin and exits the Solomon Sea through Vitiaz Strait. Flow at the Solomon Strait correlates well with the inflow in the 40-220 m depth layer where $r > 0.5$; the lower correlation of $\sim$0.4 is found in the upper 40 m of the water column. Correlation between flow at Solomon Strait and that at the southern entrance reaches a maximum of 0.9 at 110-130 m implying the nearly exclusive interaction of flow variability through the Solomon Strait and the southern-entrance since there is low interaction between the inflow variability and flow through Vitiaz Strait and St. George's Channel at this depth layer. The high positive correlation in the 0-220 m depth layer suggests that the flow into the Solomon Sea at Solomon Strait, typically confined to the upper 100-200 m of the water column (Alberty et al., 2019), is closely related to the southern entrance inflow in that layer. This is consistent with previous studies (Melet et al., 2010a; Cravatte et al., 2011; Anutaliya et al., 2019) that the seasonal latitudinal migration of the South Equatorial Current (SEC) influences the flow into the Solomon Sea. The SEC migrates northward to near 3° - 6° S during March - April supplying flow into the Solomon Sea at Solomon Strait corresponding to flow into Solomon Strait (negative flow) and weakening or reversed flow at the southern entrance. During July - April, the SEC migrates southward to center near 8° - 10° S intensifying the southern entrance inflow and increasing the flow out of Solomon Strait (positive flow). Low correlation between the Solomon Sea inflow at the southern entrance and the outflow at St. George's Channel is observed with r smaller than 0.5 in the 0-300 m depth layer at zero lags. Below 300 m, the correlation with the outflow at St. George's Channel is $\sim$0.6 at zero lag. Correlation between flow through St. George's Channel and the southern entrance in the upper 60 m of the water column improves ($r = 0.5$-0.6, significant at 95% confident interval) when the

inflow leads by 8-9 months. Below 60 m depth, the correlation increases ($r = 0.4$-0.7, significant at 95% confident interval) when St. George's Channel flow leads by 1-3 months. Previous studies predicted a lead of the southern entrance as a part of St. George's Channel outflow is derived from the southern entrance inflow that turns eastward to flow along the southern coast of New Britain (Fine et al., 1994; Melet et al., 2010a). St. George's Channel outflow in the 0-100 m layer is likely dominated by inflow through the Solomon Strait (Melet et al., 2011; Alberty et al., 2019).

5.3.2 Seasonal variability

The seasonal cycle for both the inflow and the outflow is computed as a combination of annual and semiannual harmonics fitted to the volume transport in the upper layer ($\sigma_\theta \leq 26.7$) (Figure 5.4a) and volume transport per unit depth at each depth level over the analysis period of July 2012 -February 2014 (Figure 5.4b-f). Caution is needed as the seasonal cycle calculated here is derived from a relatively short time series so will not be as robust as that calculated from multiple years of measurements, e.g. see the seasonal cycles provided by Kessler et al., 2019 and Anutaliya et al., 2019 based on longer time series of transport in the Solomon Sea.

The seasonal cycle of the volume inflow explains 78% of the 0-500 m inflow variance, while that of the volume outflow explains 79% of the total outflow variance. Seasonal transport per unit depth at both the southern entrance and the three main exits combined is similar overall ($r = 0.9$) despite a stronger seasonal poleward surface flow at the entrance and a stronger subsurface equatorward flow that extends over a longer period at the exits (Figure 5.4b, c). At the southern entrance, the seasonal surface poleward flow extends to 100-170 m depth during January - mid-May with a maximum speed of 78 Sv/km in April. The seasonal maximum poleward flow at the exits is only 37 Sv/km in April and extends to a shallower depth of 70-150 m during January - mid-May. The maximum seasonal subsurface equatorward flow is 85 Sv/km and 108 Sv/km at the southern entrance and the exits, respectively. A seasonal inflow stronger than 80 Sv/km is observed during June - July at 170-270 m depth, while that of the total outflow is present from

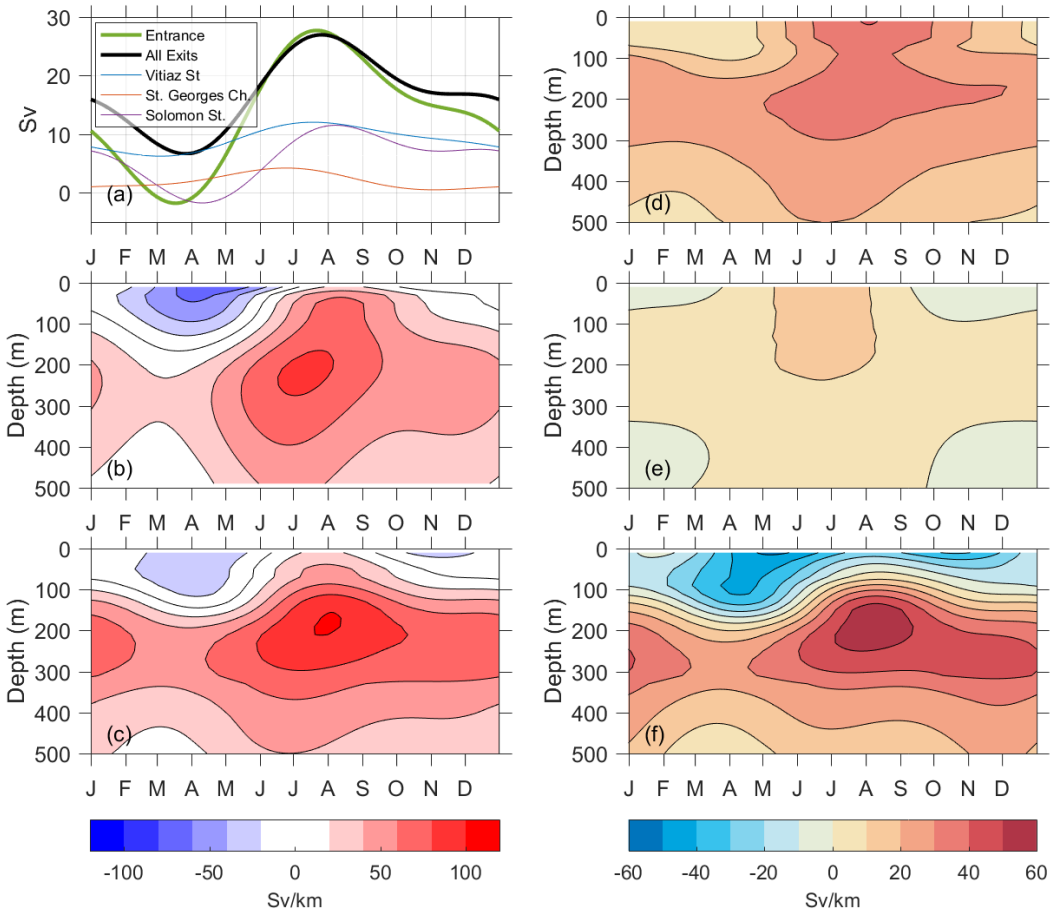

Figure 5.4: Seasonal cycle computed by fitting annual and semiannual harmonics to volume transport above $\sigma_\theta \leq 26.7$ at Solomon Sea southern entrance (thick green), its three main exits (thick black), Vitiaz Strait (thin blue), St. George's Channel (thin red), and Solomon Strait (thin purple) (a), volume transport per unit depth at the southern entrance (b), volume transport per unit depth of the three main exits combined (c), volume transport per unit depth at Vitiaz Strait (d), volume transport per unit depth at St. George's Channel (e), and volume transport per unit depth at Solomon Strait (f). Note the different color bars: that for (b) and (c) is shown in the lower left while that for (d), (e), and (f) is shown in the lower right.

mid-May to mid-December at 110-310 m depth.

Vitiaz Strait and St. George's Channel contribute 22% and 8%, respectively, to the total outflow variability on seasonal timescales (Figure 5.4). Seasonal flow over the 0-500 m depth layer in Vitiaz Strait is always equatorward with a subsurface velocity core centered at $\sim$200 m and maximum subsurface flow of 41 Sv/km in July (Figure 5.4d). Surface flow at Vitiaz Strait exhibits the highest seasonal fluctuation among the three exits and highly influences seasonal fluctuations of the total outflow in the upper 80 m of the water column (Figure 5.4c); the maximum flow reaches 54 Sv/km in August and the minimum seasonal flow is only 1 Sv/km at the end of February. At St. George's Channel, the seasonal fluctuation of the flow is similar at all depth levels; the strongest equatorward flow is observed at the end of June and the weakest flow is during October - November with flow reversal occurring over the 0-70 m and 350-500 m layers (Figure 5.4e). The strongest seasonal fluctuation at St. George's Channel is at the surface, ranging from -9 to 16 Sv/km. Seasonal fluctuation of flow at the Solomon Strait contributes 70% to the seasonal total outflow variance and most closely resembles that of the total outflow below 100 m depth (Figure 5.4c, f). At Solomon Strait, the seasonal surface flow is almost always poleward into the Solomon Sea (Figure 5.5f). The subsurface equatorward transport extends from 60-180 m depth to the deepest analyzed depth of 500 m with the maximum subsurface transport per unit depth of 56 Sv/km, slightly more than half of the maximum subsurface seasonal total outflow. The similarity between the seasonal cycle at the Solomon Sea southern entrance and that of the outflow through Solomon Strait indicates a strong interaction on the seasonal timescales.

5.4 Solomon sea volume transport from numerical simulation (POP/CICE)

Velocity and density fields from POP are examined to further understand the relationship between the inflow and outflow of the Solomon Sea, particularly to investigate factors that

contribute to the difference between the observed mean upper layer volume transport over the overlapping July 2012 - February 2014 period at the southern entrance and the exits (Figure 5.3; Section 5.3.1).

5.4.1 Comparison between POP volume transport and the observations

Time-mean velocity at the exits

Although mooring observations and model outputs were observed/ simulated over different time periods, the across-transect velocity exhibits similar overall time-mean velocity structure; the depth of the maximum mean velocity cores from POP and the observations compares well at all three exits (Figure 5.5). At Vitiaz Strait, the POP mean maximum equatorward velocity is 1.3 m/s and that from the observations is 1.0 m/s (Figure 5.5a, d). POP shows a velocity core in Vitiaz Strait located in the middle of the channel; however that from the mooring observations intensifies toward the western boundary as shown by previous observations (Cravatte et al, 2011; Germineaud et al., 2016; Alberty et al., 2019) and a high-resolution regional numerical simulation (Djath et al., 2014). As POP's horizontal resolution is $\sim$11 km in the Solomon Sea region, the POP bathymetry cannot precisely resolve the deep and narrow terrain in St. Georges Channel. Instead, St. George's Channel that is only $\sim$17 km wide in reality is configured to be $\sim$22 km wide (two velocity grid cells over the full channel depth) and only 465 m deep which is much shallower than the real sill depth of 1400 m. Flow at St. Georges Channel is much weaker in POP with a maximum mean subsurface velocity of 0.3 m/s compared to the observed value of 0.7 m/s (Figure 5.5b, e). This difference is likely the result of the bathymetry limitations in the model. At Solomon Strait, the observed and simulated mean velocities are very similar and their maximum mean velocities of the surface poleward core and subsurface equatorward core (centered at $\sim$250 m depth) in the western part of the channel (63 km within the western boundary) are comparable (Figure 5.5c, f). POP's subsurface poleward flow below $\sim$900 m depth is also similar to the

observations despite a stronger velocity core located at $\sim$ 1600 m. In the eastern part of the Solomon Strait, velocity is generally small in both observations and the model.

Fluctuation of volume transport and volume transport per unit depth

POP volume transport per unit depth shows a clear seasonal cycle at both the entrance and the exits with subsurface equatorward flow that intensifies during June - July and weakens during February - March (Figure 5.6a, b) in good agreement with the mooring observations (Figure 5.2a, b). POP also shows the stronger subsurface flow at the exits compared to that at the southern entrance, consistent with the observations. At the exits, surface poleward flow in POP often extends over a longer period usually covering most months except June and July compared to that at the entrance that only extends from January to May; this difference in time span of the surface poleward flow is not clear in the observations that only cover a 19 month period. The longer duration of the surface poleward current at the exits compensates the intensified subsurface outflow giving a model mean upper layer volume transport of 17.6 Sv similar to that at the southern entrance of 17.4 Sv (Table 5.1). Flow at the southern entrance ranges from -2.9 to 36.7 Sv and that at the exits ranges from -7.0 to 37.0 Sv in POP (Figure 5.6c), comparable to the range of the inflow and outflow observed by the moorings (Figure 5.3a).

Distribution of the mean outflow among the main exits in POP is quite different from those of the observations. The mean POP outflow at Vitiaz Strait is 12.4 Sv and so higher than the mooring estimation of 9.1 Sv (Figure 5.6a, d; Table 5.1). At Solomon Strait, the mean POP flow is 2.5 Sv smaller than that of the mooring observations, although flow at Solomon Strait from both observations and POP show a similar range in volume transport. As the mooring measurements are over the period of July 2012 - February 2014, it includes two seasons of intensified equatorward flow in July - August but only one season of weak flow or flow reversal in March - April. This likely causes the lower mean transport at Solomon Strait. Mean upper-layer volume transport at St. George's Channel estimated from POP is slightly lower than that from

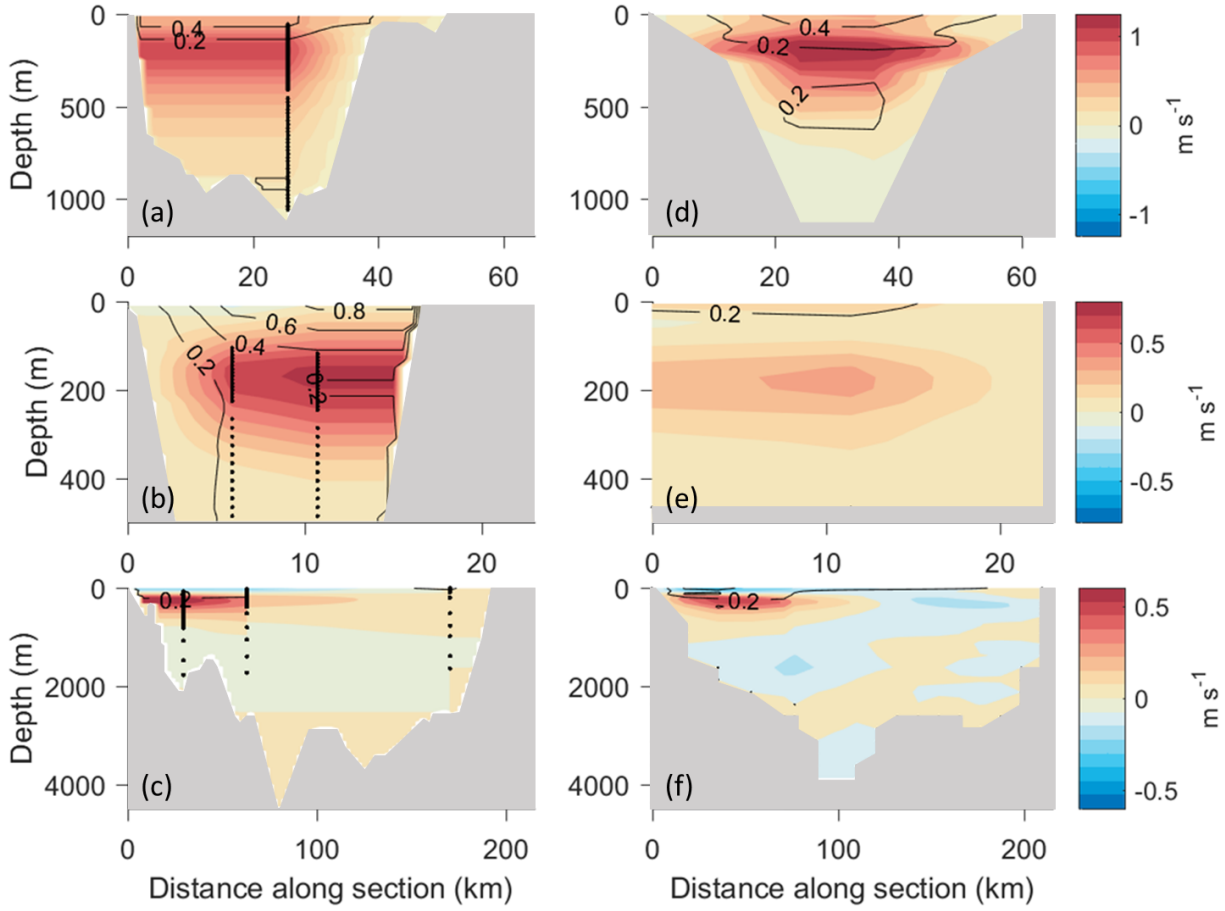

Figure 5.5: Time-mean velocity over the July 2012 - February 2014 period from the outflow mooring observations (a-c) and that over 2005 - 2009 period from POP (d-f) at Vitiaz Strait (a, d), St. George's Channel (b, e), and at Solomon Strait (c, f). Color bar for each channel is present on the right and the width of each channel (x-axis) is different. Note that only the upper 500 m of velocity at St. George's Channel is shown as the channel is only 465 m deep in POP. Thick black contour indicates level of zero flow and thin black contour is plotted every 0.3 m/s, while black dots represent the mean location of mooring measurements.

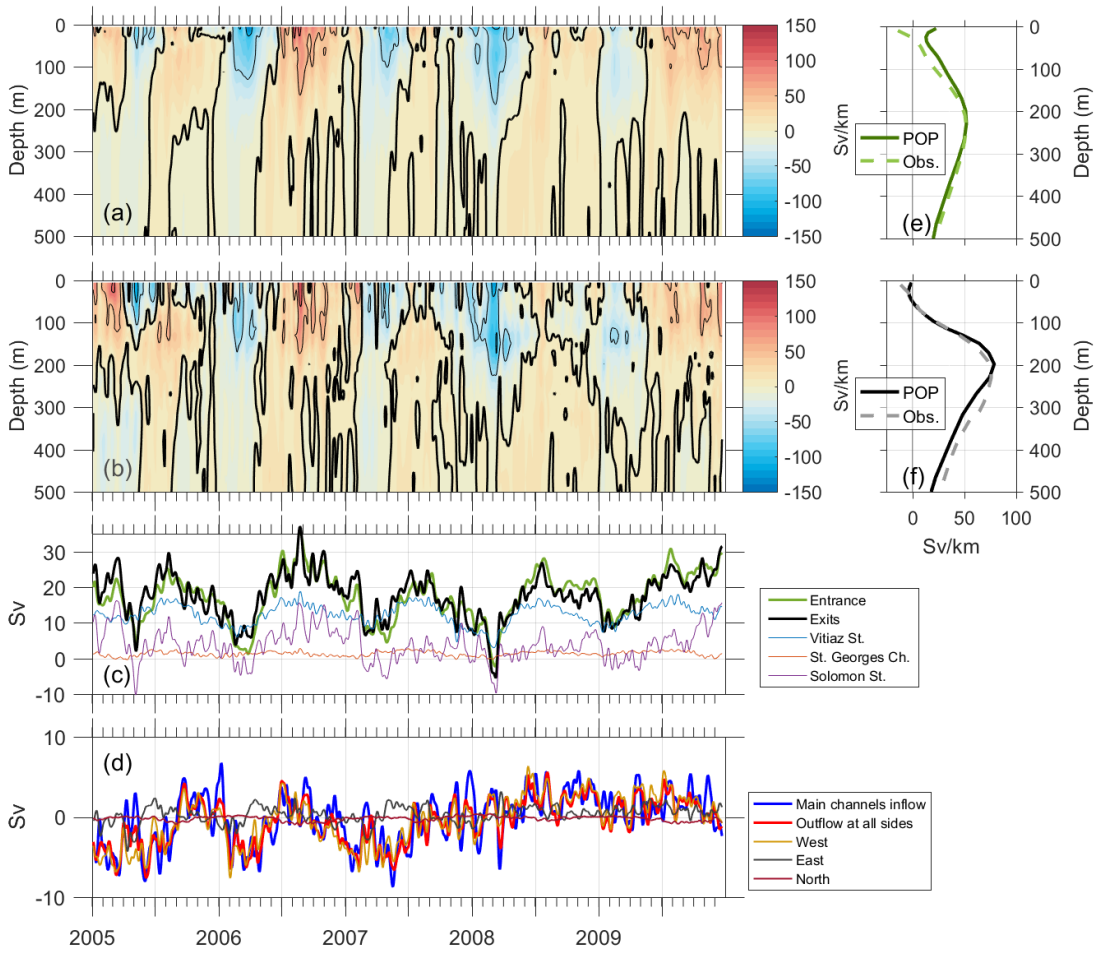

Figure 5.6: Volume transport per unit depth anomaly (time-mean transport profile removed) simulated by POP at the Solomon Sea southern entrance (a) and all three main exits combined (b), volume transport in the surface and thermocline layer ($\sigma_\theta \leq 26.7$) (c) at the entrance (thick green), three main exits combined (thick black), Vitiaz Strait (thin blue), St. George's Channel (thin red), and Solomon Strait (thin purple), and the comparison between net volume inflow at the main channels (thick blue; inflow at the southern entrance minus outflows at the three main exit passages) and outflow at the side channels (thick red) decomposed into outflow at the west site/ Jomard Channel (thin yellow), east site (thin gray), and north site (thin maroon) (d). 2005-2009 mean volume transport per unit depth of the inflow and outflow is shown in (e) and (f) (solid lines) along with the observed mean profile (dashed lines). Thick black contour in (a) and (b) indicates level of zero flow and thin black contour is plotted every 50 Sv/km.

the observations. Volume transport fluctuation at St. George's Channel estimated by POP is also somewhat smaller with a range of -0.6 to 3.0 Sv compared to the observed that ranges from -1.3 to 5.8 Sv. The discrepancy is likely a consequence of coarse model resolution that cannot fully resolve flow through such a deep and narrow channel, such as St. George's Channel.

Even though the horizontal resolution of POP is quite coarse for providing a detailed depiction of the circulation in the Solomon Sea, the comparison with observations show that the POP velocity field remarkably captures much of the main circulation in this region. In addition, the POP velocity fields allow for an examination of the Solomon Sea circulation in the layer below 500 m as well as in the regions not occupied by the moorings, such as that occurs west of Misima Island, Papua New Guinea, where the western inflow mooring is located, as well as between the Solomon Island chain (Figure 5.1). Therefore, POP velocity and density fields are analyzed in the following to understand the cause of the apparent mismatch between the observed inflow and outflow time series.

5.4.2 POP volume inflow and outflow

In the surface and thermocline layer, model temporal fluctuations of both the Solomon Sea inflow and outflow at the main exits are similar; $r = 0.9$ with no time lag (Figure 5.6). The difference between the inflow and total outflow ranges from -8.7 to 6.7 Sv around a mean value of 0.16 Sv (Figure 5.6d; Table 5.1). Seasonal variability of the main-channel net inflow, defined as inflow at the southern entrance minus outflow at the three main exits, is apparent from 2005 to 2007; low net inflow is observed in approximately the first half of the years while high net inflow is present in the second half. The majority of the main-channel net inflow fluctuation is captured by fluctuation of the flows at the sides of the Solomon Sea, which are located to the west of Misima through Jomard Channel (west site), between the Solomon Island chain (east site), and to the east of Vitiaz Strait mooring (north site) (Figure 5.1), with a correlation of 0.8 (Figure 5.6d). Mean flows at the west, east, and north sites are 0.42, 0.31, and 0.20 Sv toward the equator,

respectively. This yields the total upper-layer 2005-2009 mean flow of 0.53 Sv into the Solomon Sea from all the sides and implies a mean across-isopycnal flow of 0.39 Sv. At the sides, flow ranges from -5.6 to 7.6 Sv and is largely dominated by flow through Jomard Channel (Figure 1) ranging from -6.3 to 7.6 Sv (Figure 5.6d).

Flow through Jomard Channel (185 km wide with the sill depth of 1250 m and configured in POP to be 180 km wide with the sill depth of 1140 m) is highly fluctuating, so it is important to identify if the low-frequency component of the transport through this passage can contribute to the time-mean difference in the observed volume transport. POP indicates that the mean flow through Jomard Channel in the upper 80 m of the water column is poleward out of the Solomon Sea intensified on the western side of the channel (Figure 5.7a). Below 80 m depth, the flow reverses to be equatorward with a maximum mean flow of 0.4 m/s at 230 m depth, also in the western side of the channel; the depth of the subsurface maximum velocity core is similar to that at the southern entrance (Figure 5.2f, 5.6e). Across-channel velocity through Jomard Channel shows high standard deviation in the upper 200 m of the water column and is with in $\sim$130 km of the western boundary (Figure 5.7b). To examine whether flow through Jomard Channel can contribute to the difference in the time-mean observed at the entrance and exits (Figure 5.2, 5.3), a 19-month (length of the observing period) moving average is applied to the upper layer volume transport at Jomard Channel; the low-frequency flow ranges from -2.8 to 1.8 Sv (Figure 5.8a).

As the correlation between the upper layer flow through Jomard channel and the across-transect mean geostrophic velocity from POP sea surface height is high ($r = 0.84$; Figure 5.8a), sea surface height can be used as a proxy for volume transport in the upper layer. Correlation between along-track sea surface height from the Jason-1 mission over 2005-2009 period, and POP sea surface height is 0.59 and 0.53 at the end points of the transect across Jomard Channel. Along-track sea surface height near Misima Island also compares well with direct measurement sea level anomaly from Misima mooring/PIES over July 2012 - May 2016 period ($r = 0.65$). Thus, satellite along-track sea surface height from the Jason-1 and Jason-2 missions (track locations

shown in Figure 5.1) available from January 2005 to May 2016 is used to estimate a proxy for the transport anomaly; the proxy ranges from -5.1 to 8.8 Sv (Figure 5.8b). A 19-month moving average of the proxy (time-mean of the proxy is zero) suggests that flow through Jomard Channel can contribute -1.1 to 0.8 Sv to a time-mean flow into the Solomon Sea over a 19-month period. No distinct seasonal fluctuation is observed in the 2005-2016 proxy of the transport anomaly (Figure 5.8).

5.5 Summary

Independent measurements of volume transport in the upper layer ($\sigma_\theta \leq 26.7$) at the southern entrance and at the exits of the Solomon Sea show similar fluctuations with no significant time lag (Figure 5.2, 5.3). At the seasonal timescale, the outflow variability is highly dominated by the seasonal fluctuation at Solomon Strait highlighting strong seasonal interaction between the inflow and flow through Solomon Strait (Figure 5.4). Although mean volume inflow over the observing period is smaller than the mean outflow (Table 5.1), numerical simulation and satellite along-track sea surface height suggest that inflow through the unmeasured Jomard Channel can contribute to the mean flow (Figure 5.8). As the numerical simulation suggests that fluctuation of flow through Jomard Channel is $\sim$10 Sv, measurement of the LLWBC contribution through Jomard Channel would be valuable to gain a better understanding of the circulation in the Solomon Sea, particularly at short timescales.

Many questions regarding the relationship between the Solomon Sea inflow and outflows remain to be addressed by future studies. What are the forcing mechanisms that influence the flow variability at each exit and are they related to the westward-propagating Rossby waves from the interior of the Pacific Ocean that influence seasonal and interannual variability at the southern entrance (Anutaliya et al., 2019)? A longer observation of the outflow would also be necessary to understand the interannual variation at each exit passage to understand how the intensified

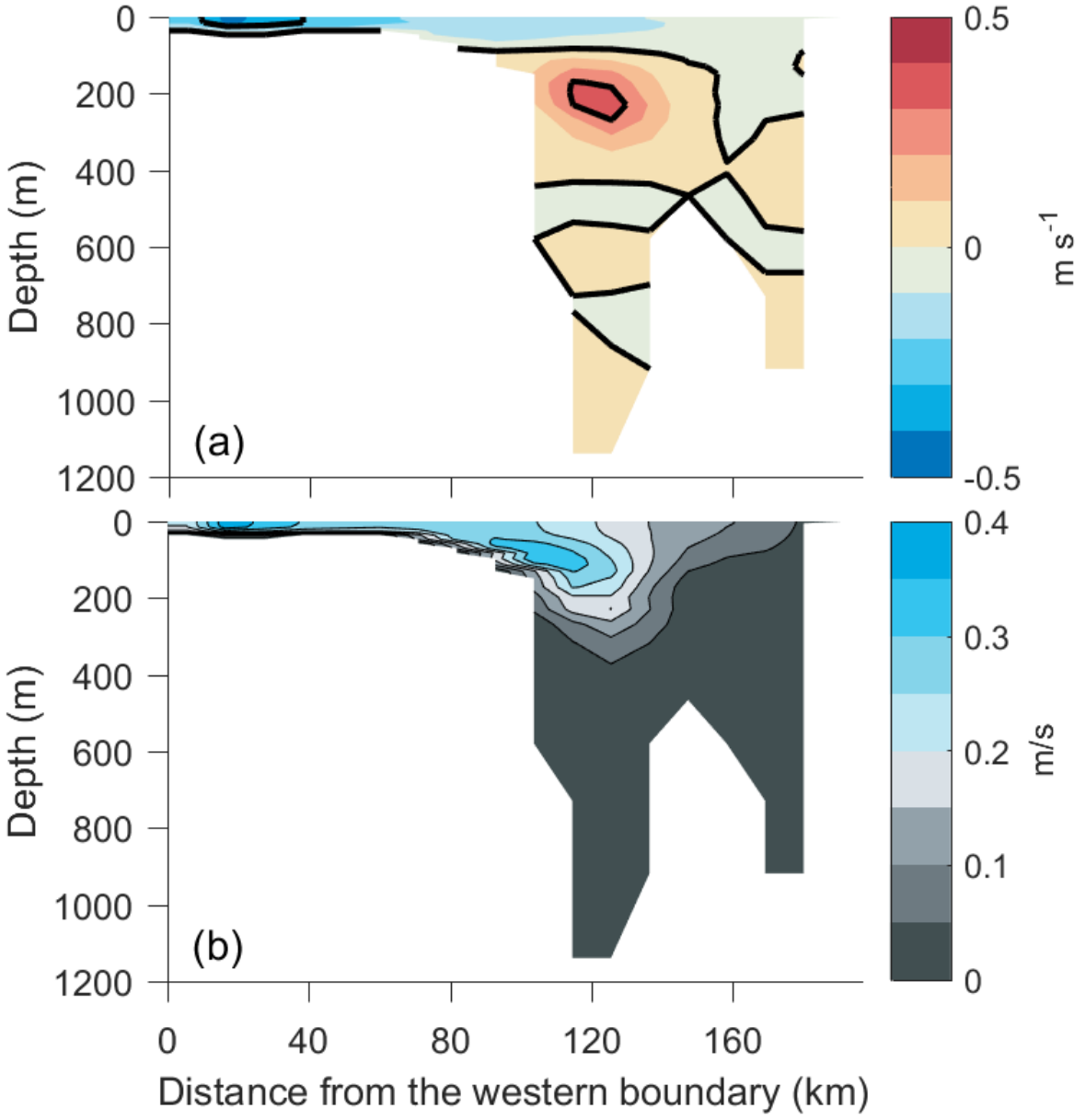

Figure 5.7: Mean (a) and standard deviation (b) of 2005-2009 POP velocity (m/s) through Jomard Channel (Figure 5.1). Thick black contour in (a) is plotted every 0.3 m/s.

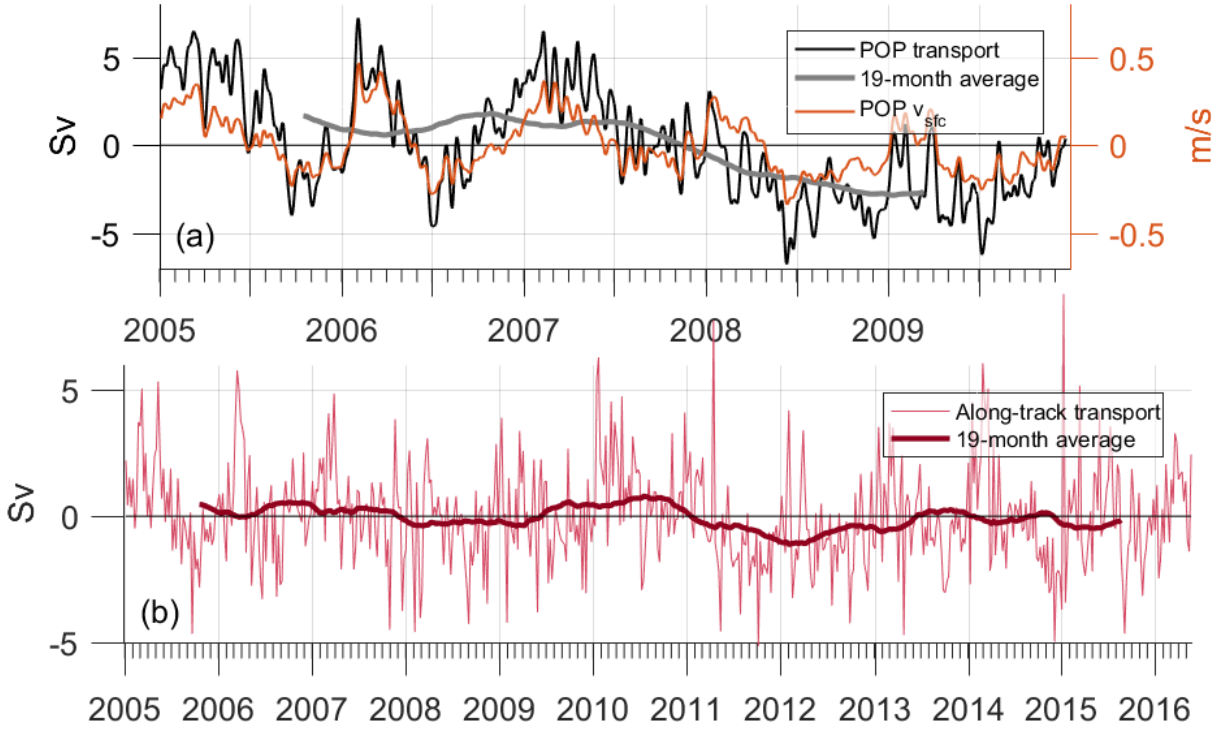

Figure 5.8: Across-transect mean surface geostrophic velocity (m/s) (orange), volume transport (Sv) in the upper layer (black) and its 19-month moving average (thick gray) at Jomard Channel simulated from POP (a), and the upper layer volume transport proxy from satellite along-track sea surface height based on empirical relationship from POP outputs (thin pink) and 19-month moving average of the proxy (thick maroon) (b).

(weakened) equatorward inflow (Davis et al., 2012; Zilberman et al., 2013; Anutaliya et al., 2019) distributes among the exit passages during El Niño (La Niña) conditions.

5.6 Acknowledgement

This material is based upon work supported by the National Aeronautics and Space Administration under Grant Number 80NSSC17K0373 to Arachaporn Anutaliya. Any opinions,findings, and conclusions or recommendations expressed in this material are those of the author(s) and do not necessarily reflect the views of the National Aeronautics and Space Administration. Julie L. McClean was supported by Department of Energy/Office of Science grant DE-SC0012778. CCMP Version-2.0 vector wind analyses are produced by Remote Sensing Systems. Data are available at www.remss.com. This study has been conducted using E.U. Copernicus Marine Service Information (http://marine.copernicus.eu/services-portfolio/access-to-products/?option=com_csw&view=details&product_id=SEALEVEL_GLO_PHY_L3_REP_OBSERVATIONS_008_062).

Chapter 5 is a draft of manuscript in preparation for submission as ”Observations of the Solomon Sea inflow and outflow”, by A. Anutaliya, U. Send, J. Sprintall, and J. L. McClean. The dissertation author was the primary investigator and author of this work.

Chapter 6

Conclusions

In this thesis, the variability of low latitude boundary currents in the Bay of Bengal (BoB) and the south Pacific Ocean are examined.

Chapter 2 discusses a new technique that is successfully developed to extract volume transport along the eastern and southern coasts of Sri Lanka from the continuous bottom pressure and acoustic travel time measurements from Pressure sensing Inverted Echo Sounders (PIES). The volume transport in the 0-200 m depth layer along the eastern (southern) Sri Lankan coasts reverses its direction semiannually (annually). The boundary currents in the 0-200 m depth layer play an important role in balancing the salinity in the Bay of Bengal (BoB), particularly during the northeast monsoon when the southward-flowing East Indian Coastal Current intensifies and extends to flow along the Sri Lankan eastern coast and then turns westward to flow along the southern coasts. During the fall monsoon transition of some years, the boundary currents also transport saline water originating in the central or western equatorial Arabian Sea into the BoB. The eddy salt flux calculated in Chapter 2 is inferred from PIES-based volume transport in combination with historical hydrography and a satellite sea surface salinity (SSS) product. Unfortunately, the satellite SSS provides no viable measurements within 40 km of the coast due to land contamination (Grodsky et al., 2018). Thus, the eddy salt flux presented in this study is

likely underestimated as the SSS is extrapolated to the coast as a constant while a few near-coast glider measurements show that SSS sometime intensifies toward the coasts during these high salt flux seasons. With direct measurements of salinity with in 40 km of the Sri Lankan coastline (such as from near-coast salinity mooring measurements), more accurate eddy salt flux estimation could be achieved.

Chapter 3 made use of glider measurements, historical hydrography, and numerical simulations to reveal the presence of an undercurrent along the eastern coast of Sri Lanka flowing in the opposite direction to the surface current, particularly during the spring monsoon transition and summer monsoon. Evidence from previous mooring observations along the eastern coast of India (Mukherjee et al., 2014) and southern coasts of Sri Lanka (Schott et al., 1994) also observe the reversing subsurface flow suggesting a subsurface pathway that connects the two basins of the northern Indian Ocean. Still the first-order estimation of salt flux associated with the undercurrent is small and further study is needed to obtain a better understanding of the role of the undercurrent on inter-basin salt/freshwater exchange.

Observations over approximately five years of the New Guinea Coastal Current/New Guinea Coastal Undercurrent (NGCC/NGCU), the LLWBC of the Solomon Sea located in the southwestern Pacific Ocean, are examined in Chapter 4. High-frequency continuous observations using PIES and end-point moorings show highly fluctuating flow in the upper 500 m of the water column at subseasonal, seasonal, and interannual timescales. While the local and remote winds partly influence the subseasonal variability, westward-propagating Rossby waves originating in the interior of the Pacific Ocean highly influence the variability at seasonal and interannual timescales. During the 2015/2016 El Niño, the NGCC/NGCU strengthens and the seasonal cycle is suppressed. In addition, 25 years of proxy volume transport based on gridded satellite absolute dynamic topography is developed. The proxy shows high correlation between the volume transport anomaly, calculated by removing the seasonal cycle and filtering signals to remove frequencies higher than 400 days, and mean surface temperature in the Niño 3.4 region in the

central equatorial Pacific Ocean (5° S to 5° N latitude and 170° W to 120° W longitude). The proxy transport suggests intensified equatorward flow of the NGCC/NGCU and a weakened seasonal cycle during El Niño conditions while the equatorward flow weakens and its seasonal cycle becomes more pronounced during La Niña conditions.

Chapter 5 exploits the simultaneous measurements of continuous flow into and out of the Solomon Sea over a 19-month period as well as five-year outputs from a global coupled Parallel Ocean Program/ Los Alamos Sea Ice Model (POP/ CICE) simulation to examine the relationship between the Solomon Sea inflow and outflow. The measurements show high correlation between flow into the Solomon Sea and that at its main exit passages at zero lag. High correlation between the inflow and outflow at Vitiaz Strait is observed over all depth layers in the upper 500 m of the water column suggesting that the majority of the southern entrance inflow exits the Solomon Sea at Vitiaz Strait. At seasonal timescales, the southern-entrance inflow fluctuation highly covaries with flow at Solomon Strait. Above the $\sigma_\theta = 26.7$ isopycnal, mean volume transport of the inflow over the observing period is somewhat lower than that of the outflow. POP velocity fields and satellite along-track-derived sea surface height suggest that the mismatch between the 19-month time-mean volume inflow and outflow is likely contributed by highly-fluctuating flow through Jomard Channel that is not accounted for by the measurements. Further work can be carried out to gain a better understanding of the relationship between the inflow and outflows, for example to examine mechanisms dominating the variability at each exit and how that may be influenced by interannual ENSO signals. Are the mechanisms influencing the inflow variability (e.g. local and remote winds and westward-propagating Rossby waves originated in the interior of the Pacific Ocean) similar or different to those influencing the outflow? Longer observations of the outflows would be of benefit in obtaining a better understanding of the interannual outflow variability which is valuable in understanding the mass and heat recharge/discharge associated with El NiñoSouthern Oscillation.

Appendix A

Numerical model: Chapter 4

A global strongly eddy active Ocean General Circulation Model (OGCM), the 0.1° Parallel Ocean Program coupled to the Los Alamos Sea Ice Model (POP/ CICE) run in the Community Earth System Model (CESM) framework (McClean et al., 2018), was used to estimate uncertainty associated with volume transport derived from mooring/PIES measurements. POP is a three-dimensional, z-level, primitive equation model (Dukowicz & Smith, 1994). It was configured on a global tripole grid with 42 vertical levels and partial bottom cells. It is forced with Co-ordinated Ocean-ice Reference Experiments II (CORE-II) interannually-varying atmospheric surface fluxes (Large & Yeager, 2009) and run from 1948-2009. POP's horizontal resolution corresponds to approximately 11 km in the Solomon Sea. The POP output analyzed here consists of three-dimensional daily-averaged velocity and density fields for 2005-2009.

Appendix B

Estimating error in volume transport calculation due to eddies: Chapter 4

Assuming a constant f and no cross-passage structure along the entire transect between the two end-point moorings can result in an error in our volume transport calculation, particularly during times when eddies propagate across the transect. Therefore, we estimated uncertainty in our calculation arising from across-transect eddy propagation as an artifact of these assumptions. We identified eddies manually from a satellite SLA field as a closed SLA contour with a minimum or maximum vertical displacement exceeding 10 cm. For each eddy, the uncertainty (V_e, shown in Figure 4.5b) was estimated as the difference between that representing the mooring (V_{moor}) and the "more resolved" volume transport (V_{res}). Only the end-point SLA and a constant f ($f_{mid} = f$ at 9.4° S) were used to calculate V_{moor}, while all available SLA along the transect binned into 0.12° bin (corresponding to ∼0.06° latitude) and f parameter at the center of each bin (f_i) were used to compute V_{res}. Both V_{moor} and V_{res} were estimated at each daily time step (t):

$$V_{moor}(t) = \frac{gD}{f_{mid}}(\eta_{n+1}(t) - \eta_1(t)), \tag{B.1}$$

$$V_{res}(t) = \sum_{i=1}^{n} \frac{gD}{f_i}\Delta\eta_i(t) \tag{B.2}$$

$$V_e(t) = V_{moor}(t) - V_{res}(t) \tag{B.3}$$

Where D is a constant depth layer of 500 m, η is SLA at the western side of bin i at time step t, n represents the number of bins along the transect (equal to 40), and $\Delta\eta$ is the SLA difference between the eastern and western side of bin.

Bibliography

Alberty, M. S. (2018), Water Mass Transport and Transformation in the Tropics and Arctic, (Doctoral dissertation). Retrieved from eScholarship. (https://escholarship.org/uc/item/9rf158pq). San Diego, CA: University of California San Diego.

Alberty, M., J. Sprintall, J. MacKinnon, C. Germineaud, S. Cravatte, S., and A. Ganachaud (2019), Moored Observations of Transport in the Solomon Sea, J. Geophys. Res. Oceans, doi:10.1029/2019JC015143

Anutaliya, A., U. Send, J. L. McClean, J. Sprintall, L. Rainville, C. M. Lee, S. U. P. Jinadasa, A. J. Wallcraft, and E. J. Metzger (2017), An undercurrent off the east coast of Sri Lanka. Ocean Sci., 13, 1035-1044, doi:10.5194/os-13-1035-2017

Anutaliya, A., U. Send, J. Sprintall, J. L. McClean, M. Lankhorst, and J. Koelling (2019), Mooring and seafloor pressure end point measurements at the southern entrance of the Solomon Sea: Subseasonal to interannual flow variability. J. Geophys. Res. Ocean, 124, 5085-5104, doi:10.1029/2019JC015157

Butt, J. and E. Lindstrom (1994), Currents off the east coast of New Ireland, Papua New Guinea, and their relevance to regional undercurrents in the western equatorial Pacific Ocean. J. Geophys. Res., 99, 12503-12514

Byrne D. A. (2000), From the Agulhas to the South Atlantic: Measuring Inter-ocean Fluxes, (Doctoral dissertation). Retrieved from bookpump (http://www.bookpump.com/dps/pdf-b/1121040b.pdf). New York, NY: Columbia University.

Chaitanya, A. V. S., F. Durand, S. Mathew, V. V. Gopalakrishna, F. Papa, M. Lengaigne, J. Vialard, C. Kranthikumar, and R. Venkatesan (2014), Observed year-to-year sea surface salinity variability in the Bay of Bengal during the 2009-2014 period. Ocean Dynam., 65, 173-186, doi:10.1007/s10236-014-0802-x

Chelton, D. B., R. A. deSzoeke, M. G. Schlax, K. El Naggar, and N. Siwertz (1998), Geographical variability of the first-baroclinic Rossby radius of deformation. J. Phys. Oceanogr., 28, 433-460.

Chen, S., and B. Qiu (2004). Seasonal variability of the South Equatorial Countercurrent. J. Geophys. Res., 109, C08003. doi:10.1029/2003JC002243

Codiga, D. L. (2011), Unified Tidal Analysis and Prediction Using the UTide Matlab Functions (Technical Report 2011-01). Graduate School of Oceanography, University of Rhode Island, Narragansett, RI. ftp://www.po.gso.uri.edu/pub/downloads/codiga/pubs/2011Codiga-UTide-Report.pdf

Cravatte, S., A. Ganachaud, Q-P. Duong, W. S. Kessler, G. Eldin, and P. Dutrieux (2011), Observed circulation in the Solomon Sea from SADCP. Progr. in Oceanogr., 88, 116-130, doi: 10.1016/j.pocean.2010.12.015

Cutler, A. N., and J. C. Swallow (1984), Surface currents of the Indian Ocean (to 25°S, 100°E). IOS Tech. Rep., 187, Inst. Of Oceanogr. Sci., Wormley, England.

D'Addezio, J. M., B. Subrahmanyam, E. S. Nyadjro, and V. S. N. Murty (2015), Seasonal Variability of Salinity and Salt Transport in the Northern Indian Ocean. J. Phys. Res., 45, 1947-1966. doi:10.1175/JPO-D-14-0210.1

Dandapat, S., A. Chakraborty, J. Kuttippurath (2018), Dipole events using a high resolution regional ocean model. Ocean Dynam.,68(10), 1321-1334.

Davis, S. E., W. S. Kessler, and J. T. Sherman (2013), Gliders Measure Western Boundary Current Transport from the South Pacific to the Equator. J. Phys. Oceanogr., 42, 2001-2013. doi: 10.1175/JPO-D-12-022.1

de Vos, A., C. B. Pattiaratchi, and E. M. S. Wijeratne (2014), Surface circulation and upwelling patterns around Sri Lanka. Biogeosciences, 11, 5905-5930. doi:10.5194/bg-11-5909-2014

Djath, B., J. Verron, A. Melet, L. Gourdeau, B. Barnier, and J-M Molines (2014), Multiscale dynamical analysis of a high-resolution numerical model simulation of the Solomon Sea Circulation. J Geophys. Res. Oceans, 119, 6286-6304. doi:10.1002/2013JC009695

Donguy, J., and G. Meyers (1996), Seasonal variations of sea-surface salinity and temperature in the tropical Indian Ocean. Deep Sea Res., Part I, 43(2), 117-138.

Ducet, N., P. Y. L. Traon, and G. Reverdin (2000), Global high-resolution mapping of ocean circulation from TOPEX/Poseidon and ERS-1 and -2. J. Geophys. Res., 105, 19477-19498.

Dukowicz, J. K., and R. D. Smith (1994), Implicit free-surface method for the Bryan-Cox-Semtner ocean model. J. Geophys. Res., 99, 7991-8014.

Durand, F., D. Shankar, F. Birol, and S. S. C. Shenoi (2009), Spatiotemporal structure of the East India Coastal Current from satellite altimetry. J. Geophys. Res., 114, C02013, doi:10.1029/2008JC004807.

Durand, F., F. Papa, A. Rahman, S. K. Bala (2011), Impact of Ganges-Brahmaputra interannual discharge variations on Bay of Bengal salinity and temperature during 1992-1999 period. J. Earth Syst. Sci., 120, 859-872.

Eigenheer, A., and D. Quadfasel (2002), Seasonal variability of the Bay of Bengal circulation inferred from TOPEX/Poseidon altimetry. J. Geophys. Res., 105, 3243-3252, doi:10.1029/1999JC900291

Fine, R. A., R. Lukas, F. M. Bingham, M. J. Warner, and R. H. Gammon (1994), The western equatorial pacific: A water mass crossroads. J. Geophys. Res., 99(C12), 25063-25080. doi: 10.10.29/94JC02277

Ganachaud, A., S. Cravatte, A. Melet, A. Schiller, N. J. Holbrook, B. M. Sloyan, et al. (2014), The Southwest Pacific Ocean circulation and climate experiment (SPICE). J. Geophys. Res. Oceans, 119, 7660-7686. doi:10.1002/2013JC009678

Ganachaud, A., S. Cravatte, J. Sprintall, C. Germineaud, M. S. Alberty, C. Jeandel, et al. (2017), The Solomon Sea: its circulation, chemistry, geochemistry and biology explored during two oceanographic cruises. Elem. Sci. Anth., 5, 33. doi: 10.1525/elementa.221

Gasparin, F., A. Ganachaud, C. Maes, F. Marin, and G. Eldin (2012), Oceanic transports through the Solomon Sea: The bend of the New Guinea Coastal Undercurrent. Geophys. Res. Lett., 39, L15608. doi:10.1029/2012GL052575

Germineaud, C., A. Ganachaud, J. Sprintall, S. Cravatte, G. Eldin, M. S. Alberty, and E. Privat (2016), Pathways and Water Properties of the Thermocline and Intermediate Water in the Solomon Sea. J. Phys. Oceanogr., 46, 3031-3049. doi:10.1175/JPO-D-16-0107.1

Grodsky, S. A., D. Vandemark, and H. Feng (2018), Assessing Coastal SMAP Surface Salinity Accuracy and Its Application to Monitoring Gulf of Maine Circulation Dynamics. Remote Sens., 10(8), 1232, doi:10.3390/rs10081232

Gourdeau, L., J. Verron, A. Melet, W. Kessler, F. Marin, and B. Djath (2014), Exploring the mesoscale activity in the Solomon Sea: A complementary approach with a numerical model and altimetric data. J. Geophys. Res. Oceans, 119, 2290-2311, doi:10.1002/2013JC009614

Gourdeau, L., J. Verron, A. Chaigneau, S. Cravatte, and W. Kessler (2017), Complementary Use of Glider Data, Altimetry, and Model for Exploring Mesoscale Eddies in the Tropical Pacific Solomon Sea. J. Geophys. Res. Ocean, 122, 9209-9229, doi:10.1002/2017JC013116

Grenier, M., S. Cravatte, B. Blanke, C. Menkes, A. Koch-Larrouy, R. Durand, A. Melet, and C. Jeandel (2011), From the western boundary currents to the pacific equatorial undercurrent: Modeled pathways and water mass evolutions. J. Geophys. Res., 116, C12044, doi:10.1029/2011JC007477

Gu, D. F., and S. G. H. Philander (1997), Interdecadal climate fluctuations that depend on exchanges between the tropics and extratropics. Science, 275, 805-807.

Hacker, P., E. Firing, and J. Hummon (1998), Bay of Bengal currents during the northeast monsoon. Geophys. Res. Lett., 25(15), 2,769-2,772, doi:10.1029/98GL52115

Han, W., and J. P. McCreary (2001), Modelling salinity distributions in the Indian Ocean, J. Geophys. Res., 106, 859-877.

Harrison, D. E., & N. K. Larkin (1996), The COADS Sea Level Pressure Signal: A Near-Global El Niño Composite and Time Series View, 1946-1993. J. Clim., 9(12), 3025-3055.

Holgate, S. J., A. Matthews, P. L. Woodworth, L. J. Rickards, M. E. Tamisiea, E. Bradshaw, E., et al. (2013), New Data Systems and Products at the Permanent Service for Mean Sea Level. J. of Coastal Res., 29(3), 493 ? 504. doi:10.2112/JCOASTRES-D-12-00175.1

Hristova, G. H., and W. S. Kessler (2012), Surface Circulation in the Solomon Sea Derived from Lagrangian Drifter Observations. J. Phys. Oceanogr., 42, 448-458, doi:101175/JPO-D-11-099.1

Hristova, G. H., W. S. Kessler, J. C. McWilliams, and M. J. Molemaker (2014). Mesoscale variability and its seasonality in the Solomon and Coral Seas. J. Geophys. Res. Oceans, 119, 4669-4687, doi:10.1002/2013JC009741

Ishida, A., Y. Kashino, S. Hosoda, and K. Ando (2008). North-south asymmetry of warm water volume transport related with El Niño variability. Geophys. Res. Lett. 35, L18612, doi:10.1029/2008GL034858

Jacox, M. G., E. L. Hazen, K. D. Zaba, D. L. Rudnick, C. A. Edwards, A. M. Moore, and S. J. Bograd (2016), Impacts of the 2015-2016 El Niño on the California Current System: Early assessment and comparison to past events. Geophys. Res. Lett., 43, 7072-7080, doi:10.1002/2016GL069716

Jensen, T.G. (2001), Arabian Sea and Bay of Bengal exchange of salt and tracers in an ocean model. Geophys. Res. Lett., 28, 3967?3970.

Jensen, T. G. (2003), Cross-equatorial pathways of salt and tracers from the northern Indian Ocean: modelling results. Deep Sea Res., Part II, 50, 2111-2128.

Jensen, T. G., H. W. Wijesekera, E. S. Nyadjro, P. G. Thoppil, J. F. Shriver, K. K. Sandeep, and V. Pant (2016), Modeling salinity exchanges between the equatorial Indian Ocean and the Bay of Bengal. Oceanography, 29(2), 92-101, doi:10.5670/oceanog.2016.42

Johnson, G. C., and M. J. McPhaden (1999), Interior pycnocline flow from the subtropical to the equatorial Pacific Ocean. J. Phys. Oceanogr., 29, 2073-2089.

Kanzow, T., U. Send, W. Zenk, A. D. Chave, and M. Rhein (2006), Monitoring the integrated deep meridional flow in the tropical North Atlantic: Long-term performance of a geostrophic array. Deep-Sea Res. I, 53, 526-546, doi:10.1016/j.dsr.2005.12.007

Kennelly, M., K. Tracy, and D. R. Watts, (2007), Inverted Echo Sounder data processing manual. University of Rhode Island Graduate School of Oceanography Tech. Rep. 2007-02. [Available online at http://digitalcommons.uri.edu/physical_oceanography_techpts/2/.]

Kessler, W. S. (2001), EOF representations of the Madden-Julian Oscillation and its connection with ENSO. J. Clim., 14, 3055-3061.

Kessler, W. S., and L. Gourdeau (2007), The Annual Cycle of Circulation of the Southwest Subtropical Pacific, Analyzed in an Ocean GCM. J. Phys. Oceanogr., 37, 1610-1627, doi:10.1175/JPO3046.1

Kessler, W. S., and S. Cravatte (2012), ENSO and Short-Term Variability of the South Equatorial Current Entering the Coral Sea. J. Phys. Oceanogr., 43, 956-969, doi:10.1175/JPO-D-12-0113.1

Kessler, W. S., H. G. Hristova, and R. E. Davis (2019), Equatorward western boundary transport from the South Pacific: Glider observations, dynamics and consequences. Prog. Oceanogr., 175, 208-225, doi:10.1016/j.pocean.2019.04.005

Kuroda, Y. (2000), Variability of currents off the northern coast of New Guinea, J. Oceanogr., 56, 103-116.

Large, W.G., and S. G. Yeager (2009), The global climatology of an interannually varying air?sea flux data set. Clim. Dyn., 33, 341?364. doi:10.1007/s00382-008-0441-3

Lee, T., and I. Fukumori (2003), Interannual-to-decadal variations of tropical-subtropical exchange in the Pacific Ocean: Boundary versus interior pycnocline transports. J. Phys. Oceanogr., 16, 4022-2042.

Lee, C. M., S. U. P. Jinadasa, A. Anutaliya, L. R. Centurioni, H. J. S. Fernando, V. Hormann, M. Lankhorst, L. Rainville, U. Send, and H. W. Wijesekera (2016), Collaborative observations of boundary currents, water mass variability, and monsoon response in the southern Bay of Bengal. Oceanography, 29(2), 102?111, doi:10.5670/oceanog.2016.43

Levine, A. F. Z., and M. J. McPhaden (2016), How the July 2014 easterly wind burst gave the 2015-2016 El Niño a head start. Geophys. Res. Lett., 43, 6503-6510, doi:10.1002/2016GL069204

Luo, J-J., R. Zhang, S. Behera, Y. Masumoto, F-F. Jun, R. Lukas, T. Yamagata (2010), Interaction between El Niño and extreme Indian Ocean Dipole. J. Clim., 23, 726–742, doi: 10.1175/2009JCLI3104.1

McClean, J. L., D. C. Bader, M. E. Maltrud, K. J. Evans, M. A. Taylor, Q. Tang, et al. (2018), High-resolution fully-coupled ACME v0.1 approximate present day transient simulations. Abstract OM44C-2143, presented at the Ocean Sciences Meeting, Portland, OR, 12-16 Feb.

McCreary, J. P., P. K. Kundu, and R. L. Molinari (1993), A numerical investigation of dynamics, thermodynamics and mixed-layer processes in the Indian Ocean, Prog. Oceanogr., 31, 181-244.

McCreary, J. P., and P. Lu (1994), Interaction between the subtropical and equatorial ocean circulations: The subtropical cell. J. Phys. Oceanogr., 24(2), 466-497, doi:10.1175/1520-0485

McCreary, J. P., W. Han, D. Shankar, and S. R. Shetye (1996), Dynamics of the East India Coastal Current 2. Numerical solutions. J. Geophys. Res., 101, 13,993-14,010, doi:10.1029/96JC00560

McPhaden, M. J. (2015), Playing hide and seek with El Niño. Nat. Clim. Change, 5, 791-795.

McPhaden, M. J., and D. X. Zhang (2002), Slowdown of the meridional overturning circulation in the upper Pacific Ocean. Nature, 415, 603-608.

Meissner, T., F. J. Wentz, and A. Manaster (2018), Remote Sensing Systems SMAP Ocean Surface Salinities [Level 3 Running 8-day], Version 3.0 validated release. Remote Sensing Systems, Santa Rosa, CA, USA. Available online at www.remss.com/missions/smap. http://doi: 10.5067/SMP3A- 3SPCS

Melet, A., L. Gourdeau, W. Kessler, J. Verron, and J. Molines (2010a). Thermocline circulation in the Solomon Sea: a modeling study. J. Phys. Oceanogr., 31, 13324-1345.

Melet, A., L. Gourdeau, and J. Verron (2010b), Variability in Solomon Sea circulation derived from altimeter sea level data. Ocean Dynam., 60, 883-900.

Melet, A., J. Verron, L. Gourdeau, and A. Koch-Larrouy (2011), Equatorward pathways of the Solomon Sea water masses and their modifications, J. Phys. Oceanogr., 41(4), 810-826.

Melet, A., L. Gourdeau, J. Verron, and B. Djath (2013), Solomon sea circulation and water mass modifications: Response at ENSO timescales. Ocean Dyn., 63(1), 1-19, doi:10.1007/s10236-012-0582-0

Mooley, D. A., and B. Parthasarathy (1984), Indian summer monsoon and the east equatorial pacific sea surface temperature. Atmosphere-Ocean, 22(1), 23-35, doi.org/10.1080/07055900.1984.9649182

Permanent Service for Mean Sea Level (PSMSL) (2019), "Tide Gauge Data", Retrieved 20 May 2019 from http://www.psmsl.org/data/obtaining/.

Peterson, I., J. Hamilton, S. Prinsenberg, and R. Pettipas (2012), Wind-forcing of volume transport through Lancaster Sound. J. Geophys. Res. Oceans, 117, C11018, doi:10.1029/2012JC008140

Picaut, J., M. Ioualalen, C. Menkes, T. Delcroix, and M. J. McPhaden (1996), Mechanism of the zonal displacements of the Pacific Warm Pool: Implications for ENSO. Science, 274 (5292), 1486-1489.

Qiu, B., and S. Chen (2004), Seasonal Modulations in the Eddy Field of the South Pacific Ocean. J. Phys. Oceanogr., 34, 1515-1527.

Qiu, B., and S. Chen (2010), Interannual-to-decadal variability in the bifurcation of the North Equatorial Current off the Philippines. J. Phys. Oceanogr., 40, 2525-2538.

Ramage, C. S., and A. M. Hori (1981), Meteorological aspects of El Niño. Mon. Wea. Rev., 109, 1827-1835.

Rao, R. R., and R. Sivakumar (2003), Seasonal variability of sea surface salinity and salt budget of the mixed layer of the north Indian Ocean. J. Geophys. Res. Oceans, 108(C1), 9-1 ? 9-14, doi:10.1029/2001JC00907

Reppin, J., F. A. Schott, and J. Fischer (1999), Equatorial currents and transports in the upper central Indian Ocean: Annual cycle and interannual variability. J. Geophys. Res., 104(C7), 15495-15514.

Rio, M. H., and F. Hernandez (2004), A mean dynamic topography computed over the world ocean from altimetry, in situ measurements, and a geoid model. J. Geophys. Res., 109, C12032, doi:10.1029/2003JC002226

Rydbeck, A. V., T. G. Jensen, and M. Flatau (2019), Characterization of Intraseasonal Kelvin Waves in the Equatorial Pacific Ocean. J. Geophys. Res. Oceans., doi.org/10.1029/2018JC014838

Pant, V., M. S. Girishkumar, T. V. S. Udaya Bhaskar, M. Ravichandran, F. Papa, and V. P. Thangaprakash (2015), Observed interannual variability of near-surface salinity in the Bay of Bengal, J. Geophys. Res. Oceans, 120, 3315-3329, doi:10.1002/2014JC010340

Thomson, R. E., and W. J. Emery (2014), Data Analysis Methods in Physical Oceanography. Waltham, MA: Elsevier Science. Retrieved from http://roger.ucsd.edu/record=b8259868 S9

Tsuchiya, M., R. Lukas, R. A. Fine, E. Firing, and E. Lindstrom (1989), Source waters of the Pacific Equatorial Undercurrent. Progr. Oceanogr., 23, 101-147.

Saji, N. H., B. N. Goswami, P. N. Vinayachandran, and T. Yamagata (1999), A dipole in the tropical Indian Ocean, Nature, 401, 360-363.

Sanchez-Franks, A., B. G. M. Webber, B. A. King, P. N. Vinayachandran, A. J. Matthews, P. M. F. Sheehan, A. Behara, and C. P. Neema (2019), The Railroad Switch Effect of Seasonally Reversing Currents on the Bay of Bengal High-Salinity Core. Geophys. Res. Lett., 46, 6005-6014, doi:10.1029/2019GL082208

Santiago-Mandujano, F., and E. Firing (1990), Mixed-layer shear generated by wind stress in the central equatorial Pacific. J. Phys. Oceanogr., 20, 1576-1582.

Schott, F. A., J. Reppin, and J. Fischer (1994), Currents and transports of the Monsoon Current south of Sri Lanka. J. Geophys. Res., 99 (C12), 25127-25141.

Schott, F., and J. P. McCreary (2001), The monsoon circulation of the Indian Ocean, Prog. Oceanogr., 51, 1-123.

Schott, F. A., S. P. Xie, and J. P. McCreary (2009), Indian Ocean Circulation and Climate Variability. Rev. Geophys. 47, RG1002.

Sengupta, D., G. N. Bhsrath Raj, S. S. C. Shenoi (2006), Surface freshwater from Bay of Bengal runoff and Indonesian Throughflow in the tropical Indian Ocean. Geophys. Res. Lett., 33(22), L22609, doi:10.1029/2006GL027573

Shankar, D., J. P. McCreary, and W. Han (1996), Dynamics of the East India Coastal Current 1. Analytic solutions forced by interior Ekman pumping and local alongshore winds. J. Geophys. Res., 101(C6), 13975-13991.

Shankar, D., P. N. Vinayachandran, and A. S. Unnikrishnan (2002), The monsoon currents in the north Indian Ocean. Prog. Oceanogr., 52, 63-120, doi:10.1016/S0079-6611(02)00024-1

Shetye, S. R., A. D. Gouveia, S. S. C. Shenoi, D. Sundar, G. S. Michael, and G. Nampoothiri (1993), The western boundary current of the seasonal subtropical gyre in the Bay of Bengal. J. Geophys. Res., 98(C1), 945-954.

Shetye, S. R., A. D. Gouveia, D. Shankar, S. S. C. Shenoi, P. N. Vinayachandran, D. Sundar, G. S. Michael, and G. Nampoothiri (1996), Hydrography and circulation in the western Bay of Bengal during the northeast monsoon. J. Geophys. Res., 101, 14,011-14,025.

Smith, W. H. F., and D. T. Sandwell (1997), Global seafloor topography from satellite altimetry and ship depth soundings, Science, 277, 1957-1962.

Sreenivas, P., C. Gnanaseelan, and K. V. S. R. Prasad (2012), Influence of El Niño and Indian Ocean Dipole on sea level variability in the Bay of Bengal. Global Planet Change, 80-81, 215-225, doi:10.1016/j.gloplacha.2011.11.001

Thompson, B., C. Gnanaseelan, P. S. Salvekar (2006), Variability in the Indian Ocean circulation and salinity and its impact on SST anomalies during dipole events. J. Mar. Sci Technol., 64, 853-880.

Vinayachandran, P. N., and T. Yamagata (1997), Monsoon response of the sea around Sri Lanka: generation of thermal domes and anticyclonic vortices. J. Phys. Oceanogr., 28, 1946-1960.

Vinayachandran, P. N., Y. Masumoto, T. Mikawa, and T. Yamagata (1999), Intrusion of the southwest monsoon current into the Bay of Bengal. J. Geophys. Res., 104(C5), 11077-11085.

Vinayachandran, P. N., T. Kagimoto, Y. Masumoto, P. Chauhan, S. R. Nayak, and T. Yamagata, (2005a), Bifurcation of the East India Coastal Current east of Sri Lanka. Geophys. Res. Lett., 32, L15606, doi:10.1029/2005GL022864

Vinayachandran, P. N., J. P. McCreary, R. R. Hood, and K. E. Kohler (2005b), A numerical investigation of the phytoplankton bloom in the Bay of Bengal during northeast monsoon. J. Geophys. Res., 110, C12001, doi:10.1029/2005JC002966

Vinayachandran, P. N., D. Shankar, S. Vernekar, K. K. Sandeep, P. Amol, C. P. Neema, and A. Chatterjee (2013), A summer monsoon pump to keep the Bay of Bengal salty. Geophys. Res. Lett., 40, 1777-1782, doi:10.1002/grl.50274

Wang, B., R. Wu, and R. Lukas (2000), Annual adjustment of the thermocline in the tropical Pacific Ocean. J. Clim., 13, 596-1942.

Waworuntu, J. M., R. A. Fine, D. B. Olson, and A. L. Gordon (2000), Recipe for Banda Sea water. J. Mar. Res., 58, 547-569.

Webster, P. J., V. O. Magana, T. N. Palmer, J. Shukla, R. A. Tomas, M. Yanai, and T. Yasunari (1998). Monsoons: Processes, predictability, and the prospects for prediction. J. Geophys. Res., 103, 14451-14510.

Wentz, F. J., J. Scott, R. Hoffman, M. Leidner, R. Atlas, and J. Ardizzone (2015). Remote Sensing Systems Cross-Calibrated Multi-Platform (CCMP) 6-hourly ocean vector wind analysis product on 0.25 deg grid, Version 2.0, 2012-2017. Remote Sensing Systems, Santa Rosa, CA. Available online at www.remss.com/measurements/ccmp. Accessed 23 Mar 2018.

Wijesekera, H. W., T. G. Jensen, E. Jarosz, W. J. Teague, E. J. Metzger, D. W. Wang, S. U. P. Jinadasa, K. Arulananthan, L.R. Centurioni, and H. J. S. Fernando (2015), Southern Bay of Bengal currents and salinity intrusions during the northeast monsoon. J. Geophys. Res. Oceans, 120, 6897-6913, doi:10.1002/2015JC010744

Wijesekera, H. W., W. J. Teague, D. W. Wang, E. Jarosz, and T. G. Jensen (2016), Low-Frequency Currents from Deep Moorings in the Southern Bay of Bengal. J. Phys. Oceanogr., 46, 3209-3238, doi: 10.1175/JPO-D-16-0113.1

Wilson, E. A., S. C. Riser (2016), An Assessment of the Seasonal Salinity Budget for the Upper Bay of Bengal. J. Phys. Oceanogr., 46, 1,361-1,376.

Wyrtki, K. (1985), Water displacements in the Pacific and the genesis of El Niño cycles, J. Geophys. Res., 90, 475-486.

Yasunari, T. (1990), Impact of Indian monsoon on the coupled atmosphere/ocean system in the tropical pacific. Meteorl. Atmos. Phys., 44, 29-41, doi:10.1007/BF01026809

Zilberman, N. V., D. H. Roemmich, and S. T. Gille (2012), The Mean and the Time Variability of the Shallow Meridional Overturning Circulation in the Tropical South Pacific Ocean. J. Clim., 26, 4069-4087, doi:10.1175/JCLI-D-12-00120.1